POLITECNICO DI MILANO
Dipartimento di Elettronica e Informazione
DOCTORAL PROGRAM IN INFORMATION TECHNOLOGY

Human-centric behaviour of redundant manipulators under kinematic control

Doctoral Dissertation of:
Andrea Maria Zanchettin

Advisor:
Prof. Paolo Rocco

Tutor:
Prof. Carlo Piccardi

Chair of the Doctoral Program:
Prof. Carlo Fiorini

2012 - XXIV edition

To my parents

Vorrei essere libero, libero come un uomo.
Come l'uomo più evoluto che si innalza con la propria intelligenza
e che sfida la natura con la forza incontrastata della scienza,
con addosso l'entusiasmo di spaziare senza limiti nel cosmo,
è convinto che la forza del pensiero sia la sola libertà.

I'd like to be free, free like a man.
Like the most evolved man, rising up with his own intelligence
and challenging the nature with the unopposed strength of science,
wearing the enthusiasm to move freely in the cosmos,
he is convinced that the power of thought is the only freedom.

GIORGIO GABER

Acknowledgements

This research has been carried out under the supervision of Prof. Paolo Rocco. I wish to thank him for all the fruitful discussions, and for his kind and precious support and guidance during all the PhD program.

I am especially indebted with Dr. Luca Bascetta for his kind availability and help. I would like also to thank all the people at my Department who work in the ROSETTA (RObot control for Skilled ExecuTion of Tasks in natural interaction with humans; based on Autonomy, cumulative knowledge and learning) project[1]: Professors Gianni Ferretti, Arturo Locatelli, Gianantonio Magnani, Nicola Schiavoni and Dr. Bakir Lacevic.

I wish to thank Prof. Giuseppe Oriolo from Università di Roma "La Sapienza", who served as a reviewer of this work, for his overall appreciation and valuable suggestions on how to strengthen the thoroughness of the results.

[1]The research leading to these results has been partly supported by the European Community's Seventh Framework Programme FP7/2007-2013 - Challenge 2 - Cognitive Systems, Interaction, Robotics - under grant agreement No 230902 - ROSETTA. This support is gratefully acknowledged. For further information see http://www.fp7rosetta.org/.

Last but not least, a grateful acknowledgement to Professors Rolf Johansson and Anders Robertsson at Lund University for hosting me at their Department in Spring 2010, and for their cooperation and hospitality.
I would like to thank also all the colleagues in the ROSETTA project and in particular Ioannis Symeonidis from Ludwig-Maximilians University of Munich and Mikael Hedelind from ABB Research Corporate in Västerås for their cooperation and fruitful exchange of ideas.

Milano, 13.01.2012

Abstract

Although robustness and safety of industrial robots have considerably increased in the last decades, common industrial manipulators are still largely unable to cooperate with human beings in a natural way.
A novel fact in recent years which may contribute to alleviate this situation is the commercial availability of redundant manipulators (i.e. robotic arms having more degrees of freedom than those strictly necessary to perform a certain task). It is well known that such robotic arms allow to achieve high levels of dexterity: since the same task can be performed in several ways, redundant manipulators offer a wide range of flexibility in motion planning. Moreover, thanks to the extra Degree(s) of Freedom (DOF), it is possible to modify in real-time the behavior of the robot, in order improve safety in the cooperation with human co-workers, without modifying the end-effector motion.

The aim of this research is to study strategies to exploit the kinematic redundancy of robot manipulators in order to make their motion as natural as possible. Since the robot is supposed to cooperate with humans, its motion should be predictable, safe, and intuitive. This work is then focused on the development of criteria to design, and enforce on an industrial robot control architecture, a human-like kinematic control for redundant manipulators. In this way, a human-friendly behavior of the robot will ensure a natural cooperation between robotic manipulators and humans, which is not obtained with today commercial industrial manipulators.

Riassunto

Nonostante la robustezza e l'affidabilità dei robot industriali sia considerevolmente cresciuta negli ultimi decenni, i comuni manipolatori industriali non sono tuttora idonei per una cooperazione naturale con gli esseri umani.
Una novità degli ultimi anni che potrebbe mitigare questa situazione è la disponibilità commerciale di manipolatori ridondanti (bracci robotici con più gradi di libertà rispetto a quelli strettamente necessari per eseguire un certo compito). È noto che questi bracci robotici consentono di ottenere elevati gradi di destrezza: il medesimo compito può essere infatti eseguito in diversi modi e per questo motivo i manipolatori ridondanti offrono una maggiore flessibilità nella pianificazione del movimento. Inoltre, grazie ai gradi di libertà aggiuntivi, è sempre possibile modificare il tempo reale il comportamento del robot in modo da incrementare la sicurezza nella cooperazione con gli operatori umani, senza alterare il moto dell'organo terminale.

Questa ricerca si pone l'obiettivo di studiare metodologie di utilizzo della ridondanza cinematica dei manipolatori robotici in modo da rendere il loro moto il più naturale possibile.
Per una migliore cooperazione uomo-macchina, il moto del braccio robotico dovrebbe risultare predicibile, sicuro ed intuitivo. Questo lavoro è mirato allo sviluppo di criteri per il progetto di algoritmi "umano-centrici" di inversione cinematica e alla loro implementazione all'interno di un controllore industriale. In questo modo, un moto più naturale del robot assicurerà una cooperazione più spontanea tra persone e manipolatori robotici che al momento non è ottenibile con i più moderni robot commerciali.

Outline

ROBOTIC aided manufacturing is nowadays a technology with a high level of maturity. Thanks to their flexibility, industrial robots are adopted in several transformation processes such as welding, painting, deburring, assembly, etc.
Despite the benefits of articulated manipulators to industrial production, there are today several obstacles to obtain a more widespread use of robots. They still need a lot of skilled engineering effort for installation, setup and programming. They also require closed-ended environments, with physical protection devices to separate them from human workers, and this limits their flexible usage. For this reason, some of the most attractive studies in this field focus on the development of strategies to enforce safety in human robot interaction. In fact, common industrial manipulators are still not able to cooperate with human beings in a natural way.

Using redundant manipulators, namely robotic arms having more DOF than those strictly necessary to perform a certain task, it is possible to achieve high levels of dexterity, which can be exploited to make the robot able to cooperate with humans in the same way that humans would cooperate with other humans. Since the same task can be performed in infinite ways, redundant manipulators offer a wide range of flexibility in motion planning. Thanks to the extra DOF, it is always possible to modify in real-time the behavior of the robot, in order to ensure additional criteria (such as singularity or obstacle avoidance, or torque minimization) or to achieve a safe cooperation with human co-workers, without suspending the main task.
Since the early 80's, a considerable amount of literature on redundant manipu-

lators is available, a part of which is reviewed in Chapter 1. Further research in this field is strongly motivated by the renewed interest of industry in redundant manipulators, due to their increased dexterity with respect to their non-redundant counterparts. Robot manufactures are in fact putting on the market kinematically redundant robots, see Fig. 1, which naturally fosters research in the area.

(a) KUKA LWR

(b) BARRETT WAM

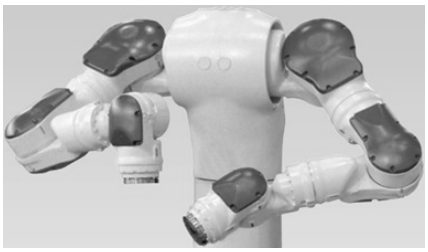

(c) YASKAWA SDA-10

Figure 1: *Examples of commercial redundant robots*

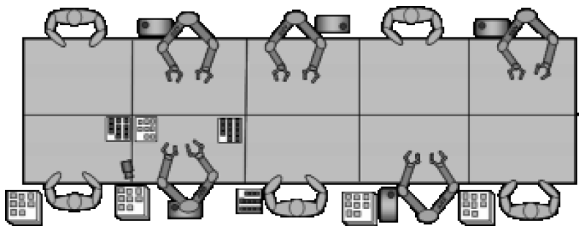

Figure 2: *An example of a shared workspace between humans and robots (source:* ROSETTA *project)*

Future robotic controllers will exploit new functionalities that are "human-centered": the controller has knowledge about how the robot could inflict injuries on humans and how to avoid them, and it is equipped with sensors, sensor processing and reasoning capabilities to find the optimal trade-off between effective progress in its task and safe physical cooperation and interaction with the human co-worker(s) as sketched in Fig. 2.

A human-centered technology is thus the way to make a physical cooperation no longer a futuristic vision but a concrete opportunity just around the corner. This cooperation should not only be physically safe, but also psychologically comfortable to the humans: they have, at all times, to feel assured that they understand the intentions of the robot, and that the robot executes its tasks with motion profiles that humans perceive as natural. For this, next generation manipulators are expected to resemble a human-like behavior at kinematic level, in order to avoid any unease or discomfort to the nearby humans.
In this work we conjecture that making robots able to move and act similar to humans might facilitate their social acceptance.

Thesis structure and main contributions

The original contribution of this thesis to the field of human-robot interaction concerns the exploitation of the kinematic redundancy of next generation industrial manipulators to achieve a natural-looking motion and facilitate a psychologically safe interaction between humans and robots.

This work is organized in three Parts:

1. in the first Part, a general user-oriented framework for redundancy resolution in industrial robotic manipulators is proposed and applied to several simulation and experimental cases;

2. in Part II, a detailed kinematic study on the human arm motion and the identification of a redundancy resolution criterion to explain human-like motion patterns are presented;

3. Part III describes the implementation, based on the framework discussed in Part I, of the identified human-like redundancy resolution on a 14-DOF dual-arm anthropomorphic industrial manipulator and discusses the evidence of an increased social acceptability.

Part I - A framework for redundancy resolution

In Chapter 2, the first original contribution of this thesis is presented: a general framework for redundancy resolution in industrial manipulators. The flexibility of the proposed approach is discussed. In particular, it is shown that the selection of the redundancy resolution criterion is totally decoupled from the implementation of the algorithm adopted to generate joint angle references. Any user-defined redundancy resolution criterion can thus be enforced. Potentialities of this new

methodology are experimentally verified on an industrial robot in a case study where functional redundancy occurs.
In Chapter 3, the proposed redundancy resolution technique is experimentally applied to different industrial applications. In particular the possibility to handle the case of multiple degrees of redundancy as well as the capability to cope with sensor driven task modifications are discussed.

Part II - Analysis and synthesis of the human arm motion

Chapter 4 presents the experimental campaign carried out to study the natural motion of the human arm and in particular to address the identification of a suitable way to describe how humans resolve the kinematic redundancy of their arm. The protocol of the experiments as well as the procedure to extract joint variables is discussed.
Based on these experiments, Chapter 5 describes the nonlinear correlation analysis performed using the acquired data. A clear correlation has been found between the hand pose and the elbow swivel angle which was used to characterize the redundant DOF of the human arm.

Part III - Application to a dual-arm robot prototype

In Chapter 6, the identified correlation has been exploited in the robotic controller to achieve a natural-looking motion for a 14-DOF prototype robot. Physiological experiments on volunteers to discuss the acceptability of robot trajectories are discussed in order to give a validation to the work contained in this dissertation.

Publications

This thesis is based on the following publications:

1. A.M. Zanchettin, P. Rocco - *A general user-oriented framework for holonomic redundancy resolution in robotic manipulators using task augmentation*, IEEE Transactions on Robotics (published online, DOI 10.1109 / TRO.2011.2173852).

2. A.M. Zanchettin, P. Rocco - *Dual-arm redundancy resolution based on null-space dynamically-scaled posture optimization*, IEEE International Conference on Robotics and Automation, ICRA 2012, Saint Paul (Minnesota, USA), May 14th-18th, 2012 (accepted).

3. A.M. Zanchettin, P. Rocco - *On the use of functional redundancy in industrial robotic manipulators for optimal spray painting*, 18th IFAC World

Congress, Milano (Italy), August 28th - September 2nd, 2011 - pp. 11495-11500.

4. I. Symeonidis, S. Peldschus, A.M. Zanchettin, P. Rocco, D. Bortot, K. Bengler - *Database of human reach motions in work environment*, First International Symposium on Digital Human Modeling, DHM 2011, Lyon (France), June 14th-16th, 2011 - pp. 1-6.

5. A.M. Zanchettin, P. Rocco, A. Robertsson, R. Johansson - *Exploiting task redundancy in industrial manipulators during drilling operations*, IEEE International Conference on Robotics and Automation, ICRA 2011, Shanghai (China), May 9th-13th, 2011 - pp 128-133.

6. A.M. Zanchettin, P. Rocco, L. Bascetta, I. Symeonidis, S. Peldschus - *Kinematic analysis and synthesis of the human arm motion during a manipulation task*, IEEE International Conference on Robotics and Automation, ICRA 2011, Shanghai (China), May 9th-13th, 2011 - pp. 2692-2697.

7. A.M. Zanchettin, P. Rocco, L. Bascetta, I. Symeonidis, S. Peldschus - *Kinematic motion analysis of the human arm during a manipulation task*, International Symposium on Robotics and German Conference on Robotics, ISR/Robotik 2010, Munich (Germany), June 7th-9th, 2010 - pp. 1252-1257.

8. L. Bascetta, P. Bolzern, G. Ferretti, B. Lacevic, A. Locatelli, G. Magnani, P. Rocco, N. Schiavoni, A.M. Zanchettin - *Robotica industriale umano-centrica: il progetto ROSETTA*, Automazione e Strumentazione, June 2011 - pp. 75-79.

9. L. Bascetta, G. Ferretti, B. Lacevic, G. Magnani, P. Rocco, A.M. Zanchettin - *Robotica industriale umano-centrica: il progetto ROSETTA*, Motion Control 2010, Cinisello Balsamo (Italy), November 10th-11th, 2010 - pp. 1-10.

10. A. Locatelli, P. Rocco, N. Schiavoni, A.M. Zanchettin - *Ripetibilità dei movimenti nei manipolatori robotici a ridondanza cinematica*, Motion Control 2010, Cinisello Balsamo (Italy), November 10th-11th 2010, pp. 1-11.

and on this submitted material:

1. A.M. Zanchettin, L. Bascetta, P. Rocco - *Human-like redundancy resolution for anthropomorphic industrial manipulators*, IEEE Robotics and Automation Magazine (under review).

The following publications contain relevant results, but not covered in the doctoral dissertation:

1. A.M. Zanchettin, P. Rocco, G. Ferretti - *Numerical issues in integrating holonomic kinematic inversion algorithms for redundant manipulators*, 8th IFAC Symposium on Nonlinear Control Systems, NOLCOS 2010, Bologna (Italy), September 1st-3rd, 2010 - pp. 999-1004.

2. P. Rocco, A.M. Zanchettin - *General parameterization of holonomic kinematic inversion algorithms for redundant manipulators*, IEEE International Conference on Robotics and Automation, ICRA 2010, Anchorage (Alaska, USA), May 3rd-8th, 2010 - pp. 3721-3726.

Cooperations with other Institutions

The research leading to the results presented in this thesis has been carried out at the Dipartimento di Elettronica e Informazione (DEI) of Politecnico di Milano, Italy. The experiments described in Chapter 3 have been performed in the Laboratory of Automatic Control at DEI.
The force control experiments discussed at the end of Chapter 3 have been carried out in the Laboratory of Robotics at the Department of Automatic Control of Lund University, LTH, Sweden, during my research stay in Lund in Spring 2010.
The motion capture experiments presented in Chapter 4 have been carried out at the Institute of Ergonomics of the Technische Universität München, Germany in cooperation with the Institute for Legal Medicine of the Ludwig-Maximilians University of Munich, Germany.
The physiological experiments described in Chapter 6 have been performed in the Laboratory of Automatic Control at DEI, in cooperation with the Institute for Legal Medicine of the Ludwig-Maximilians University of Munich, Germany.

Contents

List of Figures

List of Figures

List of Tables

CHAPTER 1

Introduction and background

1.1 Kinematically redundant manipulators

A manipulator consists of a series of rigid bodies connected by joints. If q_i ($i = 1, \ldots, n$) denotes the variable characterizing the position of the i-th joint, the posture of the entire chain is uniquely defined once the vector $\boldsymbol{q} = \begin{bmatrix} q_1 & q_2 & \ldots & q_n \end{bmatrix}^T$ is given.
The task, e.g. the position and orientation of the end-effector, is usually assigned with the vector $\boldsymbol{\mu} = \begin{bmatrix} \mu_1 & \mu_2 & \ldots & \mu_m \end{bmatrix}^T$ comprising Cartesian position coordinates and a minimal representation of the orientation. A manipulator is redundant if $n > m$.
For a given task, the direct kinematic mapping associated to a manipulator is thus a function $\boldsymbol{f} : \mathbb{R}^n \to \mathbb{R}^m$:

$$\boldsymbol{\mu} = \boldsymbol{f}(\boldsymbol{q}) \tag{1.1}$$

The kinematic inversion problem is to find $\boldsymbol{q}$ for a given $\boldsymbol{\mu}$ such that the previous equation holds. Usually, this problem is addressed at velocity level. In other words, the first time derivative of (1.1) is taken into account:

$$\dot{\boldsymbol{\mu}} = \frac{\partial \boldsymbol{f}}{\partial \boldsymbol{q}} \dot{\boldsymbol{q}} = \boldsymbol{J}(\boldsymbol{q})\, \dot{\boldsymbol{q}} \tag{1.2}$$

where $\boldsymbol{J}$ is a $m \times n$ matrix called task-Jacobian, or simply Jacobian[1].

1.1.1 Null-space velocities and self-motion

In case of redundancy, the task Jacobian introduced so far is a $m \times n$ matrix where $m < n$. Since the problem of the kinematic inversion is to compute $\dot{\boldsymbol{q}}$ for a given $\dot{\boldsymbol{\mu}}$ such that (1.2) holds, it follows that, even when the Jacobian is full rank, the solution of such a problem is no longer unique, making the redundancy resolution a non-trivial task. In other words, considering $\boldsymbol{J}$ as a linear transformation from $\mathbb{R}^n$ to $\mathbb{R}^m$, (1.2) represents an under-determined system of equations in the unknown $\dot{\boldsymbol{q}}$.
For a given configuration $\boldsymbol{q}$, there exists also a set of joint velocities which do not affect the task velocity. In fact, consider two different solutions $\dot{\boldsymbol{q}}^\star$ and $\dot{\boldsymbol{q}}^\sharp$ of (1.2), then their difference yields a zero task velocity, as it can be simply verified:

$$\boldsymbol{J}\left(\dot{\boldsymbol{q}}^\star - \dot{\boldsymbol{q}}^\sharp\right) = \boldsymbol{J}\dot{\boldsymbol{q}}^\star - \boldsymbol{J}\dot{\boldsymbol{q}}^\sharp = \dot{\boldsymbol{\mu}} - \dot{\boldsymbol{\mu}} = \boldsymbol{0} \tag{1.3}$$

Actually, the set of joint velocities producing a zero task velocity forms a vector space which is called *null-space*:

$$\mathcal{N}(\boldsymbol{J}) = \{\dot{\boldsymbol{q}} : \boldsymbol{J}\dot{\boldsymbol{q}} = \boldsymbol{0}\} \tag{1.4}$$

Letting $\mathcal{R}(\boldsymbol{J})$ be the space of all admissible task velocities in a given configuration, then the rank-nullity theorem states that

$$dim\{\mathcal{R}(\boldsymbol{J})\} + dim\{\mathcal{N}(\boldsymbol{J})\} = n \tag{1.5}$$

Therefore, when the task Jacobian is full-rank, i.e. $rank(\boldsymbol{J}) = m$, and thus $dim\{\mathcal{R}(\boldsymbol{J})\} = m$, the null-space is a vector space of dimension $n - m$, as the number of degrees of redundancy.
A more rigorous geometrical analysis to address these concepts can be performed using the Singular Value Decomposition (SVD) of the Jacobian matrix $\boldsymbol{J}$. Consider

$$\boldsymbol{J} = \boldsymbol{U}\boldsymbol{\Sigma}\boldsymbol{V}^T \tag{1.6}$$

the SVD of $\boldsymbol{J}$, where $\boldsymbol{U}$ and $\boldsymbol{V}$ are orthonormal matrices and $\boldsymbol{\Sigma}$ is a $m \times n$ matrix which can be further decomposed as follows:

$$\boldsymbol{\Sigma} = \begin{bmatrix}\boldsymbol{S} & \boldsymbol{0}\end{bmatrix} \tag{1.7}$$

where[2] $\boldsymbol{S} = diag(\sigma_1, \sigma_2, \ldots, \sigma_m)$ is a diagonal matrix which contains the so-called *singular values* $\sigma_i > 0$.

[1] Capital letters are going to be used to denote matrices. Their dependence on $\boldsymbol{q}$, if any, will be omitted.
[2] The Jacobian matrix is assumed to be full-rank.

The columns of matrix $\boldsymbol{U}$ represent a basis of all feasible task velocities and therefore form a basis of $\mathcal{R}(\boldsymbol{J})$. On the other hand, letting

$$\boldsymbol{V} = \begin{bmatrix} \boldsymbol{v_1} & \dots & \boldsymbol{v_m} & \boldsymbol{v_{m+1}} & \dots & \boldsymbol{v_n} \end{bmatrix} \tag{1.8}$$

then the last $n - m$ columns of $\boldsymbol{V}$, namely from $\boldsymbol{v_{m+1}}$ to $\boldsymbol{v_n}$, form an orthonormal basis of the null-space of the task Jacobian $\boldsymbol{J}$. In other words, any linear combination of them is a null-space velocity.
Finally, the set of all robot postures $\boldsymbol{q}$ satisfying equation (1.1) is called the *self-motion manifold* for the task constraint $\boldsymbol{\mu} = \boldsymbol{f}(\boldsymbol{q})$. A motion along the self-motion manifold is therefore called self-motion, [85]. The effect of the self-motion can be easily visualized in Fig. 1.1 where a 7-DOF robot is spanning the self-motion manifold while maintaining the same position/orientation of the end-effector.

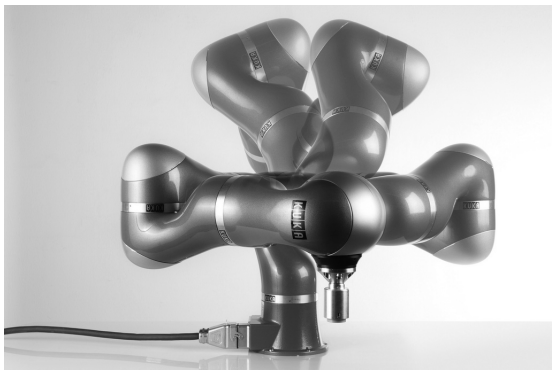

Figure 1.1: KUKA LWR *performing a self-motion*

1.1.2 Resolution of kinematic redundancy

The solutions of the inverse kinematic problem can be parameterized by superimposition of two terms: a particular solution and an arbitrary null-space velocity. The former can be computed as follows:

$$\dot{\boldsymbol{q}}^{\boldsymbol{0}} = \boldsymbol{J}^{\dagger}\dot{\boldsymbol{\mu}} \quad \boldsymbol{J}^{\dagger} = \boldsymbol{V}\begin{bmatrix} \boldsymbol{S}^{-1} \\ \boldsymbol{0} \end{bmatrix}\boldsymbol{U}^{T} = \boldsymbol{J}^{T}\left(\boldsymbol{J}\boldsymbol{J}^{T}\right)^{-1} \tag{1.9}$$

where $\boldsymbol{J}^{\dagger}$ is the so-called Moore-Penrose pseudo-inverse of $\boldsymbol{J}$. Equation (1.9) represents the unique solution of (1.2) without any null-space component. For linearity, one can always modify the computed solution $\dot{\boldsymbol{q}}^{\boldsymbol{0}}$ without affecting the desired task velocity by adding an arbitrary null-space velocity.
As reported in [11], a general solution of (1.2) can be written as follows:

$$\dot{\boldsymbol{q}} = \boldsymbol{J}^{\dagger}\dot{\boldsymbol{\mu}} + \left(\boldsymbol{I} - \boldsymbol{J}^{\dagger}\boldsymbol{J}\right)\boldsymbol{v} \tag{1.10}$$

where $\left(\boldsymbol{I} - \boldsymbol{J}^{\dagger}\boldsymbol{J}\right)$ projects an arbitrary vector $\boldsymbol{v}$ in the null-space of $\boldsymbol{J}$.
The availability of additional DOF suggests to design performance criteria based on which one particular solution among the others can be selected.

In particular, let $u\left(\boldsymbol{q}\right)$ be a convex cost function defined over the robot configuration space, then $-\boldsymbol{\nabla} u = -\partial u/\partial \boldsymbol{q}$ is a direction in the configuration space towards the minimum of u. Therefore, one might select $\boldsymbol{v}$ in (1.10) as follows

$$\boldsymbol{v} = -k\boldsymbol{\nabla} u, \quad k > 0 \tag{1.11}$$

in order to converge to a local minimum of the cost function, as in the gradient optimization method, see e.g. [50]. The cost function can be thus selected in order to meet additional criteria, such as for instance singularity avoidance, see e.g. [88], or joint limits avoidance [75], defining

$$u = \frac{1}{2}\sum_{i=1}^{n}\left(\frac{q_i - q_i^{mid}}{q_i^{max} - q_i^{min}}\right)^2 \tag{1.12}$$

where $q_i^{mid} = \left(q_i^{max} + q_i^{min}\right)/2, i = 1, \ldots, n$ and q_i^{min} and q_i^{max} are the lower and upper limits for joint i, respectively.

The general solution in (1.10) can be interpreted as a solution of a certain quadratic optimization problem. It is easy to verify, using the theory of Lagrange multipliers, that (1.10) is the unique optimal solution of the following quadratic problem

$$\min_{\dot{\boldsymbol{q}}}\left[\frac{1}{2}\dot{\boldsymbol{q}}^T\dot{\boldsymbol{q}} - \dot{\boldsymbol{q}}^T\boldsymbol{v}\right] \text{ subject to } \boldsymbol{J}\dot{\boldsymbol{q}} - \dot{\boldsymbol{\mu}} = \boldsymbol{0} \tag{1.13}$$

In many situations, it might be convenient to emphasize certain directions in the joint space with respect to others. For this reason, the following quadratic optimization problem can be introduced:

$$\min_{\dot{\boldsymbol{q}}}\frac{1}{2}\dot{\boldsymbol{q}}^T\boldsymbol{W}\dot{\boldsymbol{q}} \text{ subject to } \boldsymbol{J}\dot{\boldsymbol{q}} - \dot{\boldsymbol{\mu}} = \boldsymbol{0} \tag{1.14}$$

where $\boldsymbol{W} = \boldsymbol{W}^T > 0$ represents a weight matrix. The solution of the weighted problem is thus the following one

$$\dot{\boldsymbol{q}} = \boldsymbol{J}_{\boldsymbol{W}}{}^{\dagger}\dot{\boldsymbol{\mu}} \quad \boldsymbol{J}_{\boldsymbol{W}}{}^{\dagger} = \boldsymbol{W}^{-1}\boldsymbol{J}^T\left(\boldsymbol{J}\boldsymbol{W}^{-1}\boldsymbol{J}^T\right)^{-1} \tag{1.15}$$

The weight matrix can be either constant or configuration-dependent. For example, in [60] the manipulator inertia matrix $\boldsymbol{B}\left(\boldsymbol{q}\right)$ is selected as a weight matrix in (1.14) to minimize the manipulator kinetic energy and achieve additional

dynamics-related properties.

A different approach in solving the under-determined system in (1.2) consists in adding new constraints. The so called *extended Jacobian* method, proposed in [10], is aimed at designing a kinematic control strategy of the kind

$$\dot{\boldsymbol{q}} = \boldsymbol{G}\dot{\boldsymbol{\mu}} \tag{1.16}$$

able to enforce the minimality of a certain configuration dependent cost-function. Since the case studies reported next Chapters are somehow related to this method, the extended Jacobian is briefly reviewed in the following.
Consider a differentiable cost function to be optimized, say $u(\boldsymbol{q})$, and let $\boldsymbol{N}$ be a null-space basis of the Jacobian matrix $\boldsymbol{J}$. Assume that the initial configuration of the robot extremizes the cost function. Then, the following optimization problem can be formalized:

$$\min_{\boldsymbol{q}} u(\boldsymbol{q}) \text{ subject to } \boldsymbol{\mu} - \boldsymbol{f}(\boldsymbol{q}) = \boldsymbol{0} \tag{1.17}$$

It can be easily proven that the solutions of (1.17) are such that

$$\boldsymbol{N}^T \left(\frac{\partial u}{\partial \boldsymbol{q}} \right)^T = \boldsymbol{0} \tag{1.18}$$

Therefore, in order to enforce the constraint (1.18), the following kinematic control strategy can be adopted:

$$\dot{\boldsymbol{q}} = \begin{bmatrix} \boldsymbol{J} \\ \dfrac{\partial}{\partial \boldsymbol{q}} \left(\boldsymbol{N}^T \left(\dfrac{\partial u}{\partial \boldsymbol{q}} \right)^T \right) \end{bmatrix}^{-1} \begin{bmatrix} \dot{\boldsymbol{\mu}} \\ \boldsymbol{0} \end{bmatrix} \tag{1.19}$$

The extended Jacobian method can be seen as a special case of the *configuration control*, later developed in [104], which uses task augmentation, [39], [102]:

$$\dot{\boldsymbol{q}} = \begin{bmatrix} \boldsymbol{J} \\ \dfrac{\partial \boldsymbol{h}}{\partial \boldsymbol{q}} \end{bmatrix}^{-1} \begin{bmatrix} \dot{\boldsymbol{\mu}} \\ \boldsymbol{0} \end{bmatrix} \tag{1.20}$$

where $\boldsymbol{h}(\cdot) : \mathbb{R}^n \to \mathbb{R}^{n-m}$ is a generic differentiable function designed to enforce the constraint $\boldsymbol{h}(\boldsymbol{q}) = \boldsymbol{const}$.

1.1.3 Cyclicity

A side effect of the use of kinematically redundant manipulators under a kinematic control strategy is that the motion of the robot can be to some extent unpredictable. As first noticed in [66], under a kinematic control strategy, a closed

trajectory in the task space can be mapped into an open trajectory in the configuration space. A dual aspect of the same property is that any trajectory between the same start and goal task positions, even when the motion of the robot starts from the same joint configuration, might end with different joint configurations. These circumstances (sketched in Fig. 1.2), usually referred to as the non-cyclicity property, are highly undesirable and may represent a limitation in using redundant manipulators.

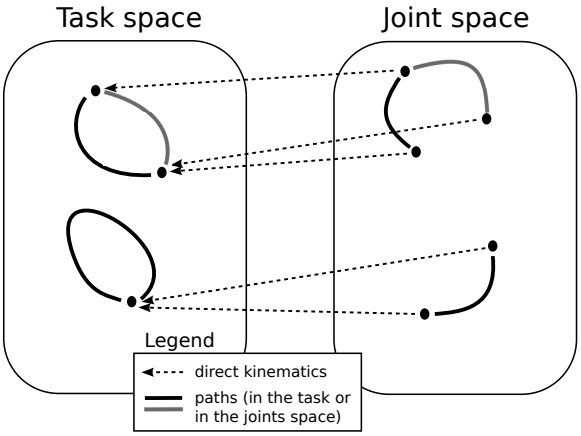

Figure 1.2: *Possible unpredictable behaviors of redundant manipulators*

Kinematic control strategies that avoid these problems exist and are called cyclic (or repeatable). A mathematical condition for an inversion technique to be cyclic has been developed in [105] and further refined in [98]. In differential geometry the property underlying these problems is called non-holonomy, see e.g. [85] and [35].
In the following, a brief review of the existing results on cyclic kinematic control strategies is given. For this, the definitions of *distribution* and *involutivity* are needed.

Definition 1.1 (Distribution)**.** *The distribution associated to the kinematic control strategy* $\dot{\boldsymbol{q}} = \boldsymbol{G}\dot{\boldsymbol{\mu}}$ *where* $\boldsymbol{G} = \begin{bmatrix} \boldsymbol{G_1} & \dots & \boldsymbol{G_m} \end{bmatrix}$ *is* $span\left(\boldsymbol{G_1}, \dots, \boldsymbol{G_m}\right) = \mathcal{R}\left(\boldsymbol{G}\right)$.

Definition 1.2 (Involutivity)**.** *The distribution associated to the kinematic control strategy* $\boldsymbol{G}$ *is said to be involutive if and only if*

$$\forall\left(i,j\right) : \left[\boldsymbol{G_i}, \boldsymbol{G_j}\right] \in \mathcal{R}\left(\boldsymbol{G}\right) \tag{1.21}$$

where

$$\left[\boldsymbol{A}, \boldsymbol{B}\right] = \frac{\partial \boldsymbol{B}}{\partial \boldsymbol{q}}\boldsymbol{A} - \frac{\partial \boldsymbol{A}}{\partial \boldsymbol{q}}\boldsymbol{B} \tag{1.22}$$

denotes the Lie bracket operation, [52].

As reported in [105] a necessary and sufficient condition to check whether a kinematic control strategy is cyclic can be stated as follows:

Theorem 1.1. *A kinematic control strategy $\dot{\boldsymbol{q}} = \boldsymbol{G}\dot{\boldsymbol{\mu}}$ is cyclic if and only if the underlying distribution is involutive.*

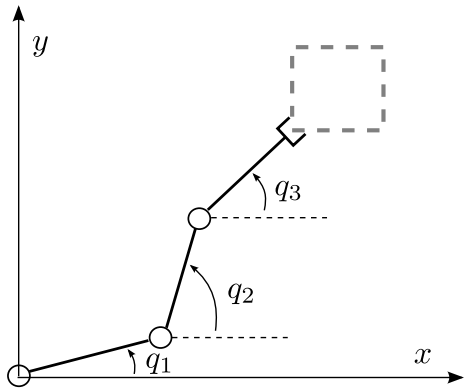

Figure 1.3: *Planar 3R manipulator*

In order to understand the connection between the cyclicicy property and the Lie brackets of $\boldsymbol{G}$, let us consider the planar manipulator sketched in Fig. 1.3, which is redundant with respect to a positioning task in the xy-plane. Assume that the following kinematic control strategy

$$\dot{\boldsymbol{q}} = \boldsymbol{G_1}\dot{x} + \boldsymbol{G_2}\dot{y} = \boldsymbol{G}\left(\boldsymbol{q}\right)\dot{\boldsymbol{\mu}} \tag{1.23}$$

is given and

$$\dot{\boldsymbol{\mu}} = \begin{bmatrix}\dot{x} & \dot{y}\end{bmatrix}^T = \begin{cases} \dot{x} = 1, \dot{y} = 0, & t \in [0, T) \\ \dot{x} = 0, \dot{y} = 1, & t \in [T, 2T) \\ \dot{x} = -1, \dot{y} = 0, & t \in [2T, 3T) \\ \dot{x} = 0, \dot{y} = -1, & t \in [3T, 4T) \end{cases} \tag{1.24}$$

is used as an input aimed at steering the robot to follow a square trajectory in the xy-plane.
Using the Taylor series, it is possible to compute the joint trajectory at time in-

stants $t = 0, T, 2T, 3T$ and $4T$ as a result of the previously defined input $\dot{\boldsymbol{\mu}}$.

$$\begin{aligned}\boldsymbol{q}(T) &= \boldsymbol{q}(0) + T\dot{\boldsymbol{q}}(0) + \frac{T^2}{2}\ddot{\boldsymbol{q}}(0) + \cdots = \\ &= \boldsymbol{q}(0) + T\boldsymbol{G_1}(\boldsymbol{q}(0)) + \frac{T^2}{2}\left.\frac{\partial \boldsymbol{G_1}}{\partial \boldsymbol{q}}\right|_{\boldsymbol{q}=\boldsymbol{q}(0)} \boldsymbol{G_1}(\boldsymbol{q}(0)) + \cdots\end{aligned} \tag{1.25}$$

Similarly

$$\begin{aligned}\boldsymbol{q}(2T) &= \boldsymbol{q}(T) + T\dot{\boldsymbol{q}}(T) + \frac{T^2}{2}\ddot{\boldsymbol{q}}(T) + \cdots = \\ &= \boldsymbol{q}(T) + T\boldsymbol{G_2}(\boldsymbol{q}(T)) + \frac{T^2}{2}\left.\frac{\partial \boldsymbol{G_2}}{\partial \boldsymbol{q}}\right|_{\boldsymbol{q}=\boldsymbol{q}(T)} \boldsymbol{G_2}(\boldsymbol{q}(T)) + \cdots\end{aligned} \tag{1.26}$$

On the other hand, the term $\boldsymbol{G_2}(\boldsymbol{q}(T))$ can be further rearranged as follows

$$\begin{aligned}\boldsymbol{G_2}(\boldsymbol{q}(T)) &= \boldsymbol{G_2}(\boldsymbol{q}(0) + T\boldsymbol{G_1}(\boldsymbol{q}(0)) + \cdots) = \\ &= \boldsymbol{G_2}(q(0)) + T\left.\frac{\partial \boldsymbol{G_2}}{\partial \boldsymbol{q}}\right|_{\boldsymbol{q}=\boldsymbol{q}(0)} \boldsymbol{G_1}(\boldsymbol{q}(0)) + \cdots\end{aligned} \tag{1.27}$$

Repeating the same computations for $\boldsymbol{q}(3T)$ and $\boldsymbol{q}(4T)$, we finally obtain that

$$\lim_{T\to 0} \frac{\boldsymbol{q}(4T) - \boldsymbol{q}(0)}{T^2} = [\boldsymbol{G_1}, \boldsymbol{G_2}] \tag{1.28}$$

which means that the distance from the initial and final configurations of the robot along a closed trajectory can be computed using the Lie brackets of the columns of $\boldsymbol{G}$.

Another aspect that can be easily verified is that any control strategy $\boldsymbol{G}$, either cyclic or not, enforces a Pfaffian constraint like

$$\boldsymbol{Z}(\boldsymbol{q})\,\dot{\boldsymbol{q}} = \boldsymbol{0} \tag{1.29}$$

As a consequence of the Frobenius' theorem, the involutivity condition recalled in Theorem 1.1 is equivalent to the integrability of the given Pfaffian constraint which can be written as follows:

$$\boldsymbol{Z}(\boldsymbol{q})\,\dot{\boldsymbol{q}} = \boldsymbol{A}(\boldsymbol{q})\frac{\partial \boldsymbol{h}}{\partial \boldsymbol{q}}\dot{\boldsymbol{q}} = \boldsymbol{0} \tag{1.30}$$

for some differentiable function $\boldsymbol{h}(\cdot)$ and some non-singular matrix $\boldsymbol{A}$. It is straightforward to notice that a *cyclic control strategy* (i.e. any method $\boldsymbol{G}$ satisfying the condition in Theorem 1.1 enforces the holonomic constraint[3] $\boldsymbol{h}(\boldsymbol{q}) = \boldsymbol{0}$.

[3] With a possible small abuse of notation, we call $\boldsymbol{h}(\boldsymbol{q}) = \boldsymbol{const.}$ a holonomic constraint, meaning that the corresponding Pfaffian is integrable, [85]. Then, without loss of generality, we will express the constraint in the form $\boldsymbol{h}(\boldsymbol{q}) = \boldsymbol{0}$.

It should be mentioned that both (1.19) and (1.20) are complete parameterizations of cyclic kinematic control strategies, meaning that any cyclic method can be written with a proper selection of $u(\cdot)$ and $\boldsymbol{h}(\cdot)$, respectively. The completeness of the parameterization is an important property of the method which will be exploited later in this thesis.
Other methods have been developed. For instance, in [94] a cyclic kinematic control strategy based on optimization is proposed. A solution based on impedance control has been developed in [86]. Recently, in [83] a constructive sufficient condition for holonomy based on the adoption of an integrable 1-form is discussed. In [34] an asymptotically cyclic kinematic control strategy is presented. In the same work, it has been proven that every cyclic method can be achieved by selecting a proper null-space velocity in (1.10).

1.2 Generation of human-like motion patterns

Research interest on Human-Robot Interaction (HRI) has been constantly increasing in the last decades and has reached nowadays an appealing degree of maturity, which encourages first steps towards a technological transfer from research centers to robot manufacturers. On the other hand, measuring the quality of this interaction is a novel field in robotics research and will be extremely useful for future assessments of all efforts in the direction of a more effective HRI. First results exist, ranging from a simple approach, like the so-called "uncanny valley" proposed in [84] (see Fig. 1.4), to a more scientific interpretation supported by physiological measurements, [70].

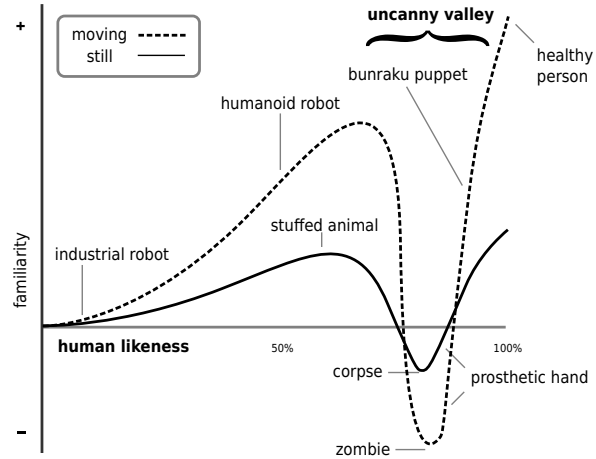

Figure 1.4: *The so-called "uncanny valley" (source Wikipedia), an intuitive correlation between robots' human-likeness and their social acceptance; this correlation is positive until a certain thresholds, called the uncanny valley where such correlation becomes negative*

Pioneer studies about human-machine interaction were based on the assumption of a physical and active exchange of forces/wrenches, [42], [87]. This led to investigate about compliant actuators, human-like control and sensing strategies, [116], to achieve intrinsically safe robots.
However, this cooperation should not just be physically safe, [36], but also psychologically comfortable to the humans: they have, at all times, to feel assured that they understand what the robot's intentions are, and that the robot executes its tasks with motion profiles that humans perceive as natural. For this reason, research in the field of human kinematic analysis has gained interest in recent years and has fostered new ideas and expectations. Next generation manipulators are thus expected to resemble a human-like behavior at kinematic level, in order to avoid any unease or discomfort (like fear or shock) to the nearby humans.
As stated in [61], the main challenge in synthesizing (i.e. reproducing with an articulated manipulator) the human motion is redundancy resolution. In fact, most of the tasks in common human activities entail only a reduced number of constraints with respect to the total number of available DOF. Therefore, a consistent and reliable way to resolve the redundancy should be achieved. Several studies on the motion of the human arm are already available in the literature, ranging from pure kinematic approaches to more complicated neuromuscular analyses. Moreover, most of them are focused on redundancy resolution.
Pioneers of neurophysiological studies proposed the existence of neural strategies to simplify the dimensionality of motor control, [15]. These concepts, well-known nowadays and referred to as *synergies*, were later refined and exploited in different works to explain natural grasping postures [97], reaching movements [95], whole body postures [112], etc.
In [100], the existence of an *uncontrolled manifold* is conjectured. By observing several repetitions of the same pointing task, the authors noticed that the configuration space can be divided into two orthogonal spaces: one of them, which actually depends on the task, is accurately controlled and stabilized meaning that the corresponding variability are lower than those of other (uncontrolled) directions. The former is clearly the space of all possible task motions $\mathcal{R}(\boldsymbol{J})$ introduced so far, while the latter is yet another term to refer to the self-motion manifold. This situation is sketched in Fig. 1.5.

As reported in [44], this variability might be very small compared to the variability allowed by joint redundancy. In [38] the uncontrolled manifold approach has been investigated in bimanual manipulation.
Apart from the neuroscience literature, the research communities of information technology, automatic control, optimization and biomechanics are very active in the field, as well. In particular, many optimality criteria, see e.g. [114] for a detailed review, have been introduced to explain human motions. In this context, the pioneer work [47] presented the first result in modeling natural trajectories

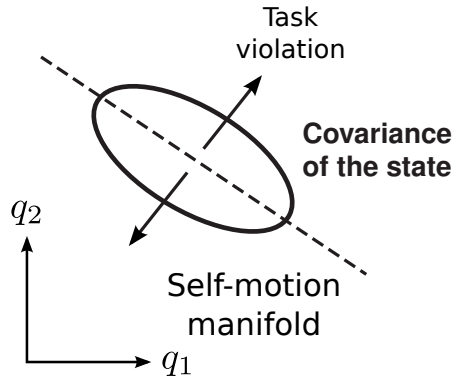

Figure 1.5: *Graphical representation of the uncontrolled manifold hypothesis, adapted from [114]*

for the human arm as resulting of a jerk minimization criterion. Further research led to more detailed objective functions. For instance, in [57] the redundancy of the human arm during a reaching trajectory is resolved minimizing the magnitude of the total work done by joint torques. In [78] an optimization framework has been proposed to resolve the redundancy of the human arm and obtain an optimal posture. In [65] a relationship between the elbow elevation angle (which can be used to parameterize the redundancy) and the hand pose has been investigated and used online to synthesize a human-like behavior of a humanoid robot. The same relationship has been exploited in [58]. In [80] two dexterity measures, the directional dynamic dexterity and the directional kinematic dexterity, have been proposed to predict the human arm pose. They both can be written as follows:

$$u = \frac{1}{\sqrt{\boldsymbol{d}^T \boldsymbol{C}\left(\boldsymbol{q}\right) \boldsymbol{d}}} \tag{1.31}$$

where $\boldsymbol{d}$ is the direction of motion of the hand and $\boldsymbol{C}\left(\boldsymbol{q}\right)$ is either the volume of the kinematic dexterity or of the dynamic dexterity ellipsoids.
More recently, in [61] a biomechanics-based investigation has been performed, where the muscular redundancy has been explicitly taken into account. It was argued that in a static configuration, among all the possible muscular activations, the optimal posture can be predicted using a weighted least-square approach. In particular, it has been experimentally proved that, letting $\boldsymbol{\tau_{ext}}$ be the vector of external torques applied to the arm (e.g. due to gravity), $\boldsymbol{M}\left(\boldsymbol{q}\right)$ the Jacobian of muscle activation and $\boldsymbol{W} = \boldsymbol{W}^T > 0$ a weight matrix, then the following cost function

$$u = \boldsymbol{\tau_{ext}}^T \left(\boldsymbol{M}\left(\boldsymbol{q}\right)^T \boldsymbol{W} \boldsymbol{M}\left(\boldsymbol{q}\right)\right)^{-1} \boldsymbol{\tau_{ext}} \tag{1.32}$$

is minimized over the space of possible arm postures for a given hand pose as

sketched in Fig. 1.6. The same approach is also proposed in [62] to predict the

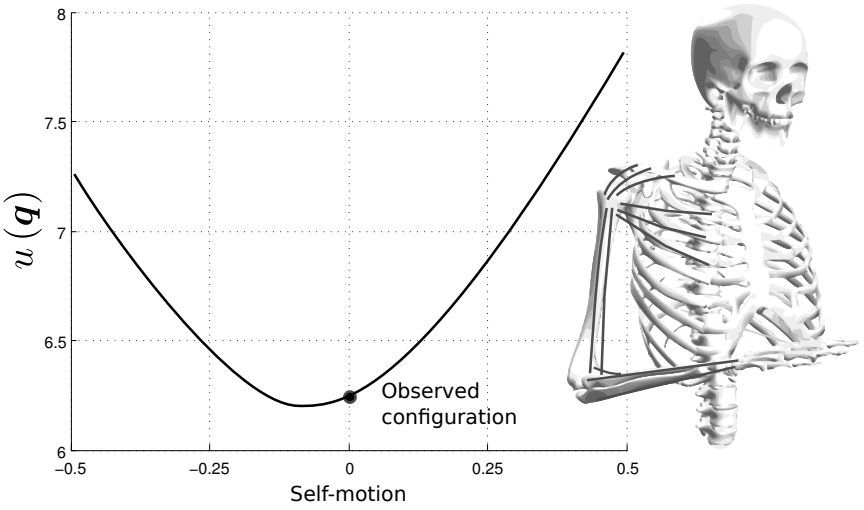

Figure 1.6: *Minimization of a physiologically-based potential energy to explain human arm natural postures, adapted from [63]*

most natural whole-body posture. In [113] the actuation redundancy of a musculoskeletal shoulder model is solved using pseudo-inversion techniques and null-space optimization. Stability and coordination of posture and locomotion have been presented in [54] using quadratic optimization techniques and adaptation. An adaptive control scheme has been proposed also in [110] where an adaptive law for the impedance (see [48]) parameters of the human arm is proposed to explain the typical behavior of humans while interacting with an unknown environment.

Completely different approaches based on learning techniques, Hidden Markov Models (HMM) or Gaussian Mixture Regression (GMR), have been recently proposed to learn natural movements [71], [23], [24].
Finally, from ergonomic studies on the arm posture, in [81] an index called Rapid Upper Limb Assessment (RULA) to measure the discomfort of a particular arm posture has been proposed. The same index has been recently exploited to obtain a shorter and more natural-looking motion for the dual-arm anthropomorphic robot JUSTIN developed at the DLR (German Aerospace Center), see [123].

1.3 Measuring the quality of the human-robot interaction

Assessing the quality of the interaction between humans and the environment by means of measuring their affective state is a novel research field that is gaining interest. Although a well-established way to analyze emotions has not been yet reached, a common framework to represent the emotional state of individuals has been presented in [73]. In particular, the author proposes a characterization of affective experiences by two main dimensions: valence and arousal. Valence represents the pleasantness of stimuli, with positive (or pleasant) at one end and negative (or unpleasant) at the other. For example, happiness has a positive valence, while disgust has a negative valence. The other (and to some extent perpendicular) dimension is called arousal (activation level) which correspond to the state of being awake or reactive to stimuli. For example, sadness has low arousal, whereas surprise has a high level of arousal. The different emotional labels can be plotted at various positions on a 2D plane spanned by these two axes to construct a 2D emotion model, see e.g. [72], as sketched in Fig. 1.7.

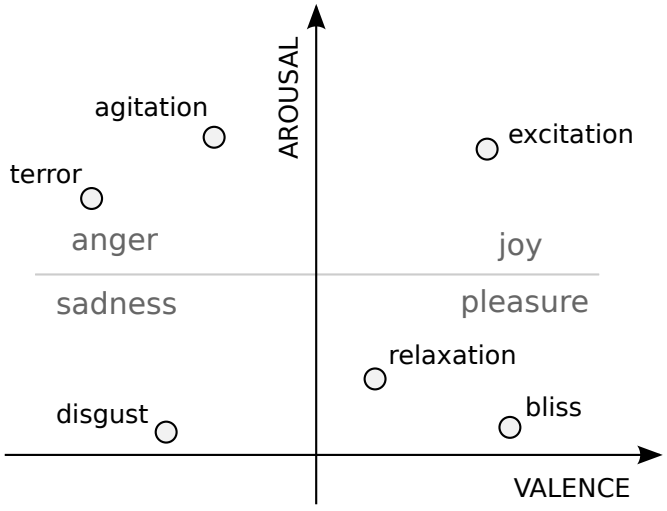

Figure 1.7: *Two-axes representation of the affective state, adapted from [64]*

Statistical correlations of different physiological signals ranging from the heart or respiration rates to the skin conductance or the brain electrical activity with an individual's arousal/valence state have intensively studied, see e.g. [72], [53], [19], [64].
Recently, roboticists started making use of these tools to measure the quality of the (possibly physical) HRI. To some extent, the "uncanney valley" sketched in Fig. 1.4 was the first attempt to throw a bridge between robotics and psychol-

ogy. Pioneers of this field were Kulic and Croft, whose studies gave the basis to the robotics community on the measurement of the affective state of individuals working side-by-side with robots using physiological devices, [69]. In her PhD dissertation, [68], Danica Kulic developed control and planning strategies to enforce a safe HRI. To further improve the perceived safety, the capability of the robot controller to perceive and interpret the human reaction to robot movements, the same work examined the feasibility of using physiological signals in a real-time fashion.

1.4 Open research challenges

While several interesting studies about redundancy resolution and generation of human-like motion patterns for anthropomorphic manipulators can be found in the literature, a concrete integration step towards a more flexible implementation is still missing. In fact, when it comes to industrial robotics, attempts to duplicate the natural motion of the human arm with the motion of the robotic arm must comply with the following constraints:

- end-effector motion (position and orientation) should be accurately controlled;
- the algorithm adopted for path-planning or redundancy resolution must be compliant with the architecture of a real industrial robot controller;
- the mapping of human motion onto an artificial arm should cope with possibly different proportions and kinematic structures.

Finally, the possibility to generate human-like motions for robotic manipulators is always referred to as a possible way to facilitate social acceptance of robots and to ease a natural HRI. However, an adequate verification of this conjecture has never been reported, at least for industrial robots, and thus represents a challenge to be addressed.

Part I

A framework for redundancy resolution

CHAPTER 2

Framework overview

The first contribution of the present dissertation is a complete parameterization of all cyclic kinematic control strategies. By a proper choice of a free function, it is possible to design all the control strategies that guarantee cyclicity of the method for a given manipulator. Then, a framework is proposed which ensures that whenever the redundancy resolution technique has to be changed, a new criterion can be enforced without modifying the core of the inverse kinematics algorithm.
Finally, it will be shown that, using the proposed framework, the robotic programmer might directly select the redundancy resolution technique that best suites her/his application.

2.1 Working assumptions

The possible non-cyclic behavior of a redundant manipulator discussed in the previous Chapter can be a source of problems. In fact, in many industrial applications, the robot is expected to perform repetitive end-effector motions. Using a cyclic kinematic control strategy may result in a predictable joint motion and a simplified programming: many characteristics of the motion (e.g. joint and velocity limits avoidance, singularity avoidance, etc.) can be verified by simulating only the first cycle. In addition, when the robot programmer needs to roll-back

some operations, the adoption of cyclic kinematic control strategies allows a joint consistent roll-back motion. Finally, since in the next future robots will be able to cooperate with human co-workers, their cyclic (repeatable) behavior might be perceived as more natural by nearby humans, facilitating their social acceptance. Many of the solutions reviewed in the previous Chapter, in fact, are difficult to implement in an industrial controller, due to their complexity. For instance, since the null-space basis $\boldsymbol{N}$ is not usually known in closed-form, the algorithm in (1.19) requires the numerical evaluation of the last row of the extended Jacobian. Notice that the constraint to be enforced in order to ensure the cyclicity of the method heavily depends on the application the robot is supposed to work on. For increased flexibility one thus may want to implement (1.19) or (1.20) with different functions $u(\cdot)$ and $\boldsymbol{h}(\cdot)$, respectively, depending on the application. In a research-oriented scenario, while the robot manufacturer implements a proprietary redundancy resolution technique, the researcher might still want to enforce different redundancy resolution criteria without having access to the manufacturer's code.
Finally, notice that all the methodologies presented in the previous Chapter are marginally stable. A stabilizing correction, forming the so-called Closed-Loop Inverse Kinematics (Closed-Loop Inverse Kinematics (CLIK), see e.g. [106]) should be adopted to overcome the drift introduced by the numerical integration when obtaining joint positions from joint velocities. For cyclic kinematic control strategies the stabilization of the holonomic constraint $\boldsymbol{h}(\boldsymbol{q}) = \boldsymbol{0}$ should be tackled, too. In fact, the feedback term in the augmented CLIK algorithm should depend on the holonomic constraint adopted to resolve the redundancy, [125], and therefore on either $u(\cdot)$ or $\boldsymbol{h}(\cdot)$. It follows that such stabilizing feedback action cannot be designed in advance, if the redundancy resolution technique has not been selected yet.
For all these reasons, the redundancy resolution criterion should be decoupled from the implementation of the (stabilized) algorithm adopted to generate the joint variables $\boldsymbol{q}$.
As already introduced, in industrial settings where the embedded code of the robot controller cannot be accessed, algorithms like the extended Jacobian cannot be coded or customized. For this reason, a methodology aimed at the implementation of any holonomic redundancy resolution criterion on top of an existing architecture will be presented in the following. As shown in Fig. 2.1, the block labeled $-\boldsymbol{p}(\cdot)$ can be selected according to the desired redundancy resolution criterion and is implemented on top of the block labeled " Embedded Inverse Kinematics" which represents the algorithm already available in the kinematic robot controller.

In this work we are assuming that the robot controller is already implemented and endowed with an additional set of inputs, say $\boldsymbol{\nu} = \boldsymbol{h}(\boldsymbol{q})$, which can assume

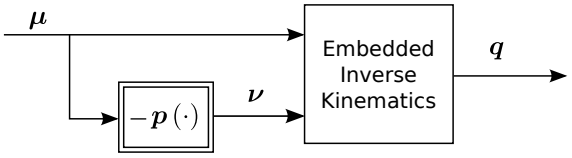

Figure 2.1: *Proposed implementation of the inverse kinematics algorithm*

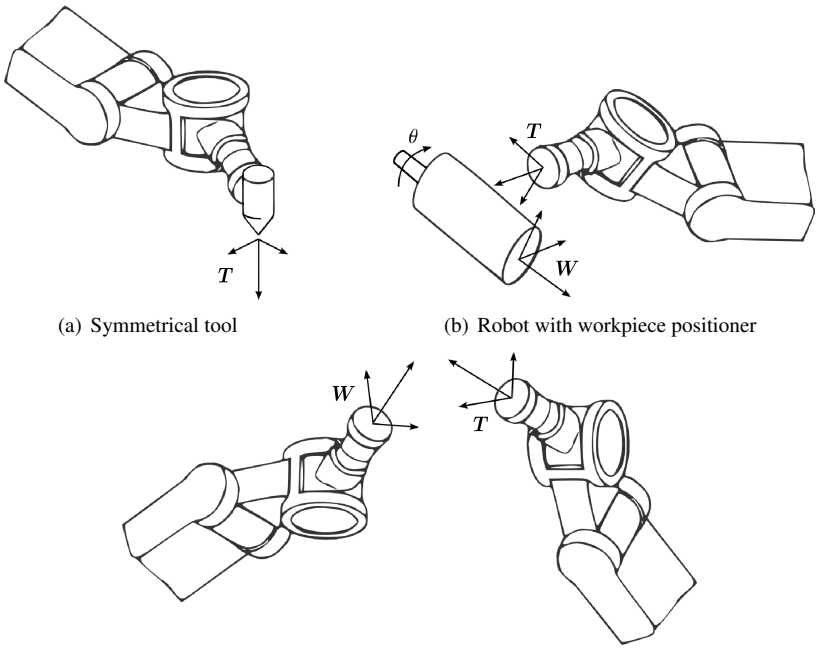

(a) Symmetrical tool

(b) Robot with workpiece positioner

(c) Cooperating manipulators

Figure 2.2: *Examples of redundant robotic systems*

any value, without affecting the task execution. The nature of the inputs $\boldsymbol{\nu}$, and thus the expressions $\boldsymbol{h}(\boldsymbol{q})$, are assumed to be known.
This assumption, which might seem to be restrictive, is actually very common in many industrial robotic systems. Fig. 2.2 shows some examples. Tasks requiring a tool with cylindrical symmetry, see Fig. 2.2(a), can be specified by means of five variables; in this case the variable ν completing the kinematic description could be the Euler angle representing the rotation of frame $\boldsymbol{T}$ around the approach axis. When a workpiece positioner is needed, as in Fig. 2.2(b), task specification requires to constrain the position and orientation of the robot flange $\boldsymbol{T} \in SE(3)$ with respect to the workpiece $\boldsymbol{W} \in SE(3)$. The additional variable ν is represented by the angle θ of the external axis controlling the positioner. Finally, in case of cooperating manipulators, see Fig. 2.2(c), the task description only requires to specify the relative position and orientation of frame

$\boldsymbol{T}$ with respect to frame $\boldsymbol{W}$. In this case, many options for the set of additional variables $\boldsymbol{\nu}$ exists. One is to use the absolute position/orientation of frame $\boldsymbol{W}$, another option involves the definition of an "intermediate frame", between $\boldsymbol{T}$ and $\boldsymbol{W}$, as explained in [29].
In the following a novel methodology to achieve any cyclic kinematic control strategy will be proposed. The methodology is based on the arrangement sketched in Fig. 2.1 where function $\boldsymbol{p}(\cdot)$ can be regarded as a tuning knob that can be adjusted in order to meet some additional requirements. The user-oriented fashion of this architecture will been emphasized and a methodology aimed at tuning such function will been developed, as well.

2.2 Complete parameterization of cyclic control strategies

We prove now that every cyclic kinematic control strategy can be written as follows:

$$\dot{\boldsymbol{q}} = \begin{bmatrix} \boldsymbol{J} \\ \dfrac{\partial \boldsymbol{h}}{\partial \boldsymbol{q}} \end{bmatrix}^{-1} \begin{bmatrix} \dot{\boldsymbol{\mu}} \\ -\dot{\boldsymbol{p}}(\boldsymbol{\mu}) \end{bmatrix} \tag{2.1}$$

where $\boldsymbol{p}(\cdot)$ is a differentiable function related to the desired holonomic redundancy resolution criterion.

Theorem 2.1 (Necessary condition)**.** *Let $\mathcal{S}$ be the set of all non-singular configurations of the Jacobian matrix $\boldsymbol{J}$:*

$$\mathcal{S} = \{\boldsymbol{q} \in \mathbb{R}^n : rank(\boldsymbol{J}) = m\} \tag{2.2}$$

Let $\mathcal{T} \subset \mathcal{S}$ be a simply-connected open subset and suppose that there exists a differentiable function $\boldsymbol{h}(\cdot) : \mathbb{R}^n \to \mathbb{R}^{n-m}$ such that the augmented Jacobian $\boldsymbol{J_A}$

$$\boldsymbol{J_A} = \begin{bmatrix} \boldsymbol{J} \\ \boldsymbol{H} \end{bmatrix} \tag{2.3}$$

is non-singular in $\mathcal{T}$, where $\boldsymbol{H} = \partial \boldsymbol{h}/\partial \boldsymbol{q}$. Let $\boldsymbol{G}$ be a cyclic kinematic control strategy. Then there exists a differentiable function $\boldsymbol{p}(\cdot) : \mathbb{R}^m \to \mathbb{R}^{n-m}$ such that $\dot{\boldsymbol{q}} = \boldsymbol{G}\dot{\boldsymbol{\mu}}$ is the solution of

$$\boldsymbol{J_A}\dot{\boldsymbol{q}} = \begin{bmatrix} \dot{\boldsymbol{\mu}} \\ -\dot{\boldsymbol{p}}(\boldsymbol{\mu}) \end{bmatrix} \tag{2.4}$$

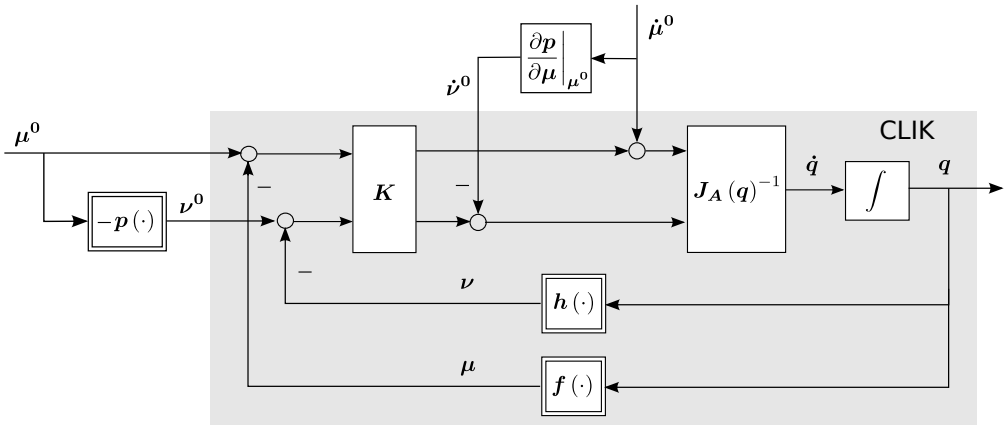

Figure 2.3: *Block diagram of the proposed framework*

Proof. By assumption $\boldsymbol{G}$ is a cyclic kinematic control strategy. It follows that there exists a differentiable function $\boldsymbol{\sigma}(\cdot) : \mathbb{R}^n \to \mathbb{R}^{n-m}$ such that $\boldsymbol{\Sigma G} = \mathbf{0}$, where $\boldsymbol{\Sigma} = \partial \boldsymbol{\sigma} / \partial \boldsymbol{q}$, and $\boldsymbol{\sigma}(\boldsymbol{q}) = \mathbf{0}$. Therefore, the augmented Jacobian $\hat{\boldsymbol{J}}_{\boldsymbol{A}}$

$$\hat{\boldsymbol{J}}_{\boldsymbol{A}} = \begin{bmatrix} \boldsymbol{J} \\ \boldsymbol{\Sigma} \end{bmatrix} \tag{2.5}$$

is non-singular in $\mathcal{T}$ and such that $\dot{\boldsymbol{q}} = \boldsymbol{G}\dot{\boldsymbol{\mu}}$ is the solution of

$$\hat{\boldsymbol{J}}_{\boldsymbol{A}}\dot{\boldsymbol{q}} = \begin{bmatrix} \dot{\boldsymbol{\mu}} \\ \mathbf{0} \end{bmatrix} \tag{2.6}$$

as it can be simply verified by substitution.
For a given initial configuration, since the motion is totally subject to holonomic constraints, at any time the joint configuration $\boldsymbol{q}$ depends only on $\boldsymbol{\mu}$. In other words, in view of the inverse function theorem, which holds because $\hat{\boldsymbol{J}}_{\boldsymbol{A}}$ is non-singular in $\mathcal{T}$, there exists a differentiable inverse function $\boldsymbol{g}(\cdot) : \mathbb{R}^m \to \mathbb{R}^n$ such that

$$\boldsymbol{f}(\boldsymbol{g}(\boldsymbol{\mu})) = \boldsymbol{\mu} \tag{2.7}$$

and the solutions $\boldsymbol{q}$ of $\dot{\boldsymbol{q}} = \boldsymbol{G}\dot{\boldsymbol{\mu}}$ are such that $\boldsymbol{q} = \boldsymbol{g}(\boldsymbol{\mu})$.
Consider now the system:

$$\dot{\boldsymbol{q}} = \boldsymbol{J_A}^{-1} \begin{bmatrix} \dot{\boldsymbol{\mu}} \\ \dot{\boldsymbol{\nu}} \end{bmatrix} \tag{2.8}$$

where $\boldsymbol{\nu}$ is the desired value of the augmented kinematic variable $\boldsymbol{\nu} = \boldsymbol{h}(\boldsymbol{q})$. Since the augmented Jacobian $\boldsymbol{J_A}$ is non singular by assumption, there exists a differentiable inverse function $\boldsymbol{k}(\cdot,\cdot) : \mathbb{R}^n \to \mathbb{R}^n$ such that

$$\boldsymbol{k}(\boldsymbol{f}(\boldsymbol{q}), \boldsymbol{h}(\boldsymbol{q})) = \boldsymbol{q} \tag{2.9}$$

and $\boldsymbol{q} = \boldsymbol{k}(\boldsymbol{\mu}, \boldsymbol{\nu})$ is the solution of (2.8). Then, consider the function $\boldsymbol{p}(\cdot) : \mathbb{R}^m \to \mathbb{R}^{n-m}$

$$\boldsymbol{p}(\cdot) = -\boldsymbol{h}(\boldsymbol{g}(\cdot)) \tag{2.10}$$

which is differentiable since both $\boldsymbol{\sigma}(\cdot)$ and $\boldsymbol{g}(\cdot)$ are differentiable, the former by assumption and the latter in view of the inverse function theorem.
Consider now the following substitution in (2.8):

$$\boldsymbol{\nu} = -\boldsymbol{p}(\boldsymbol{\mu}) = \boldsymbol{h}(\boldsymbol{g}(\boldsymbol{\mu})) \tag{2.11}$$

As previously stated, the solutions of (2.8) are such that

$$\boldsymbol{q} = \boldsymbol{k}(\boldsymbol{\mu}, -\boldsymbol{p}(\boldsymbol{\mu})) = \boldsymbol{k}(\boldsymbol{f}(\boldsymbol{g}(\boldsymbol{\mu})), \boldsymbol{h}(\boldsymbol{g}(\boldsymbol{\mu}))) = \boldsymbol{g}(\boldsymbol{\mu}) \tag{2.12}$$

which means that if $\boldsymbol{p}(\cdot)$ is selected according to (2.10), the solutions of (2.4) and (2.6) are the same. □

Proposition 2.1 (Sufficient condition)**.** *The proposed kinematic control strategy* (2.1) *is cyclic for any choice of* $\boldsymbol{p}(\cdot)$.

Proof. since the constraint $\boldsymbol{\mu} - \boldsymbol{f}(\boldsymbol{q}) = \boldsymbol{0}$ is enforced, it can be simply verified by substitution that the following constraint

$$\boldsymbol{p}(\boldsymbol{f}(\boldsymbol{q})) + \boldsymbol{h}(\boldsymbol{q}) = \boldsymbol{0} \tag{2.13}$$

which is holonomic for any choice of $\boldsymbol{p}(\cdot)$, is enforced by (2.1), as well. □

Remark 2.1. *Theorem 2.1 and Proposition 2.1 represent a complete parameterization of the set of all cyclic redundancy resolution techniques: any cyclic kinematic control strategy can be obtained by choosing a suitable differentiable function* $\boldsymbol{p}(\cdot)$. *In other words, they give a necessary and a sufficient condition, respectively, for a kinematic control strategy to be cyclic.*

Notice that system (2.1), like all kinematic control strategies resolved at velocity level, is not asymptotically stable. Integration with respect to time in order to get the position $\boldsymbol{q}$ may then lead to drifts of the solution. A closed-loop algorithm that stabilizes such system can however be arranged. The asymptotic stability of the resulting CLIK algorithm is proven in the following, together with its asymptotic holonomy.
Define the augmented kinematics as

$$\boldsymbol{f}_{\boldsymbol{A}}(\boldsymbol{q}) = \begin{bmatrix} \boldsymbol{f}(\boldsymbol{q}) \\ \boldsymbol{h}(\boldsymbol{q}) \end{bmatrix}, \boldsymbol{f}_{\boldsymbol{A}}{}^{-1}(\cdot) = \boldsymbol{k}(\cdot, \cdot) \tag{2.14}$$

the augmented task reference as

$$\boldsymbol{\mu}_{\boldsymbol{A}}^{\mathbf{0}} = \begin{bmatrix} \boldsymbol{\mu}^{\mathbf{0}} \\ \boldsymbol{\nu}^{\mathbf{0}} \end{bmatrix} = \begin{bmatrix} \boldsymbol{\mu}^{\mathbf{0}} \\ -\boldsymbol{p}\left(\boldsymbol{\mu}^{\mathbf{0}}\right) \end{bmatrix} \tag{2.15}$$

and compute its time derivative as

$$\dot{\boldsymbol{\mu}}_{\boldsymbol{A}}^{\mathbf{0}} = \begin{bmatrix} \dot{\boldsymbol{\mu}}^{\mathbf{0}} \\ -\dot{\boldsymbol{p}}\left(\boldsymbol{\mu}^{\mathbf{0}}\right) \end{bmatrix} = \begin{bmatrix} \dot{\boldsymbol{\mu}}^{\mathbf{0}} \\ -\left.\frac{\partial \boldsymbol{p}}{\partial \boldsymbol{\mu}}\right|_{\boldsymbol{\mu}^{\mathbf{0}}} \dot{\boldsymbol{\mu}}^{\mathbf{0}} \end{bmatrix} \tag{2.16}$$

Proposition 2.2. *Let $\mathcal{T} \subset \mathcal{S}$ be a simply-connected open subset where the augmented Jacobian $\boldsymbol{J_A}$ is non-singular and $-\boldsymbol{K}$ an $n \times n$ Hurwitz matrix. Consider the following dynamical system (CLIK):*

$$\dot{\boldsymbol{q}} = {\boldsymbol{J_A}}^{-1}\left(\dot{\boldsymbol{\mu}}_{\boldsymbol{A}}^{\mathbf{0}} + \boldsymbol{K}\left(\boldsymbol{\mu}_{\boldsymbol{A}}^{\mathbf{0}} - \boldsymbol{f_A}\left(\boldsymbol{q}\right)\right)\right) \tag{2.17}$$

which is sketched in Fig. 2.3. Then the equilibrium $\boldsymbol{\mu}_{\boldsymbol{A}}^{\mathbf{0}} - \boldsymbol{f_A}\left(\boldsymbol{q}\right) = \mathbf{0}$ is asymptotically stable for the given system.

Proof. Consider the following change of variables $\boldsymbol{e_A} = \boldsymbol{\mu}_{\boldsymbol{A}}^{\mathbf{0}} - \boldsymbol{f_A}\left(\boldsymbol{q}\right)$, then

$$\dot{\boldsymbol{e}}_{\boldsymbol{A}} = \dot{\boldsymbol{\mu}}_{\boldsymbol{A}}^{\mathbf{0}} - \boldsymbol{J_A}\dot{\boldsymbol{q}} = -\boldsymbol{K}\boldsymbol{e_A} \tag{2.18}$$

which means that $\boldsymbol{e_A} \to \mathbf{0}$ as $t \to +\infty$. □

Corollary 2.1. *Under the assumptions of Proposition 2.2, the solution of* (2.17) *is an asymptotically cyclic kinematic control strategy.*

Proof. It has been proven that under the assumptions of Proposition 2.2, it follows that $\boldsymbol{e_A}\left(\boldsymbol{q}, \boldsymbol{\mu}_{\boldsymbol{A}}^{\mathbf{0}}\right) \to \mathbf{0}$. Therefore, $\boldsymbol{f}\left(\boldsymbol{q}\right) - \boldsymbol{\mu}^{\mathbf{0}} \to \mathbf{0}$ and $\boldsymbol{p}\left(\boldsymbol{\mu}^{\mathbf{0}}\right) + \boldsymbol{h}\left(\boldsymbol{q}\right) \to \mathbf{0}$. Then the following holonomic constraint is asymptotically enforced:

$$\boldsymbol{p}\left(\boldsymbol{f}\left(\boldsymbol{q}\right)\right) + \boldsymbol{h}\left(\boldsymbol{q}\right) = \mathbf{0} \tag{2.19}$$

□

2.3 Selection of the parameter $p(\cdot)$

In this Section, a methodology for the selection of the parameter function $\boldsymbol{p}(\cdot)$ that best suites the user's requirement is discussed.

Assume then that the function $\boldsymbol{h}(\cdot)$ is given as a redundancy resolution criterion embedded in the CLIK algorithm and suppose that the holonomic constraint $\boldsymbol{\sigma}(\boldsymbol{q}) = \mathbf{0}$ has been found to be an appropriate way to solve the redundancy for a given manipulator, where $\boldsymbol{\sigma}(\cdot) : \mathbb{R}^n \to \mathbb{R}^{n-m}$ is a differentiable function. The following problem naturally arises: how can the function $\boldsymbol{p}(\cdot)$ be selected in order to force satisfaction of the constraint $\boldsymbol{\sigma}(\boldsymbol{q}) = \mathbf{0}$?
In general, an exact solution of this problem does not exist or its calculation is too time-consuming to be performed on-line. On the other hand, it is possible to select the function $\boldsymbol{p}(\cdot)$ in order to make the holonomic constraint $\boldsymbol{p}(\boldsymbol{f}(\boldsymbol{q})) + \boldsymbol{h}(\boldsymbol{q}) = \mathbf{0}$ as similar as possible to $\boldsymbol{\sigma}(\boldsymbol{q}) = \mathbf{0}$.
In the following, we assume, for simplicity but without any lack of generality, that $n - m = 1$. In particular, in case of multiple degrees of redundancy, namely when $n - m > 1$, the approach can be iterated over the number of the $n - m$ redundant degrees of freedom. An application to the case of multiple degrees of redundancy will be discussed in Chapter 3.
In order to simplify the selection of the function $p(\cdot)$, it is convenient to reduce the problem domain to an a-priori known functional space $\mathcal{P}$ (e.g. multivariate polynomials, multivariate trigonometric polynomials, multivariate wavelets, etc.).
Once a basis $p_1(\cdot), \cdots, p_w(\cdot)$ of the functional space has been defined, every function $p(\cdot) \in \mathcal{P}$ can be written as a linear combination of the basis functions as follows:

$$\mathcal{P} = \{p(\cdot) = c_1 p_1(\cdot) + \cdots + c_w p_w(\cdot) = \hat{\boldsymbol{p}}(\boldsymbol{\cdot})^T \boldsymbol{c}\} \tag{2.20}$$

where $\boldsymbol{c} = \begin{bmatrix} c_1 & \dots & c_w \end{bmatrix}^T$ and $\hat{\boldsymbol{p}}(\boldsymbol{\cdot})^T = \begin{bmatrix} p_1(\cdot) & \dots & p_w(\cdot) \end{bmatrix}$.
The selection of the parameter $p(\cdot)$ that best approximates the requirement specification $\sigma(\boldsymbol{q}) = 0$ can be formalized as follows.

Definition 2.1 (Problem statement)**.** *Let $\mathcal{P} \subseteq \mathcal{C}^1(\mathbb{R}^m)$ be a functional space, then find $p^0(\cdot) = \hat{\boldsymbol{p}}(\cdot)^T \boldsymbol{c^0}$ where*

$$\boldsymbol{c^0} = \underset{\boldsymbol{c} \in \mathbb{R}^w}{\arg\min} \| \hat{\boldsymbol{p}}(\boldsymbol{f}(\cdot))^T \boldsymbol{c} + h(\cdot) \|, \, \boldsymbol{q} : \sigma(\boldsymbol{q}) = 0 \tag{2.21}$$

Symbol $\|v(\cdot)\|$ denotes a proper, possibly weighted, norm, e.g. the $\mathcal{L}_2$-norm or the $\mathcal{L}_\infty$-norm of a generic function $v(\cdot)$. As stated in Theorem 2.1, the existence of a function $p(\cdot)$ that exactly enforces the user-defined requirement is guaranteed away from singularities. However, in non-singular configuration where the hypotheses of the Theorem are close to be violated, the function $p(\cdot)$ might be non-smooth. In the neighborhood of such configurations it is not convenient to accurately approximate the desired constraint $\sigma(\boldsymbol{q}) = 0$. Therefore, the worst case approximation given by the maximum-norm is not a reasonable choice. In

addition, the adoption of the maximum-norm will result in the typical $min-max$ problem which is usually difficult to deal with.
Using the $\mathcal{L}_2$-norm, the solution can be computed minimizing the cost function with respect to the parameter $\boldsymbol{c}$, yielding the following optimal solution:

$$\boldsymbol{c^0} = \boldsymbol{A}^{-1}\boldsymbol{b} \tag{2.22}$$

where

$$\begin{aligned} \boldsymbol{A} &= \lim_{M\to+\infty} \frac{1}{M}\sum_{i=1}^{M} \hat{\boldsymbol{p}}\left(\boldsymbol{\mu^{(i)}}\right)\hat{\boldsymbol{p}}\left(\boldsymbol{\mu}^{(i)}\right)^T \\ \boldsymbol{b} &= -\lim_{M\to+\infty} \frac{1}{M}\sum_{i=1}^{M} \hat{\boldsymbol{p}}\left(\boldsymbol{\mu^{(i)}}\right)\nu^{(i)} \end{aligned} \tag{2.23}$$

$\boldsymbol{\mu^{(i)}} = \boldsymbol{f}\left(\boldsymbol{q^{(i)}}\right)$, $\nu^{(i)} = h\left(\boldsymbol{q^{(i)}}\right)$ and $\boldsymbol{q^{(i)}}, i = 1, \cdots, M$ are M randomly selected points from a uniform distribution on the configuration manifold $\sigma(\boldsymbol{q}) = 0$.

In the next Proposition, we provide an assessment of the accuracy of the proposed approximation which guarantees that, provided that the value of the cost function is sufficiently small, the user requirement $\boldsymbol{\sigma}(\boldsymbol{q}) = \boldsymbol{0}$ is approximately enforced with a bounded error.

Proposition 2.3. *Assume that the hypotheses of Theorem 2.1 hold, functions $\boldsymbol{f}(\cdot), \boldsymbol{h}(\cdot), \boldsymbol{\sigma}(\cdot)$ are at least twice differentiable in $\mathcal{T}$, and let*

$$F^0 = \left\|\hat{\boldsymbol{p}}\left(\boldsymbol{f}(\cdot)\right)^T \boldsymbol{c^0} + \boldsymbol{h}(\cdot)\right\| = \left\|\boldsymbol{p^0}\left(\boldsymbol{f}(\cdot)\right) + \boldsymbol{h}(\cdot)\right\| \tag{2.24}$$

the value of the cost function corresponding to the optimal approximation $\boldsymbol{p^0}(\cdot)$ of $\boldsymbol{p}(\cdot)$.
Then, the error on the user requirement is bounded from above by a positive limited quantity L such that $L \to 0$ as $F^0 \to 0$.

Proof. Assume $\boldsymbol{p^0}(\cdot) + \boldsymbol{\delta p}(\cdot) = \boldsymbol{p}(\cdot)$ where $\boldsymbol{\delta p}(\cdot)$ is a function describing the approximation error. If $\boldsymbol{p}(\cdot)$ is used, the output of the kinematic inversion is

$$\boldsymbol{q} = \boldsymbol{k}\left(\boldsymbol{\mu}, -\boldsymbol{p^0}(\boldsymbol{\mu}) - \boldsymbol{\delta p}(\boldsymbol{\mu})\right) \tag{2.25}$$

and, in view of Theorem 2.1, is consistent with the constraint $\boldsymbol{\sigma}(\boldsymbol{q}) = \boldsymbol{0}$.
When $\boldsymbol{p^0}(\cdot)$ is used in place of $\boldsymbol{p}(\cdot)$, a different output, say $\boldsymbol{q^0} = \boldsymbol{q} + \boldsymbol{\delta q}$, is obtained, where

$$\boldsymbol{q^0} = \boldsymbol{k}\left(\boldsymbol{\mu}, -\boldsymbol{p^0}(\boldsymbol{\mu})\right) \tag{2.26}$$

Therefore, applying Taylor series (with the Lagrange form of the remainder) we have that

$$\boldsymbol{\delta q} = \boldsymbol{q^0} - \boldsymbol{q} = \left.\frac{\partial \boldsymbol{k}}{\partial \boldsymbol{\nu}}\right|_{-\boldsymbol{p^0}(\boldsymbol{\mu})} \boldsymbol{\delta p}\left(\boldsymbol{\mu}\right) + \boldsymbol{R_2}\left(\boldsymbol{\delta p}\left(\boldsymbol{\mu}\right)\right) \tag{2.27}$$

where the right-hand side is a limited quantity. In fact, since both $\boldsymbol{f}\left(\cdot\right)$ and $\boldsymbol{h}\left(\cdot\right)$ are twice differentiable, it follows that $\boldsymbol{k}\left(\cdot,\cdot\right)$ is twice differentiable in $\mathcal{T}$, as well. Moreover

$$\begin{aligned} \boldsymbol{\sigma}\left(\boldsymbol{q^0}\right) = \boldsymbol{\sigma}\left(\boldsymbol{q}+\boldsymbol{\delta q}\right) = \left.\frac{\partial \boldsymbol{\sigma}}{\partial \boldsymbol{q}}\right|_{\boldsymbol{q}} \boldsymbol{\delta q} + \boldsymbol{R_1}\left(\boldsymbol{\delta q}\right) = \\ = \left.\frac{\partial \boldsymbol{\sigma}}{\partial \boldsymbol{q}}\right|_{\boldsymbol{q}} \left.\frac{\partial \boldsymbol{k}}{\partial \boldsymbol{\nu}}\right|_{-\boldsymbol{p^0}(\boldsymbol{\mu})} \boldsymbol{\delta p}\left(\boldsymbol{\mu}\right) + \left.\frac{\partial \boldsymbol{\sigma}}{\partial \boldsymbol{q}}\right|_{\boldsymbol{q}} \boldsymbol{R_2}\left(\boldsymbol{\delta p}\left(\boldsymbol{\mu}\right)\right) + \boldsymbol{R_1}\left(\boldsymbol{\delta q}\right) \end{aligned} \tag{2.28}$$

where the right-hand side is again a limited quantity since $\boldsymbol{\sigma}\left(\cdot\right)$ is twice differentiable.
Recalling (2.25), (2.26) and (2.27), since $\boldsymbol{q}, \boldsymbol{q^0}$ and $\boldsymbol{\delta q}$ are functions of $\boldsymbol{\mu}$, we have that

$$\left\|\boldsymbol{\sigma}\left(\boldsymbol{q^0}\left(\cdot\right)\right)\right\| \leq L \tag{2.29}$$

where

$$L = \left\|\frac{\partial \boldsymbol{\sigma}}{\partial \boldsymbol{q}}\frac{\partial \boldsymbol{k}}{\partial \boldsymbol{\nu}}\right\| \left\|\boldsymbol{\delta p}\left(\cdot\right)\right\| + \left\|\frac{\partial \boldsymbol{\sigma}}{\partial \boldsymbol{q}}\boldsymbol{R_2}\left(\boldsymbol{\delta p}\left(\cdot\right)\right)\right\| + \left\|\boldsymbol{R_1}\left(\boldsymbol{\delta q}\left(\cdot\right)\right)\right\| \tag{2.30}$$

is a positive limited quantity.
On the other hand, since $\boldsymbol{p}\left(\boldsymbol{f}\left(\boldsymbol{q}\right)\right) + \boldsymbol{h}\left(\boldsymbol{q}\right) = \boldsymbol{0}$ is enforced for all $\boldsymbol{q} : \boldsymbol{\sigma}\left(\boldsymbol{q}\right) = \boldsymbol{0}$, the optimal value of the cost function can be written as follows

$$F^0 = \left\|\boldsymbol{p}\left(\boldsymbol{f}\left(\cdot\right)\right) + \boldsymbol{\delta p}\left(f\left(\cdot\right)\right) + \boldsymbol{h}\left(\cdot\right)\right\| = \left\|\boldsymbol{\delta p}\left(\cdot\right)\right\| \tag{2.31}$$

Finally, when $F^0 \to 0$, from (2.31) we notice that $\left\|\boldsymbol{\delta p}\left(\cdot\right)\right\| \to 0$, as well. The fact that $L \to 0$ is then a direct consequence of the convergence of the Taylor's series. □

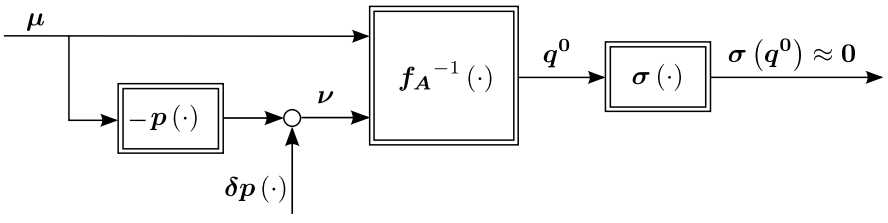

Figure 2.4: *Influence of the approximation on the user-requirement*

Remark 2.2. *Using* (2.22) *and* (2.23) *it is possible to select, from an a-priori defined functional space, a function* $\boldsymbol{p^0}(\cdot)$ *that best approximates function* $\boldsymbol{p}(\cdot)$ *of Theorem 2.1. Proposition 2.3 guarantees that the user requirement is actually enforced with a small bounded error, provided that the optimal value of the cost function* F^0 *is small enough. Figure 2.4 shows the effect of the approximation error* $\boldsymbol{\delta p}(\cdot)$ *on the user requirement* $\boldsymbol{\sigma}(\boldsymbol{q})$ *which have been proved to be related as follows*

$$L \approx \left\| \frac{\partial \boldsymbol{\sigma}}{\partial \boldsymbol{q}} \frac{\partial \boldsymbol{k}}{\partial \boldsymbol{\nu}} \right\| \|\boldsymbol{\delta p}(\cdot)\| \tag{2.32}$$

On the other hand, a new solution can be computed by increasing the complexity of the functional space, e.g. by adding new basis functions.
In the light of the above discussion, the natural way to tackle the approximation problem is to adopt a greedy algorithm, e.g. the one reported in Appendix B. The user might select a threshold F^0_{TH} *and add new regressors until* $F^0 \leq F^0_{TH}$ *in order to achieve a corresponding (and satisfactory) value of* L *such that* (2.29) *holds.*

2.4 Potentialities of the method

The block diagram of the framework for redundancy resolution resulting from the analysis of the previous Section (see Fig. 2.3) shows that different criteria can be used to resolve the redundancy without modifying the core of the CLIK algorithm. In fact, the function $\boldsymbol{p}(\cdot)$ is external to the augmented CLIK. Moreover, the stabilization method, namely the selection of the matrix $\boldsymbol{K}$, does not depend on the selected function $\boldsymbol{p}(\cdot)$. In other words, the system in (2.1) can be stabilized no matter what the function $\boldsymbol{p}(\cdot)$ is.
As one can see from Fig. 2.3, a general cyclic kinematic control strategy is strictly related to the way the augmenting task variable $\boldsymbol{\nu}$ is planned. In fact, based on the previous results, any cyclic solution of the kinematic inverse problem can be achieved planning the variable $\boldsymbol{\nu^0}$ as a function of the main task $\boldsymbol{\mu^0}$, i.e. $\boldsymbol{\nu^0} = -\boldsymbol{p}(\boldsymbol{\mu^0})$.
Finally, notice that the redundancy resolution technique does not depend on the particular way the inverse kinematics algorithm has been implemented in the robot controller. In particular, in Fig. 2.3, the inverse (augmented) Jacobian approach has been selected. As a matter of fact, any numerical method can be used to compute the inverse function $\boldsymbol{f_A}^{-1}(\cdot) = \boldsymbol{k}(\cdot,\cdot)$ (which exists away from singularities of $\boldsymbol{J_A}$), e.g. the (augmented) transposed Jacobian [103], namely

$$\dot{\boldsymbol{q}} = \boldsymbol{J_A}^T \boldsymbol{K} \boldsymbol{e_A} \tag{2.33}$$

a nonlinear programming approach [43]:

$$\boldsymbol{q} = \arg\min_{\hat{\boldsymbol{q}}} \left\| \boldsymbol{f_A}\left(\hat{\boldsymbol{q}}\right) - \boldsymbol{\mu_A^0} \right\| \tag{2.34}$$

or even a closed-form solution, resulting in a more flexible implementation.
Figure 2.5 shows the modularity of the proposed architecture. The algorithm responsible of generating the joint position references, labeled with $\boldsymbol{f_A}^{-1}(\cdot)$, is totally decoupled from the redundancy resolution technique, which is embedded in the block $-\boldsymbol{p^0}(\cdot)$. This framework is convenient from both the robot manufacturers and the robot users standpoints. As for the former, the kinematic controller can be implemented no matter what the redundancy resolution technique to be used is, while the latter is anyway allowed to select the redundancy resolution algorithm that best fits the desired application. The robotic programmer might select directly the redundancy resolution criterion, i.e. the function $\boldsymbol{\sigma}(\cdot)$ based on the requirement of the application. The algorithm that generates the parameter $\boldsymbol{p^0}(\cdot)$, namely (2.22) and (2.23), can be embedded in a common robot programming environment.

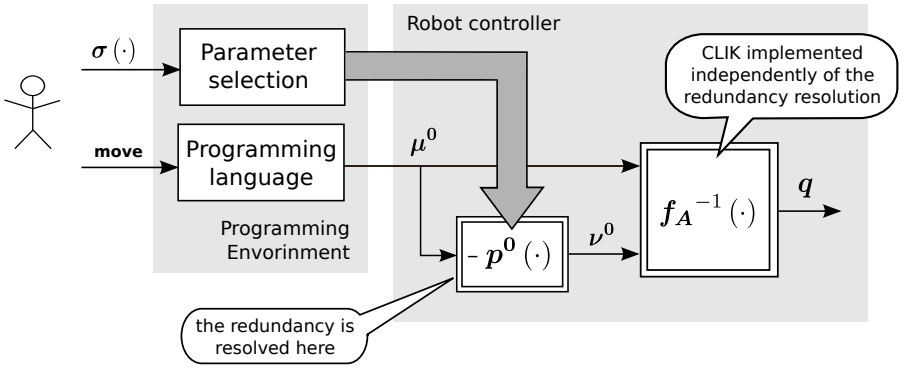

Figure 2.5: *User-oriented fashion of the proposed framework*

2.5 A detailed experimental case study

In this Section the proposed framework is used in a case study of practical interest. A 6-axes ABB IRB 140 industrial robot and a generic task requiring a cylindrical tool are considered. The robot is controlled by an ABB IRC 5 cabinet. When a tool with cylindrical symmetry is used, re-orienting the tool around its axis does not affect the task execution. This happens in many industrial applications, such as painting, welding, deburring or cutting. Since usually the tool axis does not coincide with the axis of the last revolute joint, the redundant degree of freedom can be exploited in order to achieve an additional requirement.

Assume that the pose of the tool can be described by means of a set of three Cartesian variables, say x, y and z, and three ZYZ Euler angles, say ρ, θ and ϕ. Then ϕ, the third Euler angle, can be freely specified without affecting the task execution. On the other hand, the robot controller is expected to be assigned a full description of the tool pose, and does not allow any modification of the embedded code. We will explore possible advantages related to the use of the proposed framework compared to a trivial assignment of variable ϕ.
Let

$$\boldsymbol{\mu} = \begin{bmatrix} x & y & z & \rho & \theta \end{bmatrix}^T \quad \nu = \phi \tag{2.35}$$

and define

$$\boldsymbol{\mu} = \boldsymbol{f}(\boldsymbol{q}) \quad \nu = h(\boldsymbol{q}) \tag{2.36}$$

the task kinematics and the augmenting task description, respectively.
As a redundancy resolution technique, suppose the user wants to maximize the manipulability measure, [122]. Then, applying the extended Jacobian method in (1.17) and (1.18), the user requirement can be turned into the following constraint:

$$\sigma(\boldsymbol{q}) = \boldsymbol{N}^T \left(\frac{\partial u}{\partial \boldsymbol{q}} \right)^T = 0 \tag{2.37}$$

where $\boldsymbol{N}$ is a null-space basis of $\boldsymbol{J} = \partial \boldsymbol{f} / \partial \boldsymbol{q}$, $u = \sqrt{\det\left(\boldsymbol{J}_{\boldsymbol{\omega}} \boldsymbol{J}_{\boldsymbol{\omega}}{}^T\right)}$ and $\boldsymbol{J}_{\boldsymbol{\omega}}$ is the geometrical Jacobian of the manipulator.
A number of $M = 5000$ Monte Carlo samples have been generated, consistent with the optimality constraint $\sigma(\boldsymbol{q}) = 0$, using the algorithm described in Appendix A. Then, the function $p^0(\cdot)$ has been selected within a functional space composed of polynomials and inverse trigonometric functions in the Cartesian variables of the task and a modified truncated Fourier series (which usually guarantees a faster convergence compared to the common Fourier series, [51]) in the orientation variables. The greedy algorithm has been run three times for decreasing values of the acceptance threshold F_{TH}^0 introduced at the end of Section 2.3, yielding

$$p^0_{20\,\mathrm{deg}}(\boldsymbol{\mu}) = -1.16 atan2(x, y) + 3.21 - 1.42 \sin(\rho) \tag{2.38a}$$

$$\begin{aligned} p^0_{10\,\mathrm{deg}}(\boldsymbol{\mu}) = &-2.70\sqrt{x^2 + z^2} - 1.13 atan2(x, y) + 4.86 \\ &+ 1.59 \cos(0.5\rho) \cos(0.5\theta) - 1.38 \sin(\rho) \end{aligned} \tag{2.38b}$$

$$\begin{aligned} p^0_{5\,\mathrm{deg}}(\boldsymbol{\mu}) = &-1.12 atan2(x, y) - 1.63 \sin(\rho) + 4.47 + \\ &- 2.40\sqrt{x^2 + z^2} - 0.64\sqrt{y^2 + z^2} + 0.46 \cos(0.5\rho) + \\ &+ 0.28 \sin(2\rho) + 1.80 \cos(0.5\rho) \cos(0.5\theta) \end{aligned} \tag{2.38c}$$

corresponding to $F_{TH}^0 = 20, 10, 5\,\mathrm{deg}$, respectively.
The algorithm sketched in Fig. 2.5 has been implemented on the industrial controller without adding any additional hardware. The block labeled with $\boldsymbol{f_A}^{-1}(\cdot)$ represents the proprietary kinematic inversion algorithm. The redundancy resolution criterion has been coded directly in RAPID[1] and the function $p^0(\cdot)$ has been implemented as a function call.
The robotic programmer specified the task through a list of tool poses to be interpolated online with linear and circular paths. This specification was done without taking care of the functional redundancy of the task (and without using the proposed approach) and, for this reason, will be referred to as *trivial redundancy resolution*. For the same task, the orientation of the tool is online adjusted within the task null-space using the proposed method which is aimed at solving the functional redundancy by enforcing the maximization of the manipulability measure. Finally, for the same task, Baillieul's extended Jacobian has been run in simulation[2] for comparison. Experimental and simulated time histories of the manipulability measure are shown in Fig. 2.6. As one can see, even though it is

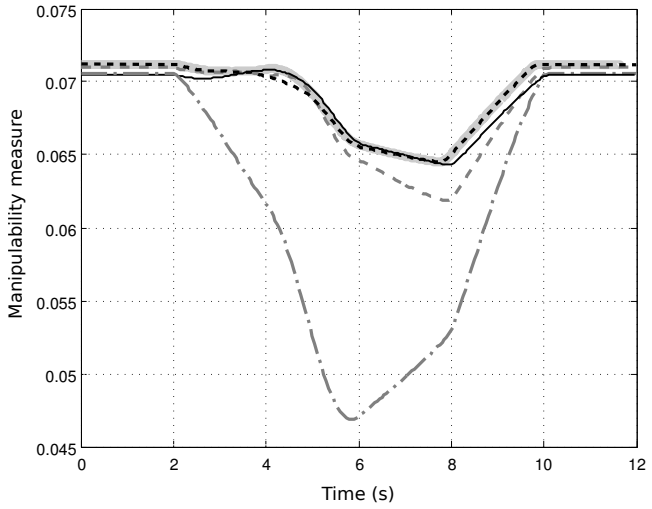

Figure 2.6: *Manipulability measure: extended Jacobian (simulated, solid gray), proposed method with $F_{TH}^0 = 20\,\mathrm{deg}$ (experimental, dashed gray), proposed method with $F_{TH}^0 = 10\,\mathrm{deg}$ (experimental, solid black), proposed method with $F_{TH}^0 = 5\,\mathrm{deg}$ (experimental, dashed black) and trivial redundancy resolution (experimental, dot-dashed gray)*

not possible to directly implement the extended Jacobian method, using the function $p^0(\cdot)$ in (2.38) and the proposed methodology it is still possible to enforce the maximization of the manipulability measure, without any modification of the

[1] RAPID is the programming language for ABB robots.
[2] Implementation of the extended Jacobian requires a modification of the code embedded in the controller and, for this reason, can be only simulated.

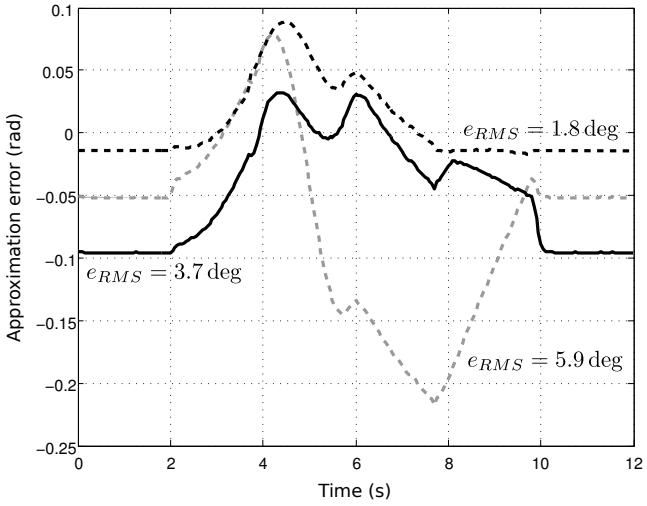

Figure 2.7: *Approximation error $\delta p\,(\boldsymbol{\mu})$: proposed method with $F^0_{TH} = 20\,\mathrm{deg}$ (experimental, dashed gray), proposed method with $F^0_{TH} = 10\,\mathrm{deg}$ (experimental, solid black) and proposed method with $F^0_{TH} = 5\,\mathrm{deg}$ (experimental, dashed black)*

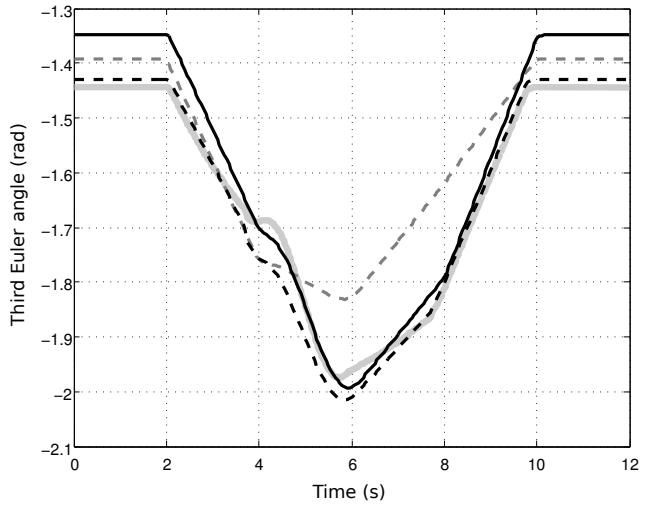

Figure 2.8: *Third Euler angle ν: extended Jacobian (simulated, solid gray), proposed method with $F^0_{TH} = 20\,\mathrm{deg}$ (experimental, dashed gray), proposed method with $F^0_{TH} = 10\,\mathrm{deg}$ (experimental, solid black) and proposed method with $F^0_{TH} = 5\,\mathrm{deg}$ (experimental, dashed black)*

manufacturer's embedded code. On the other hand, if the motion of the robot is programmed without taking care of the functional redundancy, a significantly lower manipulability measure was obtained. Moreover, consistent with Proposition 2.3, the achievement of the user requirement is more and more effective as

the threshold F^0_{TH}, and thus $F^0 \leq F^0_{TH}$, decreases. The same arguments finally explain the behavior of the approximation error $\delta p\,(\boldsymbol{\mu})$ shown in Fig. 2.7 which is progressively smaller.
Finally, in order to verify the statement of Proposition 2.3, the bound L has been computed using the Monte Carlo samples using the following approximation:

$$L \approx \left\| \frac{\partial \sigma}{\partial \boldsymbol{q}} \frac{\partial \boldsymbol{k}}{\partial \nu} \right\| F^0_{TH} \tag{2.39}$$

Figure 2.9 shows the time history of $\sigma\,(\boldsymbol{q})$ during the experiments for the three different values of the acceptance threshold F^0_{TH}. Notice that, as the threshold decreases, the user-defined holonomic requirement, which implies $\sigma\,(\boldsymbol{q}) = 0$, is more accurately achieved. As expected, in all the three experiments the error on user-requirement is bounded and such that $\|\sigma\,(\boldsymbol{q})\| \leq L$ as guaranteed by Proposition 2.3.

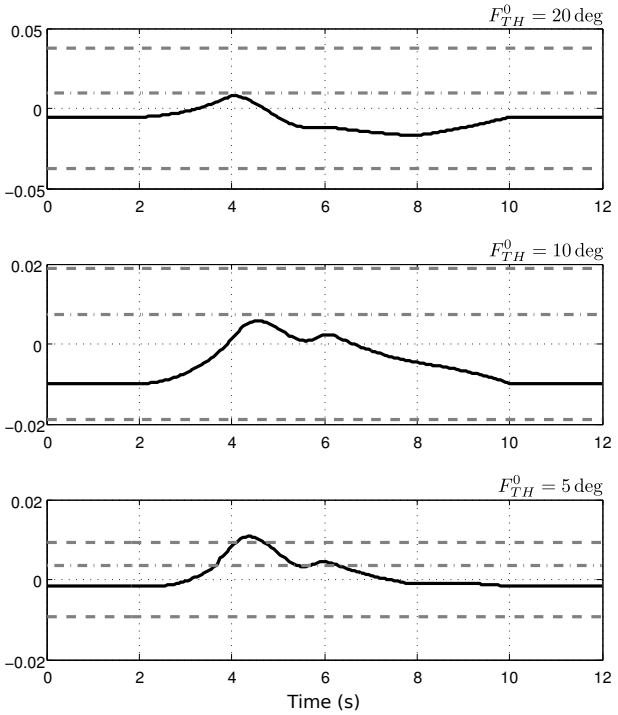

Figure 2.9: *Approximation of the user-requirement $\sigma\,(\boldsymbol{q}) = 0$: proposed method with $F^0_{TH} = 20\,\mathrm{deg}, 10\,\mathrm{deg}$ and $5\,\mathrm{deg}$ (experimental, solid black), the corresponding norm $\|\sigma\,(\boldsymbol{q})\|$ (experimental, dot-dashed gray) and the computed bounds $\pm L$ (dashed gray)*

2.5.1 Actual implementation

In the following the implementation details of the block diagram in Fig. 2.5 are presented. The input of the embedded inverse kinematics, i.e. the block labeled $\boldsymbol{f_A}^{-1}(\cdot)$, is a full description of the robot pose, in terms of Cartesian position of the Tool Center Point (TCP) and orientation of the tool (expressed using unit quaternions). The first two ZYZ Euler angle, i.e. ρ and θ, are extracted from the quaternion, while the third is discarded and replaced using $p^0(\cdot)$ in (2.38c). Then, the corresponding set of Euler angles is turned into a unit quaternion which is used to feed the trajectory interpolator and the subsequent kinematic inversion algorithm. An excerpt of the RAPID code implementation is given in the following.

```
! main procedure
PROC main()
 MoveL p(p0), v100, fine, tool;
 MoveL p(pw1),          v600\T:=2, z10,  tool;
 MoveC p(pw2), p(pw3), v600\T:=2, z10,  tool;
 MoveL p(pw4),          v600\T:=2, z10,  tool;
 MoveL p(pw0),          v600\T:=2, fine, tool;
ENDPROC

! function p for redundancy resolution
FUNC robtarget p(robtarget t)

 ! from quaternion to ZYZ Euler angles
 n     := t.rot.q1;
 ex    := t.rot.q2;
 ey    := t.rot.q3;
 ez    := t.rot.q4;
 r13   := 2*(ex*ez+n*ey);
 r23   := 2*(ey*ez-n*ex);
 f_deg := Atan2( r23 , r13 );
 f_rad := f_deg*pi/180;
 s_deg := Atan2( Sqrt(Pow(r13,2)+Pow(r23,2)),
                 2*(Pow(n,2)+Pow(ez,2))-1 );
 s_rad := s_deg*pi/180;
 x     := t.trans.x/1000;
 y     := t.trans.y/1000;
 z     := t.trans.z/1000;
```

```
 ! computing regressors
 r2   := p2(x,y,z,f_deg,s_deg);
 r3   := p3(x,y,z,f_deg,s_deg);
 r5   := p5(x,y,z,f_deg,s_deg);
 r7   := p7(x,y,z,f_deg,s_deg);
 r228 := p228(x,y,z,f_deg,s_deg);
 r229 := p229(x,y,z,f_deg,s_deg);
 r234 := p234(x,y,z,f_deg,s_deg);
 r246 := p246(x,y,z,f_deg,s_deg);

 ! overriding third Euler angle
 t_rad := - 0.640266*r2 - 2.403878*r3 - 1.116066*r5
          + 4.466930*r7 + 0.463562*r228
          + 1.796788*r229 - 1.632775*r234
          + 0.287004*r246;

 ! modifying null-space
 t.rot := fromZYZtoQuat( f_deg,s_deg,-pi/180*t_rad );

 ! return optimal tool orientation
 RETURN t;

ENDFUNC
```

2.6 Summary

A complete parameterization of cyclic kinematic control strategy has been presented. A general framework to decouple the redundancy resolution technique from the implementation of a CLIK algorithm has been introduced and discussed. Thanks to this newly conceived methodology, the user, instead of the robot manufacturer, might directly select the redundancy resolution technique that best suites the application. On the other hand, from the manufacturer point of view, the CLIK algorithm can be implemented independently of the selected redundancy resolution algorithm. A case study where functional redundancy occurs demonstrates the effectiveness of this work.

CHAPTER 3

Experimental applications of the redundancy resolution framework

This Chapter presents some experimental validations of the approach discussed in the previous Chapter, which has been applied to common industrial situations where redundancy occurs. In particular, Section 3.1 is focused on spray painting, an application very similar to the one previously introduced as a case study. In Sections 3.2 and 3.3 the approach is exploited to tackle the problem of multiple degrees of redundancy during arc welding and coordinated manipulation, respectively. Finally, Section 3.4 discusses how the proposed architecture (Fig. 2.1) can be modified to take into account sensor-driven task adaptation, e.g. for force controlled tasks.

3.1 Optimal spray painting

Automated robotic spray painting is a well-established application, especially in automotive and furniture manufacturing. Many commercial software packages are available to optimize offline this task. In fact, the tool trajectory planning is a complex problem, involving several engineering techniques, ranging from non-linear programming to 3D surface modeling.
The quality of the paint coating highly depends on the geometric properties of the

surface and on the cost function adopted to compute the gun trajectory. Commercial optimization tools aim at planning the tool trajectory to accomplish the task with the minimum cycle-time or with the minimum number of trajectory turns, subject to the desired coating thickness, but rarely take into account the robot properties. The decision variables are the route taken by the gun on the surface, the standoff distance and the path velocity.
A simple model of the painting task that is usually taken into account for optimization is depicted in Fig. 3.1, see [7], [96], [118]. The typical profile of the paint deposition rate $f\,(r,h)$ is also shown, where R is spray cone radius and h is

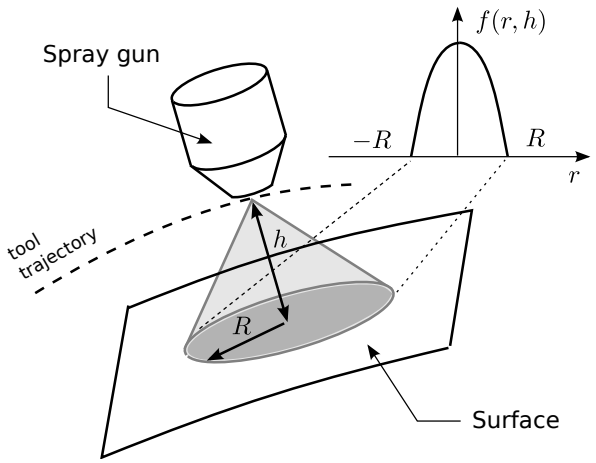

Figure 3.1: *Model of the painting task*

the TCP standoff distance. From this simple model, using the tools of differential geometry, see [96], it is possible to compute the deposition of paint on any point of the surface as a function of the gun trajectory.
Assuming that the shape of the painting distribution is a cone, the axial symmetry of the tool allows a degree of freedom (i.e. the rotation around the tool axis of symmetry) that does not affect the task execution and can be exploited to further optimize the painting task. As an output of a non model-based optimization technique, the description of the trajectory of the spray gun requires $m = 5$ DOF, one less than those of a 6-axes industrial robot ($n = 6$). Three DOF are used to place the tool in the Cartesian space, two DOF are necessary to make the spray gun perpendicular to the surface. Assume that the tool pose can be described in terms of Cartesian position of the TCP and a minimal description of the orientation of the tool, then the angle around the tool axis can be freely specified without affecting the task.
In order to describe the painting task from a kinematic point of view, let

$$\boldsymbol{\mu} = \begin{bmatrix} x & y & z & \rho & \theta \end{bmatrix}^T \quad \nu = \phi \tag{3.1}$$

be a minimal set of task variables (x, y, z are Cartesian coordinates of the TCP while ρ and θ are the first two ZYZ Euler angles) and the augmenting scalar variable (the third Euler angle ϕ), respectively.
Assuming that one would like to exploit the redundancy to optimize the manipulability measure, see [122], let $\boldsymbol{J}_{\boldsymbol{\omega}}$ be the robot Jacobian in the world frame and assume that, during the motion, the manipulability measure $u(\boldsymbol{q})$ has to be maximized, where

$$u = \sqrt{\det\left(\boldsymbol{J}_{\boldsymbol{\omega}} \boldsymbol{J}_{\boldsymbol{\omega}}{}^{T}\right)} \tag{3.2}$$

As already explained, the maximization of a cost function can be turned into the following holonomic constraint:

$$\sigma(\boldsymbol{q}) = \boldsymbol{N}^{T} \left(\frac{\partial u}{\partial \boldsymbol{q}}\right)^{T} = 0 \tag{3.3}$$

where $\boldsymbol{N}$ is any null-space basis of the task Jacobian $\boldsymbol{J}$.

We make now reference to a robotic painting station consisting in an ABB IRC 5 controller and a 6-axes ABB IRB 140 robot equipped with an ABB RB1000-WSC spray painting gun. For the given robotic station and the optimality requirement, a number of $M = 5000$ Monte Carlo samples consistent with the optimality constraint (3.3) have been extracted. Then, the function $p^0(\cdot)$ has been selected within a functional space composed of polynomials in Cartesian variables of the task and a modified truncated Fourier series in the orientation variables, yielding

$$\begin{aligned} p(\boldsymbol{\mu}) = {} & 0.99\cos(0.5\rho)\sin(\theta) + 0.50\cos(1.5\rho) - 0.63\left((x-0.4)/0.3 - 1\right) \\ & + 1.56\sin(\rho)\cos(0.5\theta) - 1.96\sin(\rho)\sin(\theta) + 1.42y \\ & - 0.40\left((z-0.2)/0.4 - 1\right) - 0.31\left((z-0.2)/0.4 - 1\right)^2 \end{aligned} \tag{3.4}$$

corresponding to an acceptance threshold of F_{TH}^0 of $6\,\mathrm{deg}$.
In the following the output of two experiments is discussed. In the former, the proposed redundancy resolution algorithm is implemented with the function $p^0(\cdot)$ selected according to (3.4). In the latter, $p^0(\cdot)$ was simply set to 0 yielding the constraint $\phi = 0$, which implies the tool to be aligned with the world's x-axis.
For both the simulations, the input of the inverse kinematic algorithm was an S-shaped trajectory laid on a curved smooth surface, resembling a car door. The path is covered from left to right in $6\ s$. We assume that the trajectory is given as the typical output of a non model-based optimization technique for spray painting, and thus cannot be further optimized, but still it allows one degree of freedom when covered with the tool mounted on the manipulator.

In Fig. 3.2 the time history of the manipulability measure is shown and compared to the maximum achievable one. As one can see using the redundancy resolution technique with the function $p^0(\cdot)$ in (3.4) the optimality of the manipulability measure is obtained, confirming the accuracy of the approximation that led to (3.4). On the other hand, the trajectory corresponding to $p^0(\cdot) = 0$ shows how smaller the manipulability measure can be compared to its maximum value, if the redundant degree of freedom is not accurately planned. For instance, at time $t = 4.5\ s$, corresponding to the second turn, the optimal manipulability index is 6 times greater than the index obtained with a non-optimal redundancy resolution. Since usually the programmed task velocity around turn is as higher as possible, a small manipulability index might cause very high joint velocities, as it actually happens at time $t = 4.5\ s$ (see Fig. 3.3).

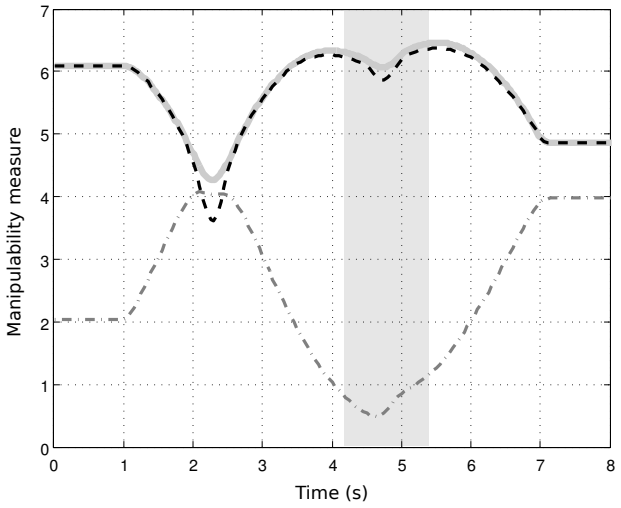

Figure 3.2: *Manipulability measure: extended Jacobian (simulated, solid gray), proposed method (experimental, dashed black) and trivial redundancy resolution (experimental, dot-dashed gray)*

Finally, Fig. 3.4 reports the time history of the third Euler angle ϕ during the optimal experiment, compared to the one obtained by simulating the extended Jacobian algorithm.

3.2 Arc welding with external workpiece positioner

Robotized arc welding is another well-established technique. For increased flexibility, the welding station is usually endowed with a common 6-axes robot and a workpiece positioner, an additional mechanical unit that enables the workpiece to rotate around one external axis, as shown in Fig. 3.5. The positioner is usually

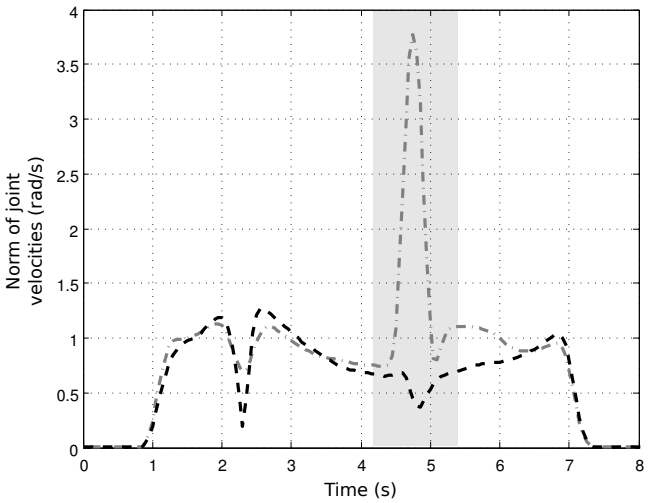

Figure 3.3: *Norm of joint velocities: proposed method (experimental, dashed black) and trivial redundancy resolution (experimental, dot-dashed gray)*

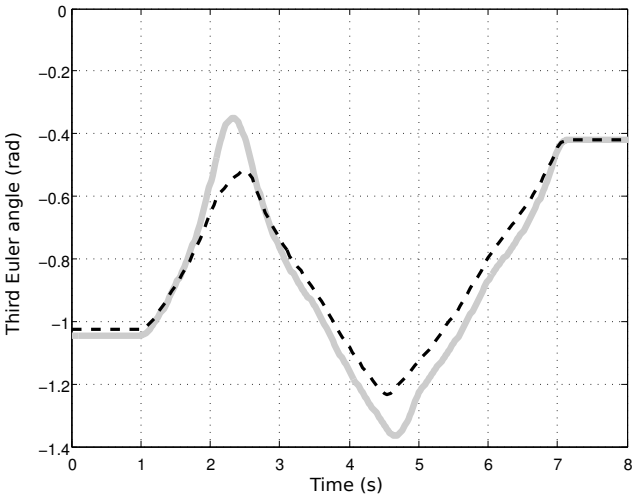

Figure 3.4: *Third Euler angle $\nu = \phi$: extended Jacobian (simulated, solid gray) and proposed method with (experimental, dashed black)*

more accurate than the one required for manual welding. Moreover, the positioner must be compatible with the robot control cabinet as it is usually actuated by the robot controller itself, in order to coordinate the motion of all the axes while welding. The total number of DOF simultaneously under control is then[1] $n = 7$. On the other hand, the welding torch possesses a cylindrical symmetry

[1]The position of the robot will be specified through joint variables $\boldsymbol{q_{1,\ldots,6}}$ while the position of the external axis will be referred to as q_7.

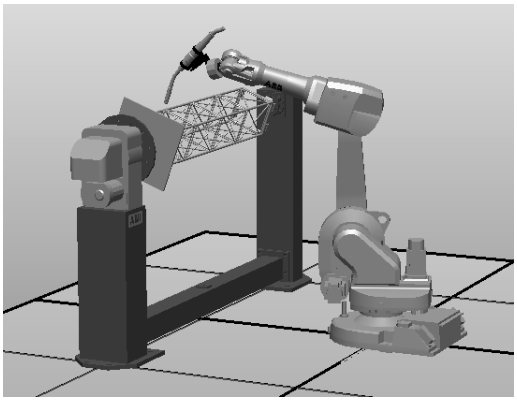

Figure 3.5: *Welding station with a workpiece positioner*

as in the case of the spray painting gun described in the previous Section. Since the task requires only $m = 5$ DOF, this application has $n - m = 2$ degrees of redundancy.
In order to describe the welding task, assume that a frame $\boldsymbol{T} \in SE(3)$ is attached to the robot TCP while another frame, say $\boldsymbol{W} \in SE(3)$, is attached to the (moving) workpiece. Then, define

$$\boldsymbol{\mu} = \begin{bmatrix} x_r & y_r & z_r & \rho_r & \theta_r \end{bmatrix}^T \quad \boldsymbol{\nu} = \begin{bmatrix} \phi_r & \psi \end{bmatrix}^T \tag{3.5}$$

as a minimal set of task variables (x_r, y_r, z_r are Cartesian coordinates describing the position of $\boldsymbol{T}$ with respect to $\boldsymbol{W}$, while ρ and θ are the first two ZYZ Euler angles describing their relative orientation) and the two augmenting variables (the third Euler angle ϕ and the external axis position ψ describing the additional degree of freedom introduced by the workpiece positioner), respectively.
Assuming that the user would like to maximize the manipulability measure u in (3.2), the following holonomic constraint

$$\boldsymbol{\sigma}(\boldsymbol{q}) = \boldsymbol{N}^T \left(\frac{\partial u}{\partial \boldsymbol{q}} \right)^T = \boldsymbol{0} \tag{3.6}$$

has been selected as a redundancy resolution criterion.
The analysis was performed on an ABB IRC 5 controller, a 6-axes ABB IRB 1600 robot equipped with an ABB PKI 300 torch and an ABB IRBP L workpiece positioner[2].
In this application, the motion of the robot is specified with respect to a moving frame. This requires the motion of the two mechanical units to be synchronized. This can be achieved with a proprietary additional software called MULTIMOVE

[2]The welding robot considered in this application is not available in the Laboratory. On the other hand, ABB provides a software named ROBOT STUDIO which emulates in detail the behavior and the interfaces of the IRC 5 controller.

which provides the synchronization between the robot controller and the external axis unit. The block diagram in Fig. 3.6 sketches the implementation on top of the industrial controller.

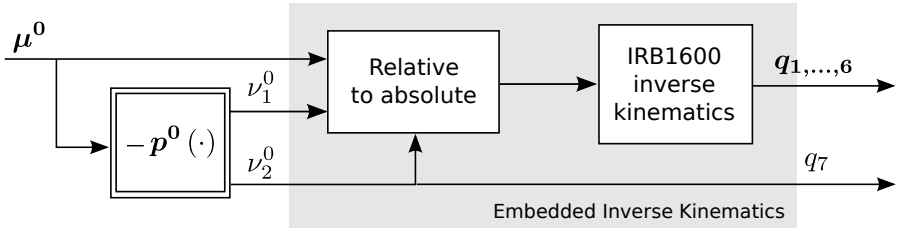

Figure 3.6: *Block diagram of the proposed framework as applied to an arc welding task with an external workpiece positioner*

So far, the proposed architecture for kinematic inversion has been applied to the case of a single degree of redundancy. However, there is no limitation on the number of degrees of redundancy this methodology is able to tackle. The case of multiple degrees of redundancy, and in particular the design of the function $\boldsymbol{p^0}(\cdot)$, is clearly more involved. In fact, in this case, such a function is no longer scalar and the approximation algorithm has to be iterated over the number of degrees of redundancy.
As pointed out in the previous Chapter, the computation of the function $\boldsymbol{p^0}(\cdot)$ is performed using a greedy algorithm in order to achieve a compromise between the approximation accuracy and the number of regressors to be evaluated online in the robotic controller. As for the case of multiple degrees of redundancy, this argument is still consistent. However, the simultaneous approximation of several functions can be tackled in different ways.
First of all, we assume, without any lack of generality, to use a unique pool of regressors. Then, two options can be considered:

- considering each of the $n - m > 1$ components of the function separately;
- processing the $n - m$ approximation simultaneously.

The adoption of the first choice leads to specify the accuracy of the approximation as follows:

$$\|\delta p_1(\cdot)\| \leq F_{TH,1}^0 \quad \cdots \quad \|\delta p_{n-m}(\cdot)\| \leq F_{TH,n-m}^0 \tag{3.7}$$

where $F_{TH,1}^0, \cdots, F_{TH,n-m}^0$ are design parameters assigned according to the dimensions of the corresponding component of the function $\boldsymbol{p}(\cdot)$. On the other hand, when the second option is considered, the overall approximation error $\boldsymbol{\delta p}(\cdot)$ is a vector function and its components might be heterogeneous (e.g. angles and distances). For this reason, appropriate weighting factors $w_1^2, \cdots, w_{n-m}^2$

should be adopted when defining the approximation accuracy

$$\|\boldsymbol{\delta p}(\cdot)\|_{\boldsymbol{W}}^2 = w_1^2 \|\delta p_1(\cdot)\|^2 + \cdots + w_{n-m}^2 \|\delta p_{n-m}(\cdot)\|^2 \leq 1 \tag{3.8}$$

It should be clear, now, that treating the approximation of each component separately is to some extent equivalent to the case of simultaneous approximation of all the components, provided that weights w_i have been selected consistently with $F_{TH,i}^0$, $i = 1, \cdots, n-m$. In fact

$$\forall i = 1, \cdots, n-m : \|\delta p_i(\cdot)\| \leq F_{TH,i}^0 = \frac{w_i^{-1}}{n-m} \Rightarrow \|\boldsymbol{\delta p}(\cdot)\|_{\boldsymbol{W}} \leq 1 \tag{3.9}$$

Therefore, without any lack of generality, the first option, consisting in processing, possibly in parallel, each degree of redundancy separately will be adopted in this work. Actually, this solution has in turn two options:

- to force reuse of regressors selected in the previous iteration;
- to ignore regressors selected in the previous iteration.

The former solution tries to further minimize the number of regressors to be used. The latter, instead, does not consider the previous iteration of the greedy algorithm. The second approach will be adopted herein and therefore the approximation algorithm will run as many times as the number of degrees of redundancy, without taking care of the previously selected regressors.

A number of $M = 1000$ Monte Carlo samples consistent with the optimality constraint (3.6) have been extracted.
Then, the function $\boldsymbol{p^0}(\cdot)$ has been selected within a functional space composed of polynomials and inverse trigonometric function of the task Cartesian variables and a modified truncated Fourier series in the orientation variables, yielding

$$\boldsymbol{p^0}(\boldsymbol{\mu}) = \begin{bmatrix} p_{\nu_1}^0(\boldsymbol{\mu}) & p_{\nu_2}^0(\boldsymbol{\mu}) \end{bmatrix}^T \tag{3.10}$$

where

$$\begin{aligned} p_{\nu_1}^0(\boldsymbol{\mu}) &= -0.26 z_r/0.6 + 0.21 y_r/0.2 + 0.82 y_r/0.2 \left(z_r/0.6\right)^3 \\ &\quad + 0.38\sqrt{y_r^2 + z_r^2} - 3.04 \sin(3\theta_r) \\ p_{\nu_2}^0(\boldsymbol{\mu}) &= -1.03\sqrt{x_r^2 + y_r^2 + z_r^2} - 0.36 z_r/0.6 - 0.31 \mathrm{atan2}(x_r, y_r) \\ &\quad - 0.22 \mathrm{atan2}\left(y_r, \sqrt{x_r^2 + y_r^2}\right) \end{aligned} \tag{3.11}$$

corresponding to an acceptance threshold of $F_{TH}^0 = 4\,\mathrm{deg}$ for both the components of $\boldsymbol{p^0}(\cdot)$.

Two experiments have been performed. In the former, the proposed redundancy resolution algorithm is implemented with the function $\boldsymbol{p}^{\mathbf{0}}(\cdot)$ selected according to (3.11). In the latter, the controller is fed with a superimposed trajectory for both the two components of $\boldsymbol{\nu}$. Notice that in this case, the reference value of $\boldsymbol{\nu}$ is no longer a function of the task variables $\boldsymbol{\mu}$.
In Fig. 3.7 the time history of the manipulability measure is shown and compared to the maximum achievable one computed in simulation using the extended Jacobian algorithm. As one can see, using the redundancy resolution technique with the function $\boldsymbol{p}^{\mathbf{0}}(\cdot)$ in (3.11) the optimality of the manipulability measure is obtained. Figure 3.8 compares the two components of $\boldsymbol{\nu}$ computed using the function $\boldsymbol{p}^{\mathbf{0}}(\cdot)$ in (3.11) and with the extended Jacobian. As expected, the approximation error is small as guaranteed by Proposition 2.3 of Chapter 2.

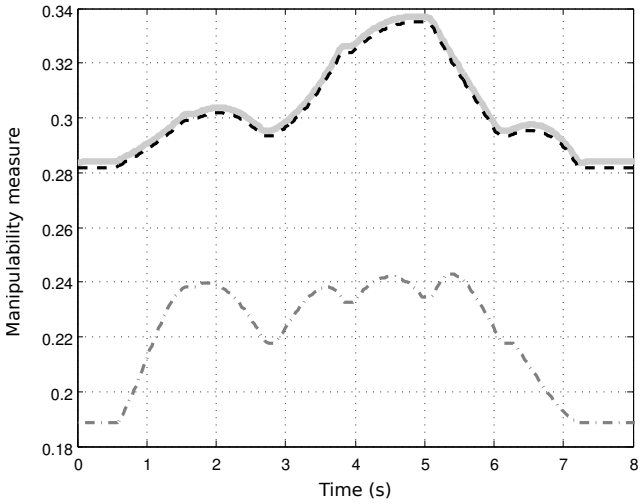

Figure 3.7: *Manipulability index: extended Jacobian (simulated, solid gray), proposed method (emulated, dashed black) and trivial redundancy resolution (emulated, dot-dashed gray)*

3.3 Coordinated movements of multiple robots

We now consider a multi-robot system composed of two 6-DOF-each industrial robots cooperating to perform a given manipulation task, as shown in Fig. 3.15. Cooperative manipulators [22] were introduced to overcome some drawbacks of common single robotic systems. It is widely agreed that operations such as carrying large payloads or assembly of compliant objects become feasible when two or more robots are coordinated. Multi-robot systems, in fact, possess extra DOF which naturally increase the dexterity of the system. On the other hand, robot cooperation opens the way to a series of challenges, ranging from interaction

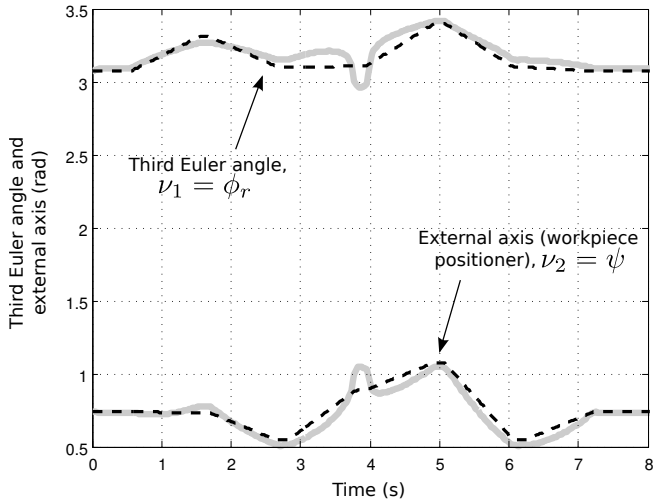

Figure 3.8: *Third Euler angle ν_1 and workpiece position ν_2: extended Jacobian (simulated, solid gray), proposed method (emulated, dashed black)*

control to redundancy resolution.
Pioneer works proposed control schemes for dual-arm systems based on exact feedback linearization, see e.g. [5], [109]. A couple of years later, first studies on the manipulability measure were published. For example, in [74] the manipulability of the system is defined in terms of intersections of the manipulability ellipsoids of each individual arm.
In [108] the so-called *leader-follower* task specification was introduced. Moreover, the problem of resolving the kinematic redundancy was considered explicitly and redundancy was referred to as one of the major benefits of multi-armed systems. The use of kinematic redundancy to achieve secondary objectives has been proposed in [49] to keep internal forces at a desired level during the manipulation and to properly distribute the control effort over each manipulator.
In [29] a complete task specification suitable for a dual-arm system has been introduced. In particular, an "intermediate frame" has been defined to be used together with the relative position/orientation of the two end-effectors, already introduced in the leader-follower approach. The work described in [21] addresses the geometric consistency of the impedance-control applied to dual-arm robotic systems, while in [20] the use of quaternion for task description is introduced to overcome the well-known problem of representation singularities.

The joint space description of the system can be simply extended from the case of a single robot by stacking the two vectors containing the joint angles of each robot, i.e.

$$\boldsymbol{q} = \begin{bmatrix} q_1 & \dots & q_{12} \end{bmatrix}^T \tag{3.12}$$

As for the task description, in the leader-follower approach $\boldsymbol{W} \in SE(3)$ contains the position and orientation of leader and similarly $\boldsymbol{T} \in SE(3)$ for the follower. The coordinated task can be described in terms of relative displacement and orientation of the follower with respect to the leader. To this end, define $\boldsymbol{R} = \boldsymbol{W}^{-1}\boldsymbol{T}$ the $SE(3)$ matrix describing the orientation of the follower with respect to the leader and the corresponding displacement, see Fig. 3.9. This sce-

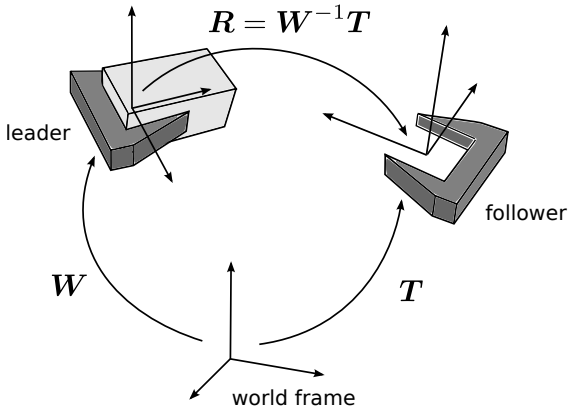

Figure 3.9: *Multi-robot kinematics chains*

nario, however, is not sufficient to fully constrain the pose of the two robots, but only the relative displacement of the two end-effectors. In order to achieve a full kinematic description of the system, some additional variables can be introduced. One possible solution is to represent the absolute position and orientation of the leader, too.
Regarding the differential kinematics of the task, the relative twist $\boldsymbol{v_r}$ of the follower with respect to the leader is given by

$$\boldsymbol{v_r} = \boldsymbol{J_r}\dot{\boldsymbol{q}} \tag{3.13}$$

where $\boldsymbol{J_r}$ is the relative task Jacobian, see Appendix C.
Finally, consider

$$\boldsymbol{\mu} = \begin{bmatrix} x_r & y_r & z_r & \rho_r & \theta_r & \phi_r \end{bmatrix}^T \quad \boldsymbol{\nu} = \begin{bmatrix} x_l & y_l & z_l & \rho_l & \theta_l & \phi_l \end{bmatrix}^T \tag{3.14}$$

as the inputs of a robotic controller, where x_r, y_r and z_r are the Cartesian position of the follower with respect to the leader and ρ_r, θ_r and ϕ_r represent the corresponding orientation (Euler angles), while $\boldsymbol{\nu}$ contains the absolute position of the leader (x_l, y_l and z_l are the Cartesian coordinates of the TCP, while ρ_l, θ_l and ϕ_l are a minimal description of the orientation in terms of Euler angles).
If the relative displacement and orientation of the follower with respect to the leader (i.e. the task variables $\boldsymbol{\mu}$) should be considered only, which naturally happens during coordinated motions, the system is kinematically redundant. In fact,

the absolute position of the leader $\boldsymbol{\nu}$ can be freely assigned, without affecting the task execution.
Assume one would like to reduce the motor torque effort to perform the task and consider the dynamic equation of the system in terms of rigid bodies:

$$\boldsymbol{B}(\boldsymbol{q})\,\ddot{\boldsymbol{q}} + \boldsymbol{C}(\boldsymbol{q},\dot{\boldsymbol{q}})\,\dot{\boldsymbol{q}} + \boldsymbol{g}(\boldsymbol{q}) = \boldsymbol{\tau} \tag{3.15}$$

where $\boldsymbol{B}(\boldsymbol{q})$ is the block diagonal inertia matrix, $\boldsymbol{C}(\boldsymbol{q},\dot{\boldsymbol{q}})$ is the block diagonal matrix of centrifugal/Coriolis terms, $\boldsymbol{g}(\boldsymbol{q})$ is the vector containing the gravitational torques and $\boldsymbol{\tau}$ is the vector of applied torques.
Given the differential kinematics relations in (3.13), and taking its time derivative, one obtains

$$\dot{\boldsymbol{v}}_{\boldsymbol{r}} = \boldsymbol{J}_{\boldsymbol{r}}\ddot{\boldsymbol{q}} + \dot{\boldsymbol{J}}_{\boldsymbol{r}}\dot{\boldsymbol{q}} \tag{3.16}$$

In order to consider inertial terms only, the following approximations can be taken into account:

$$\dot{\boldsymbol{v}}_{\boldsymbol{r}} \approx \boldsymbol{J}_{\boldsymbol{r}}\ddot{\boldsymbol{q}} \quad \ddot{\boldsymbol{q}} \approx \boldsymbol{B}^{-1}\boldsymbol{\tau} \tag{3.17}$$

yielding

$$\dot{\boldsymbol{v}}_{\boldsymbol{r}} \approx \boldsymbol{J}_{\boldsymbol{r}}\boldsymbol{B}^{-1}\boldsymbol{\tau} = \boldsymbol{J}_{\boldsymbol{r}}\boldsymbol{B}^{-1}\boldsymbol{\Sigma}^{T}\boldsymbol{\tau}_{\boldsymbol{m}} \tag{3.18}$$

where $\boldsymbol{\Sigma}$ is the matrix containing the motor gear ratios such that the motor torque $\boldsymbol{\tau}_{\boldsymbol{m}}$ is $\boldsymbol{\tau}_{\boldsymbol{m}} = \boldsymbol{\Sigma}^{-T}\boldsymbol{\tau}$.
Equation (3.18) represents the relationship between applied torques and corresponding task accelerations when inertial effects are considered only. For this reason, one might want to maximize the following quantity

$$u = \sqrt{\det\left(\boldsymbol{J}_{\boldsymbol{r}}\boldsymbol{B}^{-1}\boldsymbol{\Sigma}^{T}\boldsymbol{\Sigma}\boldsymbol{B}^{-1}{\boldsymbol{J}_{\boldsymbol{r}}}^{T}\right)} \tag{3.19}$$

which is known as *dynamic manipulability measure*, see [121].

3.3.1 Model identification experiments

Since the cost function introduced to solve the kinematic redundancy depends on the dynamic equation of the system, a first experiment has been performed to identify the dynamical model in (3.15) of an ABB IRB 140 6-axes industrial manipulator. The linear relation between dynamical parameters $\boldsymbol{\Pi}$ and the required motor torque $\boldsymbol{\tau}_{\boldsymbol{m}}$ along a given trajectory $\boldsymbol{q}_{\mathbf{1},\ldots,\mathbf{6}}, \dot{\boldsymbol{q}}_{\mathbf{1},\ldots,\mathbf{6}}, \ddot{\boldsymbol{q}}_{\mathbf{1},\ldots,\mathbf{6}}$, i.e.

$$\boldsymbol{A}\left(\boldsymbol{q}_{\mathbf{1},\ldots,\mathbf{6}}, \dot{\boldsymbol{q}}_{\mathbf{1},\ldots,\mathbf{6}}, \ddot{\boldsymbol{q}}_{\mathbf{1},\ldots,\mathbf{6}}\right)\boldsymbol{\Pi} = \boldsymbol{\tau}_{\boldsymbol{m}} \tag{3.20}$$

is well-known, [8]. However, when the physical parameters are taken into account in (3.20), the regressor matrix $\boldsymbol{A}$ is usually rank-deficient. It follows that the

minimization problem

$$\mathbf{\Pi^0} = \arg\min_{\mathbf{\Pi}} \|\boldsymbol{A}\mathbf{\Pi} - \boldsymbol{\tau_m}\| \tag{3.21}$$

has infinite solutions and, among them, even those which are not physically consistent (e.g. having negative values of masses or inertias).

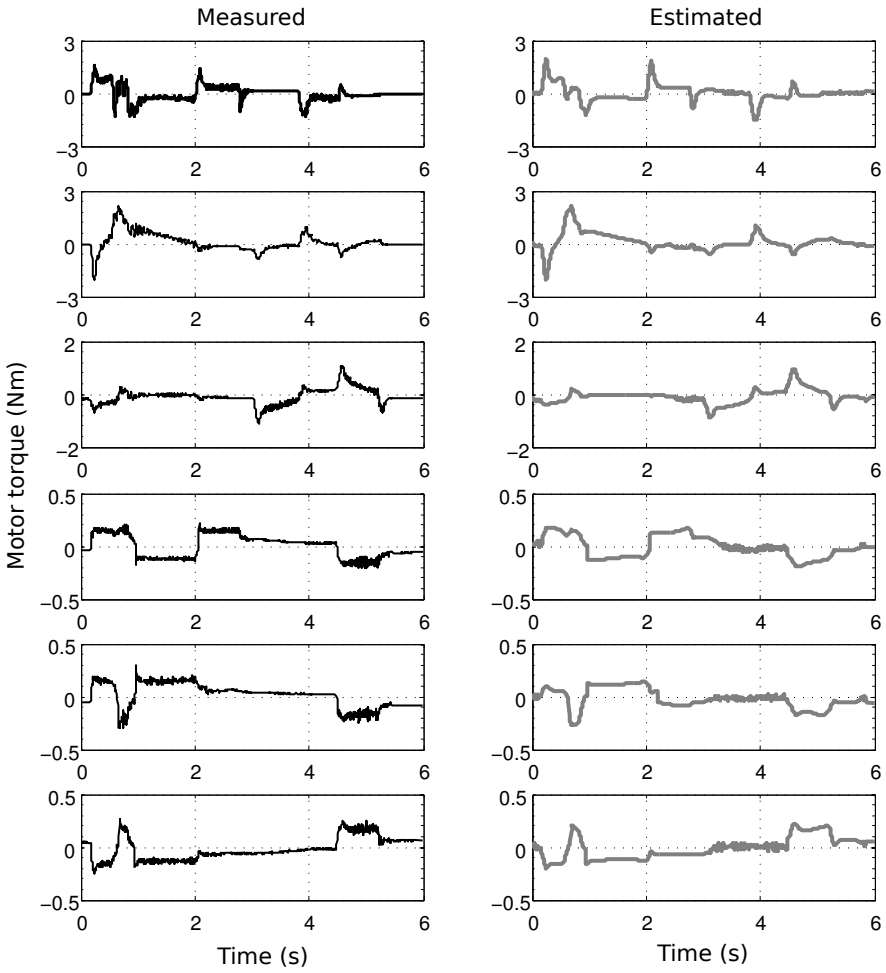

Figure 3.10: *Validation experiment: acquired motor torques (left column, black) vs. model-based predicted motor torques (right column, gray) corresponding to axis 1 (top) through axis 6 (bottom)*

As explained in [9], if a tentative value of the physical parameters, say $\mathbf{\Pi^{ref}}$, is available, one can select the solution of (3.21) such that $\left\|\mathbf{\Pi^0} - \mathbf{\Pi^{ref}}\right\|$ is minimized, too.

Therefore, let

$$\boldsymbol{A} = \begin{bmatrix} \boldsymbol{U_1} & \boldsymbol{U_2} \end{bmatrix} \begin{bmatrix} \boldsymbol{\Sigma_{11}} & \boldsymbol{0} \\ \boldsymbol{0} & \boldsymbol{0} \end{bmatrix} \begin{bmatrix} \boldsymbol{V_1}^T \\ \boldsymbol{V_2}^T \end{bmatrix} \tag{3.22}$$

be the SVD of the rank-deficient regressor matrix $\boldsymbol{A}$. Then the following solution

$$\boldsymbol{\Pi^0} = \boldsymbol{V_1} {\boldsymbol{\Sigma_{11}}}^{-1} {\boldsymbol{U_1}}^T \left(\boldsymbol{\tau_m} - \boldsymbol{A\Pi^{ref}} \right) + \boldsymbol{\Pi^{ref}} \tag{3.23}$$

is optimal in the sense of (3.21) and also minimizes the distance $\left\| \boldsymbol{\Pi^0} - \boldsymbol{\Pi^{ref}} \right\|$ from the reference value $\boldsymbol{\Pi^{ref}}$.

The output data of a first experiment (motor torques, joint positions, velocities and accelerations) have been used to identify the set of physical parameters $\boldsymbol{\Pi^0}$ using (3.23).
A second experiment has been performed to compare the identified model and the actual dynamic behavior of the robot. Time histories of acquired and predicted motor torques during the validation experiment are shown in Fig. 3.10. As one can see, the model is accurate in replicating the behavior of the robot. Notice that the model correctly predicts the low-frequency behavior, but it is not able to predict the high frequency oscillations, probably due to some intrinsic joint flexibility, see e.g. [33], [40].

3.3.2 Redundancy resolution and manipulation experiments

The identified model, and in particular the block diagonal inertia matrix $\boldsymbol{B}(\boldsymbol{q})$, has been used to tune the redundancy resolution criterion. Letting

$$u = \sqrt{\det \left(\boldsymbol{J_r} \boldsymbol{B}^{-1} \boldsymbol{\Sigma}^T \boldsymbol{\Sigma} \boldsymbol{B}^{-1} {\boldsymbol{J_r}}^T \right)} \tag{3.24}$$

the cost function to be maximized and applying the extended Jacobian method, one may turn the optimization requirement to the following holonomic constraint

$$\boldsymbol{\sigma}(\boldsymbol{q}) = \boldsymbol{N}^T \left(\frac{\partial u}{\partial \boldsymbol{q}} \right)^T = \boldsymbol{0} \tag{3.25}$$

Therefore a number of $M = 5000$ Monte Carlo samples have been generated consistent with the holonomic constraint (3.25). These samples were then used to tune the redundancy resolution criterion embedded in the function

$$\boldsymbol{p^0}(\boldsymbol{\mu}) = \begin{bmatrix} p^0_{\nu_1}(\boldsymbol{\mu}) & \dots & p^0_{\nu_6}(\boldsymbol{\mu}) \end{bmatrix}^T \tag{3.26}$$

which has been selected within a functional space composed of polynomial and inverse trigonometric functions of the Cartesian task variables, a modified truncated Fourier series and linear functions in the orientation variables. The result

is:

$$
\begin{aligned}
p^0_{\nu_1}(\boldsymbol{\mu}) &= 0.63\sqrt{x_r^2+z_r^2} + 0.04\text{atan2}(y_r, z_r) - 0.68 \\
p^0_{\nu_2}(\boldsymbol{\mu}) &= 0.06\text{atan2}(x_r, z_r) + 0.03\text{atan2}(y_r, z_r) \\
p^0_{\nu_3}(\boldsymbol{\mu}) &= 0.05\text{atan2}(x_r, y_r) - 0.18\cos(0.5\rho) + 0.06\sin(\theta) \\
p^0_{\nu_4}(\boldsymbol{\mu}) &= 0.39\text{atan2}(x_r, z_r) + 0.51\text{atan2}\left(x_r, \sqrt{x_r^2+z_r^2}\right) \\
&\quad - 0.09\text{atan2}\left(y_r, \sqrt{x_r^2+y_r^2+z_r^2}\right) - 0.30\cos(1.5\rho_r)\cos(0.5\theta_r) \\
&\quad + 0.01\left(x_r - 0.1)/0.15\right)^4 (z_r - 0.15)/0.15 \\
&\quad - 0.07\cos(0.5\rho_r)\sin(2\theta_r) + 0.14\sin(\rho_r)\cos(1.5\theta_r) \\
p^0_{\nu_5}(\boldsymbol{\mu}) &= -0.10\text{atan2}(x_r, y_r) - 0.36\text{atan2}\left(y_r, \sqrt{x_r^2+y_r^2+z_r^2}\right) \\
&\quad - 1.21 + 0.06\left(y_r/0.15\right)^2 - 0.07\left(y_r/0.15\right)^3 - 0.37\sin(\rho_r) \\
&\quad - 0.24\cos(0.5\rho_r)\cos(0.5\theta_r) - 0.03\left(\left(x_r - 0.1\right)/0.15\right)^2 \\
p^0_{\nu_6}(\boldsymbol{\mu}) &= -0.28\text{atan2}(y_r, z_r) - 0.48\text{atan2}\left(z_r, \sqrt{x_r^2+y_r^2+z_r^2}\right) \\
&\quad - 1.65\cos(0.5\rho_r) + 0.56\cos(1.5\rho_r)\cos(0.5\theta_r) + 0.81\rho_r
\end{aligned}
\tag{3.27}
$$

corresponding to an acceptance threshold F^0_{TH} of $2\ mm$ for the Cartesian variables, $3\,\text{deg}$ for the first two Euler angles and $6\,\text{deg}$ for the last one.

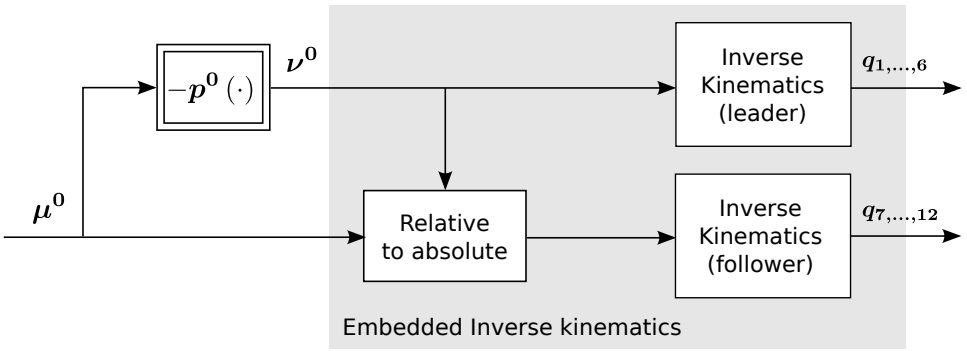

Figure 3.11: *Block diagram of the proposed framework as applied to a multiple-robot system*

The block diagram in Fig. 3.6 sketches the implementation on top of the industrial controller using the additional feature MULTIMOVE for synchronization. An excerpt of the actual implementation in the RAPID language is given in the following.

```
! Leader
PROC taskROB1()
   SyncMoveOn sync1, motion_tasks;
   MoveJ p(ps1)\ID:=10, v2000\T:=0.5, fine, tool0;
   MoveL p(ps2)\ID:=20, v2000\T:=0.5, fine, tool0;
   MoveJ p(ps3)\ID:=30, v2000\T:=0.5, fine, tool0;
   MoveL p(ps4)\ID:=40, v2000\T:=0.5, fine, tool0;
   MoveL p(ps5)\ID:=50, v2000\T:=0.5, fine, tool0;
   MoveL p(ps2)\ID:=60, v2000\T:=0.5, fine, tool0;
   MoveL p(ps6)\ID:=70, v2000\T:=0.5, fine, tool0;
   MoveL p(ps7)\ID:=80, v2000\T:=0.5, fine, tool0;
   MoveL p(ps1)\ID:=90, v2000\T:=0.5, fine, tool0;
   SyncMoveOff sync2;
UNDO
   SyncMoveUndo;
ENDPROC

! Follower
PROC taskROB2()
  SyncMoveOn sync1, motion_tasks;
  MoveJ ps1\ID:=10, v2000\T:=0.5, fine,
     tool0 \Wobj:=leader;
  MoveL ps2\ID:=20, v2000\T:=0.5, fine,
     tool0 \Wobj:=leader;
  MoveL ps3\ID:=30, v2000\T:=0.5, fine,
     tool0 \Wobj:=leader;
  MoveL ps4\ID:=40, v2000\T:=0.5, fine,
     tool0 \Wobj:=leader;
  MoveL ps5\ID:=50, v2000\T:=0.5, fine,
     tool0 \Wobj:=leader;
  MoveL ps2\ID:=60, v2000\T:=0.5, fine,
     tool0 \Wobj:=leader;
  MoveL ps6\ID:=70, v2000\T:=0.5, fine,
     tool0 \Wobj:=leader;
  MoveL ps7\ID:=80, v2000\T:=0.5, fine,
     tool0 \Wobj:=leader;
  MoveL ps1\ID:=90, v2000\T:=0.5, fine,
     tool0 \Wobj:=leader;
  SyncMoveOff sync2;
```

```
UNDO
  SyncMoveUndo;
ENDPROC
```

Notice that, while the position of the follower $\boldsymbol{\mu}$ is specified with respect the the absolute motion of the leader using the keyword `\Wobj:=Leader`, the motion of the leader $\boldsymbol{\nu}$ is computed as the output of a function, `p( )`, that implements function $-\boldsymbol{p^0}(\cdot)$ in (3.27).

The Laboratory where the experiments have been carried out is equipped with just one 6-axes ABB IRB 140 manipulator. On the other hand, ABB provides a software named ROBOT STUDIO which emulates in detail the behavior and the interfaces of the IRC 5 controller allowing also the user to save the output of the inverse kinematics (i.e. $\boldsymbol{q_1}$,... ,$\boldsymbol{_6}$ and $\boldsymbol{q_7}$,... ,$\boldsymbol{_{12}}$ of Fig. 3.11).
Two experiments have been performed. In the former, the proposed redundancy resolution algorithm is implemented with the function $\boldsymbol{p^0}(\cdot)$ selected according to (3.27). In the latter, the controller is fed with a superimposed trajectory for the leader. In this situation, the kinematic control strategy is no longer cyclic, being the reference value of $\boldsymbol{\nu}$ a generic function of time.
In Fig. 3.12 the time history of the dynamic manipulability measure is shown and compared to the maximum achievable one computed in simulation using the extended Jacobian algorithm. As one can see, thanks the redundancy resolution technique, with the function $\boldsymbol{p^0}(\cdot)$ in (3.27) it was possible to optimize the dynamic manipulability measure even without having access to the embedded code of the controller. A comparison of the six components of $\boldsymbol{\nu}$ computed using the function $\boldsymbol{p^0}(\cdot)$ in (3.27) and the extended Jacobian is reported in Figs. 3.13 and 3.14.

A visual comparison of the two redundancy resolution strategies is shown in Fig. 3.16. Notice that using the proposed redundancy resolution criterion, which was designed in order to reduce the inertial effects, the two robots are closer to each other, therefore with a smaller total inertia, with respect to the trivial redundancy resolution in which the swept motion has an increased volume.

Finally, Fig. 3.17 shows the time history of the norm of the acquired motor torques $\sqrt{\boldsymbol{\tau_m}^T \boldsymbol{\tau_m}}$ during the two experiments. As one can see the optimality of the cost function in (3.24) is achieved and the proposed framework clearly contributes in removing several peaks, making the redundancy resolution more energetically effective.

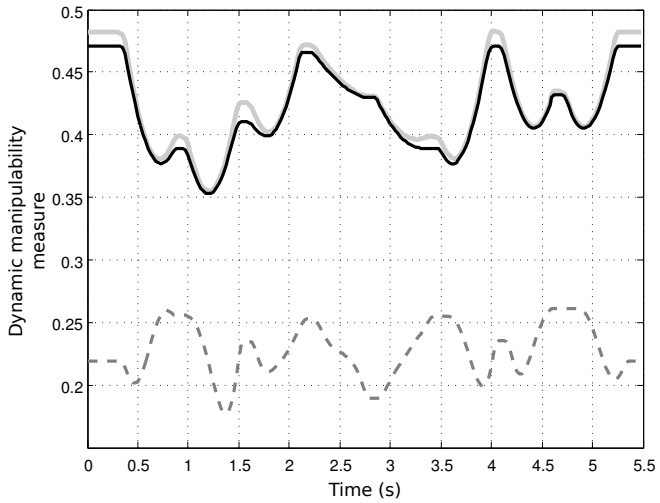

Figure 3.12: *Dynamic manipulability measure: extended Jacobian (simulated, solid gray), proposed method (emulated, dashed black) and trivial redundancy resolution (emulated, dot-dashed gray)*

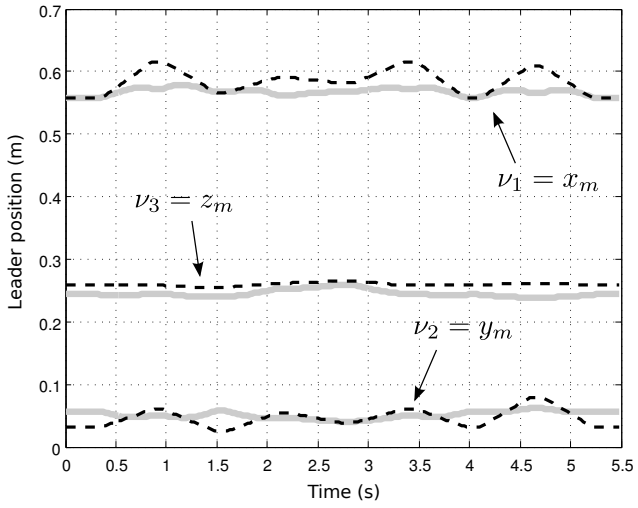

Figure 3.13: *Cartesian position of the leader $\boldsymbol{\nu_{1,2,3}}$: extended Jacobian (simulated, solid gray) and proposed method (emulated, dashed black)*

3.4 Torque-effective robotic drilling

Thanks to their flexibility, automated drilling tasks can be performed with common industrial robots. They provide high accuracy and repeatability with relatively reduced costs [89] with respect to hard automation solutions. However, achieving highly accurate drilling operations using standard robotic manipulators

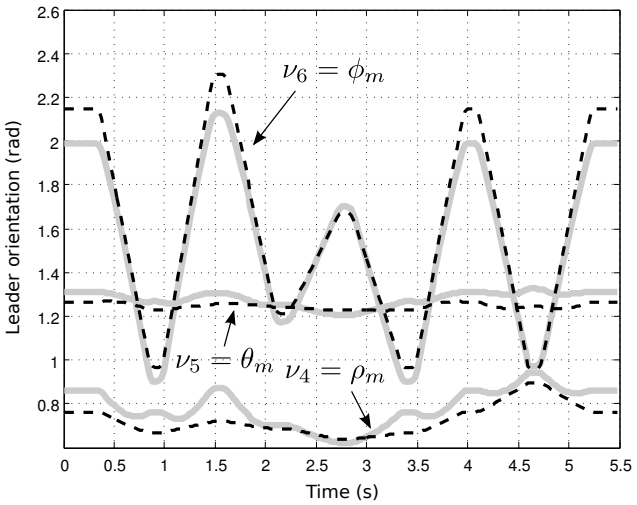

Figure 3.14: *Orientation of the leader $\boldsymbol{\nu_{4,5,6}}$: extended Jacobian (simulated, solid gray) and proposed method (emulated, dashed black)*

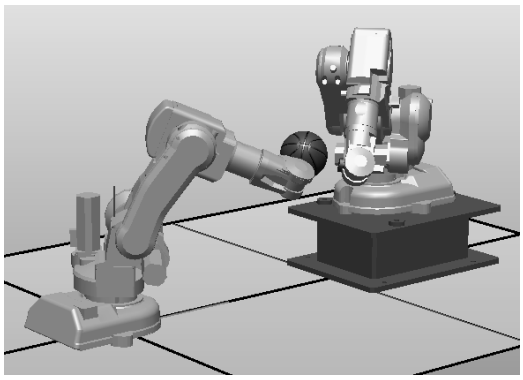

Figure 3.15: *Two coordinated robot performing a manipulation task*

might be quite difficult. Many issues related to a drilling task have been already addressed in the literature. For instance, some results on force control for special drilling machines have been reported in [59]. A characterization of force controlled robotic drilling can be found in [6]. In [90] a force control scheme is proposed to actively compensate the drill sliding. Beside force control issues, the challenging aspect of robotic drilling, which is mainly a pure kinematic issue, is redundancy resolution. In fact, similar to the spray painting example in Section 3.1, a drilling operation requires $m = 5$ DOF: three DOF are used to place the tip in the Cartesian space, two DOF are necessary to make the drill perpendicular to the workpiece. It follows that a 6-axes industrial robot is redundant with respect to a drilling task. Assume that the tool pose can be described in terms of Carte-

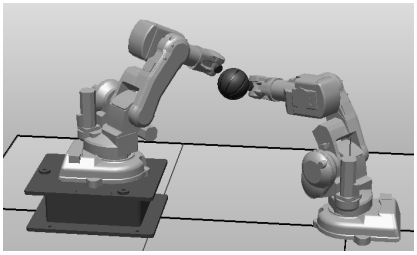

(a) Trivial redundancy resolution, $t = 0.5\ s$

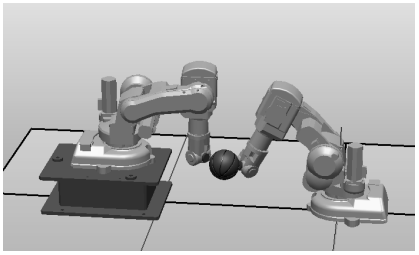

(b) Optimal redundancy resolution, $t = 0.5\ s$

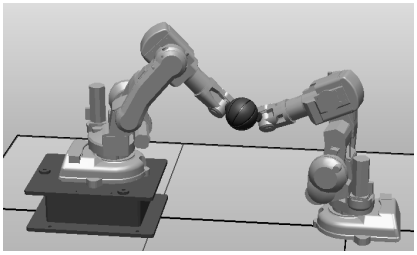

(c) Trivial redundancy resolution, $t = 2.0\ s$

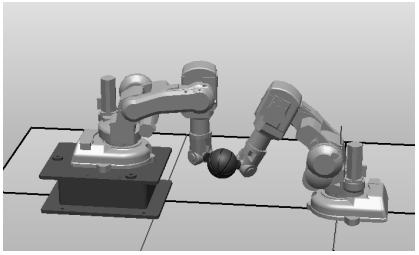

(d) Optimal redundancy resolution, $t = 2.0\ s$

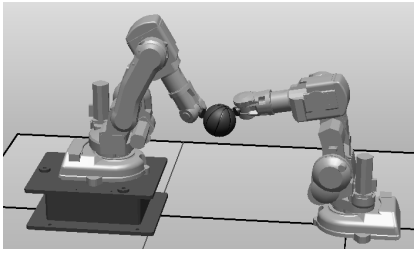

(e) Trivial redundancy resolution, $t = 3.5\ s$

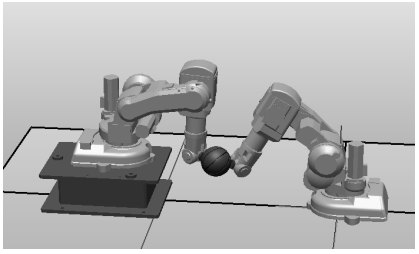

(f) Optimal redundancy resolution, $t = 3.5\ s$

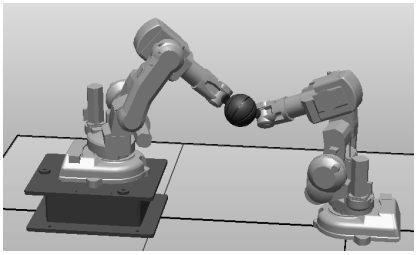

(g) Trivial redundancy resolution, $t = 5.0\ s$

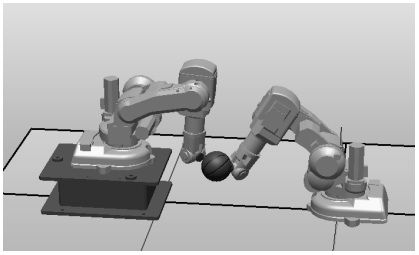

(h) Optimal redundancy resolution, $t = 5.0\ s$

Figure 3.16: *Two coordinated robot during a manipulation task with two different redundancy resolution criteria*

sian position of the TCP and a minimal description of the orientation of the tool, then the angle around the drill axis, see Fig. 3.18, can be freely specified without affecting the execution of the task. In order to describe the drilling operation, let

$$\boldsymbol{\mu} = \begin{bmatrix} x & y & z & \rho & \theta \end{bmatrix}^T \quad \nu = \phi \tag{3.28}$$

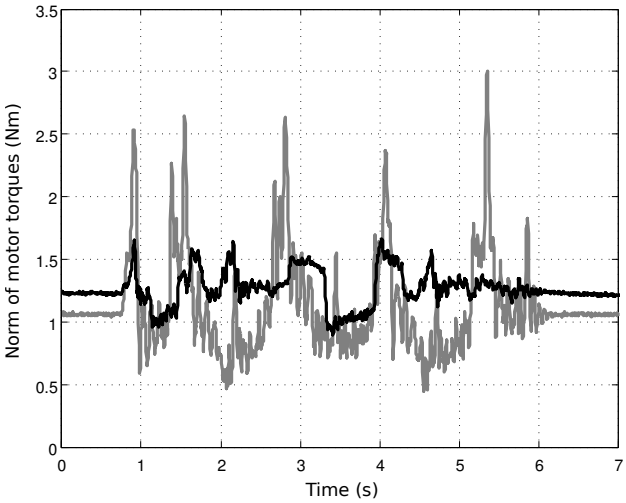

Figure 3.17: *Norm of motor torques: proposed method (experimental, solid black) and trivial redundancy resolution (experimental, solid gray)*

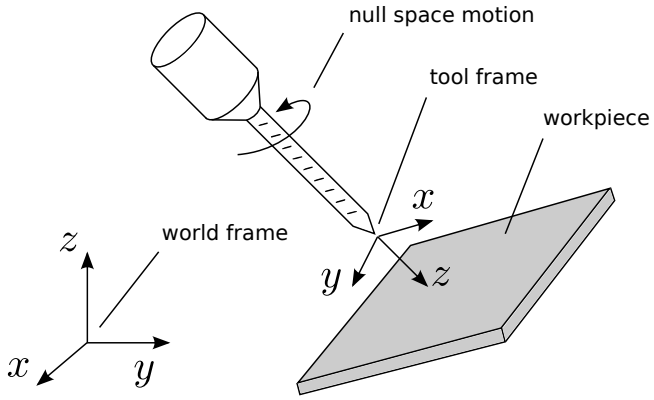

Figure 3.18: *Task redundancy during drilling operations: the task can be accomplished with different orientations of the tool around the drill axis*

be a minimal set of task variables (e.g. Cartesian coordinates of the TCP, x, y, z and the first two ZYZ Euler angles, ρ, θ) and the augmenting scalar variable (the third Euler angle ϕ), respectively.
Let $\boldsymbol{J}_{\boldsymbol{\omega}}^{\boldsymbol{tcp}}$ be the robot Jacobian in the TCP frame, then the relationship between a thrust force $\boldsymbol{n_z} f_z$ and the corresponding torque effort $\boldsymbol{\tau}$ is:

$$\boldsymbol{\tau} = \boldsymbol{J}_{\boldsymbol{\omega}}^{\boldsymbol{tcp}^T} \boldsymbol{n_z} f_z \quad \boldsymbol{n_z} = \begin{bmatrix} 0 & 0 & 1 & 0 & 0 & 0 \end{bmatrix}^T \tag{3.29}$$

Assume that the following cost function has to be minimized according to the task specification:

$$u = \frac{1}{f_z}\|\boldsymbol{\tau}\|_{\boldsymbol{W}} = \frac{1}{f_z}\sqrt{\boldsymbol{\tau}^T\boldsymbol{W}\boldsymbol{\tau}} = \sqrt{\boldsymbol{n_z}^T\boldsymbol{J}_{\boldsymbol{\omega}}^{\boldsymbol{tcp}}\boldsymbol{W}\boldsymbol{J}_{\boldsymbol{\omega}}^{\boldsymbol{tcp}^T}\boldsymbol{n_z}} \tag{3.30}$$

where

$$\boldsymbol{W} = \boldsymbol{\Sigma}^{-1}\boldsymbol{T_{max}}^{-2}\boldsymbol{\Sigma}^{-T} > 0 \tag{3.31}$$

while $\boldsymbol{\Sigma}$ is the matrix containing the motor gear ratios (such that the motor torque $\boldsymbol{\tau_m}$ is $\boldsymbol{\tau_m} = \boldsymbol{\Sigma}^{-T}\boldsymbol{\tau}$) and $\boldsymbol{T_{max}}$ is a diagonal matrix containing the maximum allowed torque each motor can provide.
Again, the minimality of the cost function can be turned into the following holonomic constraint:

$$\sigma(\boldsymbol{q}) = \boldsymbol{N}^T\left(\frac{\partial u}{\partial \boldsymbol{q}}\right)^T = 0 \tag{3.32}$$

where $\boldsymbol{N}$ is any null-space basis of the task Jacobian $\boldsymbol{J}$. In this way, the robot posture will be such that the required motor torque effort per thrust force unit can be reduced to the minimum value, yielding a more efficient drilling. Moreover, the minimality of the cost function ensures the embedded position/velocity controller to possibly stay away from torque limits.
As a matter of completeness, the gravitational load $\boldsymbol{g}(\boldsymbol{q})$ should be considered, as well. However, re-orienting the tool along the null-space direction $\boldsymbol{N}$ mainly involves a motion of the wrist joints and as such does not affect the gravitational load significantly. In other words $\boldsymbol{N}^T\partial\boldsymbol{g}/\partial\boldsymbol{q}$ is small and thus can be neglected in defining the cost function.
A number of $M = 3000$ Monte Carlo samples according to the optimality constraint (3.32) have been generated. Then, the function $p^0(\cdot)$ required in the redundancy resolution algorithm has been selected within a functional space composed of linear functions of the task variables and a modified truncated Fourier series, yielding

$$\begin{aligned} p(\boldsymbol{\mu}) = {} & 4.06y - 1.62\theta + 0.62\sin(3/2\theta)\sin(9/2\rho) + \\ & + 0.21\cos(5\rho) - 0.19\sin(5/2\rho) \end{aligned} \tag{3.33}$$

corresponding to an acceptance threshold of $F_{TH}^0 = 7\,\mathrm{deg}$. This way, the third ZYZ Euler angle ϕ will be planned in order to select the robot posture such that the normalized motor torque effort in (3.30) is minimized, with a Root Mean Square (RMS) error of less than $7\,\mathrm{deg}$.
In order to perform the drilling operation, a force tracking module must be adopted. In this work an admittance filter [41] is used to: (a) smoothen the transition between non-contact and contact motion, (b) allow the force tracking required for

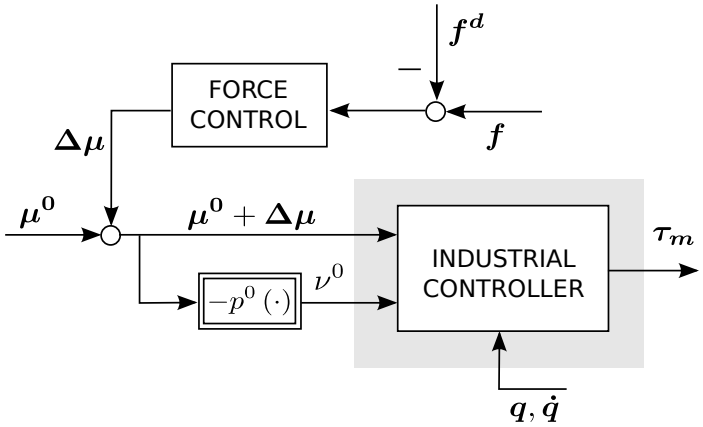

Figure 3.19: *Control architecture for redundancy resolution and force tracking*

the drilling task, [56]. In particular, the force tracking control is implemented as follows:

$$\boldsymbol{B}\frac{d^2}{dt^2}\begin{bmatrix}\Delta x\\ \Delta y\\ \Delta z\end{bmatrix} + \boldsymbol{D}\frac{d}{dt}\begin{bmatrix}\Delta x\\ \Delta y\\ \Delta z\end{bmatrix} + \boldsymbol{K}\begin{bmatrix}\Delta x\\ \Delta y\\ \Delta z\end{bmatrix} = \boldsymbol{f} - \boldsymbol{f^d} \tag{3.34}$$

where $\boldsymbol{f}$ is the measured force, $\boldsymbol{f^d}$ is the force reference, $\boldsymbol{B} > 0, \boldsymbol{D} \geq 0, \boldsymbol{K} \geq 0$ are the impedance parameters and

$$\boldsymbol{\Delta\mu} = \begin{bmatrix}\Delta x & \Delta y & \Delta z & 0 & 0\end{bmatrix}^T \tag{3.35}$$

Notice that the last two elements of $\boldsymbol{\Delta\mu}$ have been set to zero because we assume to accurately plan the approach motion, so that the drill will be exactly perpendicular to the workpiece.

The experiments were carried out on an ABB IRB 140 industrial robot, endowed with an ABB IRC 5 controller[3] featuring an external sensor interface used for the force tracking [16]. The contact forces were measured using a 6-axes JR3 wrist-mounted force/torque sensor. The tool was equipped with a $3\ mm$ diameter drill.

Two types of experiments were performed: (a) manual guidance (in which the position of the tool is manually adjusted by the human operator) and (b) force control.

[3] Since the required interface to implement the force control algorithm in Fig. 3.19 was not available, the entire diagram was implemented in an open controller so that the block labeled *Embedded Inverse Kinematics* in Fig. 2.1 actually contains a duplication of the code embedded in the industrial controller.

3.4.1 Manual guidance experiment

During the manual guidance experiment, only the impedance control was active, namely $\boldsymbol{f^d} = \mathbf{0}$, with $\boldsymbol{B} = 5\boldsymbol{I_3}, \boldsymbol{D} = 4\boldsymbol{I_3}$ and $\boldsymbol{K} = \boldsymbol{I_3}$. The impedance parameters were defined in order to allow the user to easily move the robot. During the experiment, the redundancy resolution implemented in the function $p^0(\cdot)$ in (3.33) was running, modifying the Euler angle ϕ in such a way that at any time the robot was ready to perform drilling with a minimum torque effort. In fact, as one can see from Fig. 3.19, the measured force $\boldsymbol{f}$ actively participates in the calculation of the reference for third Euler angle $\nu^0 = \phi^0 = -p^0(\boldsymbol{\mu^0} + \boldsymbol{\Delta\mu})$. While the operator was moving the tool, as one can see in Fig. 3.20, the optimality requirement, which implies $\sigma(\boldsymbol{q}) = 0$, was achieved within an acceptable tolerance, as confirmed by Fig. 3.21, which compares the actual orientation of the tool to the one computed with the extended Jacobian method.

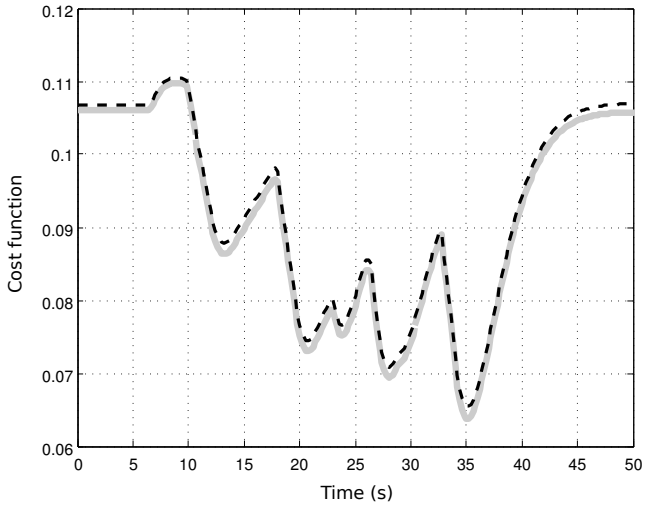

Figure 3.20: *Cost function: extended Jacobian (simulated, solid gray) and proposed method (experimental, dashed black)*

Both in the case of manual guidance and in the case where cameras are used to estimate drilling position, the tool pose is not a-priori known. Then, the robot posture cannot be optimized offline. A standard optimization technique, such as a nonlinear programming, can be either too time-consuming or hardly implementable on top of the existing industrial controller. In this first experiment we have shown that good results can be achieved with a slight modification built on top of the existing kinematic controller, and then preserving all the previously implemented protections such as torque, velocity or joint limits and singularity avoidance procedures.

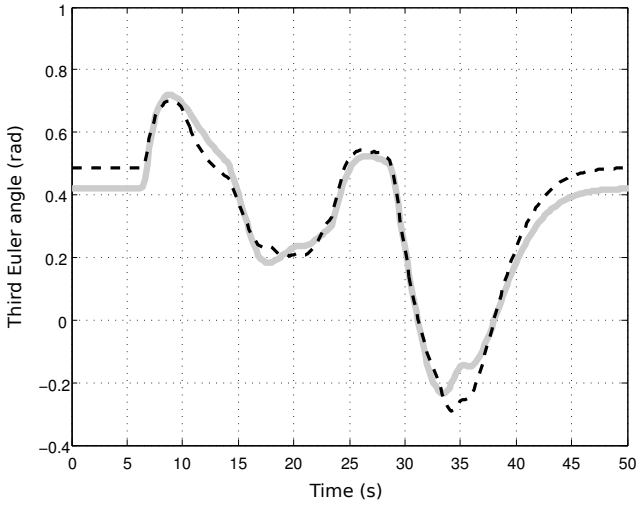

Figure 3.21: *Third Euler angle ν: extended Jacobian (simulated, solid gray) and proposed method (experimental, dashed black)*

3.4.2 Force control experiment

A set of three experiments with the robot interacting with the environment are now presented. The workpiece was a $8\ mm$ thick hard rubber plate with an expected stiffness of $25\ N/mm$, so that the robot could be considered stiff.
In all the experiments, the robot first approached the workpiece with a pure position/velocity controller. Then, when in contact, the controller started tracking a force reference $\boldsymbol{f^d}$ with a steady state value of $50\ N$. The selected parameters for the force controller (3.34) were $\boldsymbol{B} = 165\boldsymbol{I_3}$, $\boldsymbol{D} = 16700\boldsymbol{I_3}$ and $\boldsymbol{K} = \boldsymbol{0}$.
During the first experiment, the function $p^0(\cdot)$ in (3.33) was used as a redundancy resolution technique. We stress that such a function has been tuned in order to enforce a torque-effective requirement, which implies that the same thrust force can be exerted with a minimum motor torque effort. In Fig. 3.22 the measured force referred to the world frame is compared to its reference.
The same experiment was carried out with two trivial redundancy resolution techniques, namely letting[4] $\phi = -p^0(\cdot) = 2\pi/3, \forall t$ and $\phi = -p^0(\cdot) = -2\pi/3, \forall t$. In Figs. 3.23 and 3.24 the measured forces are shown together with their references. As one can see in all the three experiments the actual thrust force is the same which means that the force tracking task was accomplished.
However since the robot pose was different, due to the different redundancy resolution techniques, a different torque effort was expected. In Fig. 3.25, the norm of the normalized motor torque $\boldsymbol{\tau_m}$, namely $1/\sqrt{6}\sqrt{\boldsymbol{\tau_m}^T \boldsymbol{T_{max}}^{-2} \boldsymbol{\tau_m}}$ is shown. As

[4]Notice that letting $\boldsymbol{\mu}$ the vector of the task variables desired drilling position, using the function $p^0(\cdot)$ in (3.33), one obtains $p^0(\boldsymbol{\mu}) \approx 0$, so the values $\pm 2\pi/3$ have been selected in order to roughly span the self-motion manifold.

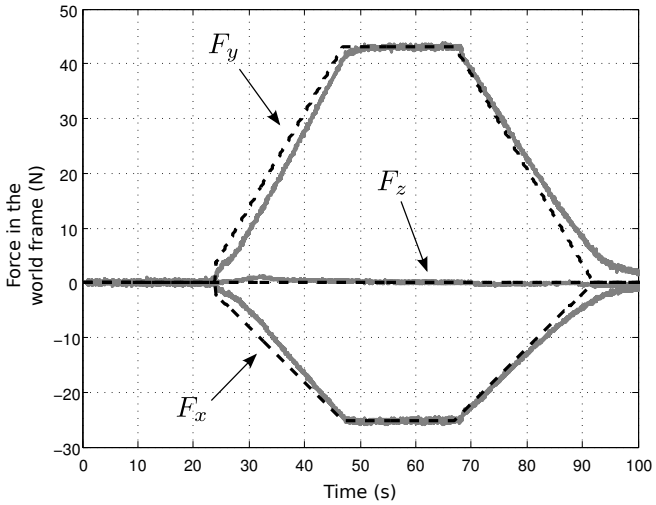

Figure 3.22: *Force tracking with $p^0(\cdot)$ in* (3.33)*: actual value (solid), reference (dashed)*

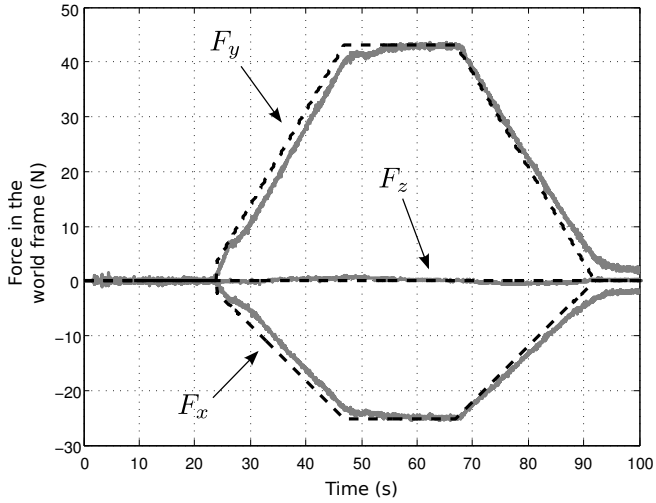

Figure 3.23: *Force tracking with $p(\cdot) = 2\pi/3$: actual value (solid), reference (dashed)*

expected, using the redundancy resolution technique defined in (3.33), the motor torque effort can be significantly reduced. Notice that, when the force reference was at steady state, namely from time instant $50\ s$ to approximately $65\ s$, the difference between the motor effort is remarkable (the worst-case experiments requires up to 12% of additional motor torque effort). In other terms, despite the simplicity of the adopted model to relate tool forces to motor torques, the selected function $p^0(\cdot)$ in (3.33) guaranteed the torque-effective criterion.

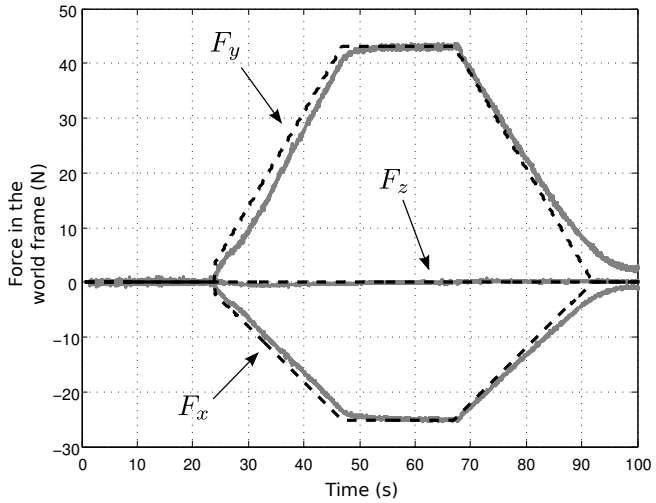

Figure 3.24: *Force tracking with $p^0(\cdot) = -2\pi/3$: actual value (solid), reference (dashed)*

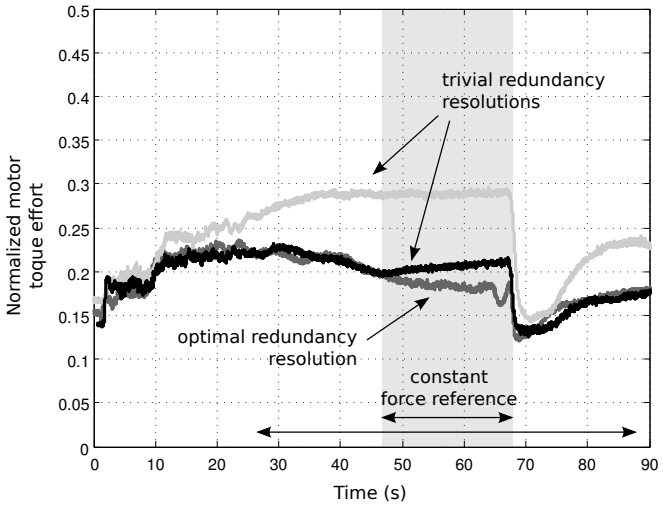

Figure 3.25: *Comparison of the normalized motor torque efforts with the three different redundancy resolution strategies: optimal redundancy resolution (dark solid gray), $\nu = \phi = 2\pi/3$ (solid black) and and $\nu = \phi = -2\pi/3$ (light solid gray)*

3.5 Summary

The redundancy resolution framework presented in Chapter 2 has been applied in different experimental scenarios. In particular, the modularity of the proposed approach has been exploited in almost all the experiments by implementing the redundancy resolution criterion on top of the existing inverse kinematics algorithm. The natural extension of the framework to the case of multiple degrees of

redundancy has been shown. Finally, the specification of different requirements, ranging from kineto-static (e.g. for spray painting and for drilling) to dynamic ones (in the case of cooperating robots), has been discussed.

Part II

Analysis and synthesis of the human arm motion

CHAPTER 4

Motion capture experiments

One of the objectives of this work is to endow robot controllers with new functionalities that are "human-centered", in order to allow for safe physical cooperation and interaction with the human co-worker(s). This cooperation should not just be physically safe, but also psychologically comfortable to the humans. For this the robot should execute its tasks with motion profiles that humans perceive as natural, intuitive and predictable. It is here conjectured that making the motion of the robotic arm resemble the motion of a human arm is a reasonable way to achieve this goal: a human worker shall feel comfortable if working side-by-side with a robotic arm that performs its task in a similar way as a fellow human co-worker.

The point is therefore to investigate how humans resolve the kinematic redundancy of their arms. Several questions arise: what is a suitable kinematic model of the human arm? can it be represented with the same formalism (e.g. Denavit-Hartenberg parameters) as robotic arms? what is a consistent way to represent kinematic redundancy of the human arm? do humans resolve redundancy by enforcing a kinematic constraint among kinematic variables, which is identifiable and repeatable? if so, is this constraint holonomic?

This Chapter describes the experimental campaign on volunteers organized to gather all the data needed to study the human arm motion. The experimental data will be analyzed in next Chapter where part of the mentioned questions will be

addressed.

4.1 Description of the experiments

The concept exploited in the experiments is the motion capture, whereby some volunteers have been instructed on the operations they were supposed to perform, and the motion of their arm was tracked through visual recording of markers attached to the arm itself. The experimental apparatus as well as the protocol of the experiments are described in this Section.
During the experiments, the hand was constrained to move with the palm on a rigid smooth sphere of $70\ mm$ radius placed on a work bench. The height of the work bench has been selected as $1090\ mm$, as prescribed by the standards on anthropometric requirements for the design of workstations at machinery [1]. The motion of the human arm, which this way resembles basic assembly operations, is partially constrained, but the motion of the hand along the spherical surface can be performed freely as depicted in Fig. 4.1. Thanks to motion capture techniques, the motion of the human arm was tracked through visual recording of markers attached to the arm itself.

4.1.1 Experimental apparatus and marker set

A commercial optoelectronic motion capture system, VICON (Oxford, UK), consisting of six T10 cameras (resolution 1 MP and frame-rate 200 Hz) with near infrared strobes was used. The system can track the 3D coordinates of markers (retro-reflective spheres) attached to the subjects. For the data cleaning the NEXUS software VICON (Oxford, UK) was used. When the markers were not visible from the cameras for a short duration of time, the missing points of their tracks were interpolated with the spline interpolation algorithm [119] as provided from the NEXUS software.

Eight healthy volunteers were selected between the $50th$ and $95th$ percentile, see [2]. Anthropometric measurement of the volunteers' right arm was performed before the experiment. The following marker arrangement was considered:

- one marker on the 7th cervical vertebra (C7);
- one marker on the 10th thoracic vertebra;
- one marker on the xiphoid process on the sternum;
- one marker on the incisura jugularis (IJ) on the sternum;
- the remaining markers are arranged as shown in Fig. 4.2.

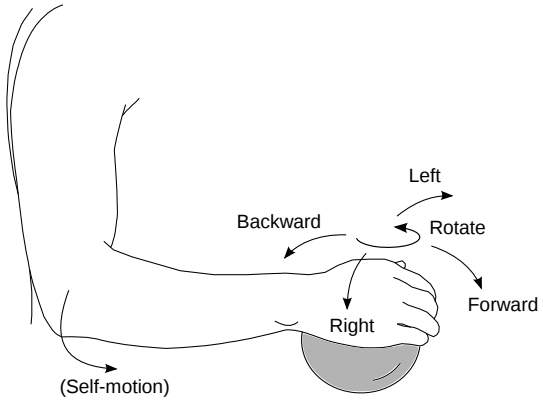

Figure 4.1: *Hand's admissible motion acts on the spherical surface*

A very similar arrangement for the markers has been proposed in the biomechanics literature, see e.g. [99].

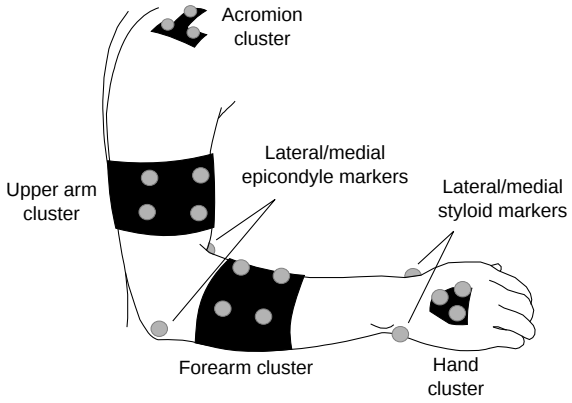

Figure 4.2: *Markers arrangement*

4.1.2 Protocol of the experiments

The experiments were performed with the aim to capture the natural motions of the volunteers' arm during manual operations with average demand in visual and motor control. Some motions had to be performed in advance in order to get accustomed, and execute the motion under measurement as naturally as possible. Each volunteer was asked to take a comfortable posture before the measurement and change the posture to a more comfortable one in case of significant translational motion of the shoulder. The feet position had to remain fixed during the experiments, while the horizontal distance of the torso from the work bench had

to be around $100\ mm$. The mid-sagittal plane of the volunteer had to be at a predefined position relative to the work bench. The volunteer had to avoid stopping between the motion parts of each command, and to overlap motions parts. Talcum-powder was used to reduce the friction between the hand and the sphere. Five repetitions of each motion had to be performed, waiting $1\ s$ between every repetition.
Before every motion a command was given to the volunteers describing the motion to be executed. This way the volunteer was able to get acquainted with the motion to be performed. The researcher observed if the volunteers' motions were performed according to these instructions.
A reference motion capture was performed before the actual experiment to calculate the locations of the markers placed on anatomical landmarks, especially the markers on the humeral epicondyles and the forearm styloid processes, relative to the marker clusters (technical frames). This process was performed because these markers were hidden from the cameras during long intervals. The calibration motions are described in Fig. 4.3. A set of simple motions resembling typical

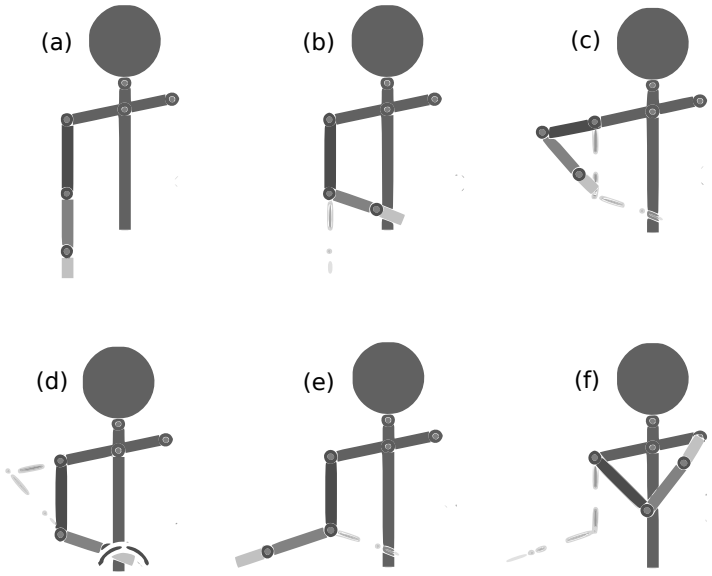

Figure 4.3: *Calibration motions: (a) natural anatomical posture, (b) elbow flexion, (c) arm abduction, (d) pronation-supination, (e) humeral axial rotation (f) generic motion*

movements during assembly operations were performed as reported in Tab. 4.1.
The output data of the measurement were the Cartesian coordinates of each marker over time. Some potential errors that can influence the measured data are the followings:

1. skin artifacts;

Position			
Hand	Code	Motion	Duration
top	A, B	(1) forward 45 deg	1.5 s
		(2) backward 45 deg	1.5 s
		(3) right 90 deg - forward 90 deg	3 s
		(4) anticlockwise 60 deg - backward 90 deg	3 s
		(5) anticlockwise 90 deg - forward 90 deg	3 s
top	C, D	(1) right 90 deg - clockwise 45 deg	3 s
		(2) right 90 deg - backward 45 deg	3 s
bottom	VA, VB	(1) right 180 deg - forward 45 deg	4 s
		(2) right 180 deg - clockwise 45 deg	4 s

Table 4.1: *Benchmark motions for the motion capture experiments*

(a) experiment A(3) (b) experiment D(2)

Figure 4.4: *One volunteer during the experiments*

2. markers' visibility lost during motion for extended time period.

4.2 Kinematic model of the human arm

The first step in the analysis consists in the selection of a model for the human arm. The choice is the result of a compromise between representativeness of the model and its usefulness for the subsequent analysis on redundancy. The kinematic redundancy of the arm is then characterized in terms of an analytical expression for the basis of the null-space of the geometrical Jacobian. A suitably defined angle is then considered as an effective way to describe the human arm self-motion.

In this work, the kinematically redundant model of the human (right) arm depicted in Fig. 4.5 is considered. The model consists of 7 revolute joints. The first three joints, q_1, q_2 and q_3, take into account the motion of the shoulder complex (i.e. the Gleno-Humeral Joint (GHJ)). It is commonly agreed that such joint

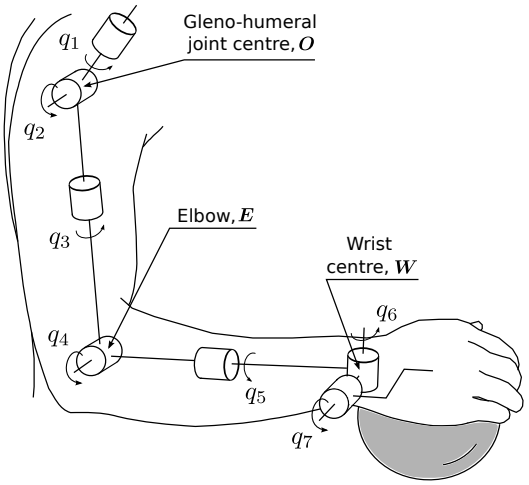

Figure 4.5: *Kinematic model of the human arm*

contains two translational degrees of freedom. However, since the surfaces of the head of the humerus is more than 99% spherical [107], it is well modeled as a ball-and-socket joint. The fourth joint, q_4, represents the elbow, while the last three joints, q_5, q_6 and q_7, take part in a spherical wrist. The former represents the motion of pronation/supination of the upper arm, the latter represent the radio-ulna deviation axis and the flexion/extension of the wrist, respectively. As reported in [126], a small separation between these two axes exists. Moreover, as reported in the literature, the flexion/extension axis of the wrist usually anticipates the radio-ulna deviation axis. In this analysis, the distance between the two axes of motion of the wrist will be neglected. In this way, their relative order is totally irrelevant.
The Denavit-Hartenberg parameters of the kinematic chain depicted in Fig. 4.5 are shown in Tab. 4.2.

The geometrical Jacobian $\boldsymbol{J}_{\boldsymbol{\omega}}$, that describes the relationship between the joint velocities and the twist of the hand frame, can be computed with well-known algorithms [103]. Since the geometrical Jacobian of the human arm is a 6×7 matrix, it admits a non trivial null-space $\mathcal{N}\left(\boldsymbol{J}_{\boldsymbol{\omega}}\right)$, containing joint velocities that do not modify the position and orientation of the hand. It is possible to compute a basis of the null-space as proposed in [117] or with support of any tool of

	Parameters			
axis	a_i	d_i	α_i	θ_i
1	0	0	$\pi/2$	q_1
2	0	0	$\pi/2$	q_2
3	0	d_3	$-\pi/2$	q_3
4	0	0	$-\pi/2$	q_4
5	0	d_5	$\pi/2$	q_5
6	0	0	$\pi/2$	q_6
7	0	0	0	q_7

Table 4.2: *Denavit-Hartenberg parameters of the kinematic model*

symbolic manipulation, yielding

$$\boldsymbol{N} = \begin{bmatrix} d_5 c_3 s_4 s_6 \\ d_5 s_4 s_3 s_2 s_6 \\ \left(d_5 s_2 c_4 - d_3 s_2 + d_5 s_4 c_2 c_3\right) s_6 \\ 0 \\ -s_2 \left(d_3 c_4 s_6 - d_5 s_6 + d_3 c_6 c_5 s_4\right) \\ -d_3 s_4 s_2 s_5 s_6 \\ -d_3 s_2 c_5 s_4 \end{bmatrix} \tag{4.1}$$

where $c_i = cos\left(q_i\right)$ and $s_i = sin\left(q_i\right)$.
Notice that, as reported in [117], the elbow joint (i.e. joint 4) does not participate in any self-motion, in accordance with the behavior of a real human arm. In other words, when the hand is completely constrained, the angle between the forearm and the forelimb (i.e. the elbow joint value) is constrained, too.
Let $\boldsymbol{E}$ and $\boldsymbol{W}$ be the origins of frames 4 and 7, respectively (see Fig. 4.5 and 4.6) and consider the vectors $\boldsymbol{w} = (\boldsymbol{W} - \boldsymbol{O})$ and $\boldsymbol{e} = (\boldsymbol{E} - \boldsymbol{O})$. Denote with $d = d\left(\boldsymbol{q}\right)$ the distance from point $\boldsymbol{E}$ to the axis lying on the vector $\boldsymbol{w}$. Then, since

$$\boldsymbol{N}^T \left(\frac{\partial d}{\partial \boldsymbol{q}}\right)^T = 0, \forall \boldsymbol{q} \tag{4.2}$$

it follows that d is an invariant with respect to a self-motion of the arm. In other terms if $\dot{\boldsymbol{q}} = \dot{\beta}\boldsymbol{N}$ then $\dot{d} = 0, \forall \dot{\beta} \in \mathbb{R}$. Therefore, the distance between the elbow and the segment connecting the shoulder to the wrist is uniquely determined, once the position of the center of the wrist is known. Finally, since d does not vary during a self-motion it follows that the remaining degree of freedom allows the elbow $\boldsymbol{E}$ to describe a circumference of radius d. Then, the human arm self-motion can be naturally described in terms of an angle.
Such an angle ν, from now on referred to as *elbow swivel angle*, can be defined as

the angle between two planes, as depicted in Fig. 4.6, where A is the half-plane containing vectors $\boldsymbol{z}$ and $\boldsymbol{w}$, while Ω is the half-plane containing vectors $\boldsymbol{e}$ and $\boldsymbol{w}$. The angle can be calculated as follows, (see [67] for a detailed overview on

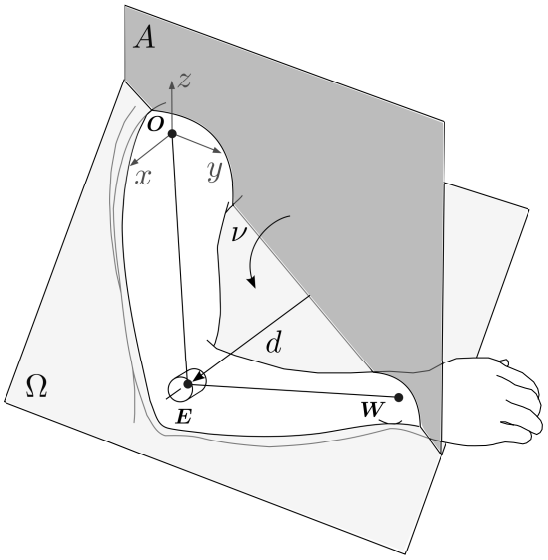

Figure 4.6: *Definition of the elbow swivel angle*

the use of this angle to describe the redundancy of a 7-DOF arm):

$$\nu = atan2\left(\boldsymbol{u}^T\left(\boldsymbol{z}\times\boldsymbol{p}\right), \boldsymbol{z}^T\boldsymbol{p}\right) \tag{4.3}$$

where $\boldsymbol{p} = \left(\boldsymbol{I} - \boldsymbol{u}\boldsymbol{u}^T\right)\boldsymbol{e}$ and $\boldsymbol{u} = \boldsymbol{w}/\left\|\boldsymbol{w}\right\|$. It is straightforward to realize that ν is a function of the joint variables $\boldsymbol{q}$, i.e. $\nu = \nu\left(\boldsymbol{q}\right)$. It can be proven that the augmented Jacobian $\boldsymbol{J_A}$ defined as follows

$$\boldsymbol{J_A} = \begin{bmatrix} \boldsymbol{J_\omega}^T & \left(\dfrac{\partial\nu}{\partial\boldsymbol{q}}\right)^T \end{bmatrix}^T \tag{4.4}$$

is singular if and only if $\boldsymbol{J_\omega}$ is rank deficient. In other words, the elbow swivel angle ν represents a consistent way to describe the redundancy of the human arm.

4.3 Reconstruction of joint variables

For each experiment, rough data consist of Cartesian coordinates of each marker, over the time, referred to the NEXUS reference frame. The model reference frame, depicted in Fig. 4.6, has been defined as follows:

- z-axis vertical pointing upward, x-axis pointing to the right (away from the torso);

- origin $\boldsymbol{O} = \begin{bmatrix} x_O & y_O & z_O \end{bmatrix}^T$: time-averaged center of the GHJ, one for each volunteer, calculated with a well-known formula, see [25]

$$\begin{aligned} x_O &= 96.2 - 0.302 \left\| (\boldsymbol{IJ} - \boldsymbol{C7}) \right\| - 0.364 H_i + 0.385 W_i \\ y_O &= 0.30 \left\| (\boldsymbol{IJ} - \boldsymbol{C7}) \right\| \, | - 66.32 - 0.432 W_i \\ z_O &= 66.468 - 0.531 \left\| \left(\frac{\boldsymbol{AcrB} + \boldsymbol{AcrF}}{2} - \frac{\boldsymbol{IJ} + \boldsymbol{C7}}{2} \right) \right\| + 0.571 W_i \end{aligned} \tag{4.5}$$

  using the markers on the acromion cluster (AcrF, AcrB and AcrL), the markers on the IJ and on the C7, the volunteer's height H_i and weight W_i.

Then, in order to perform an inter-volunteer comparison, acquired marker positions have been first referred to the frame introduced above and then normalized to a unitary arm length, using the normalizing factor $1/L_i$ where $L_i = U_i + F_i$ is the arm length of volunteer $i = 1, \ldots, 8$, while U_i and F_i are the upper- and forearm lengths, respectively.
Parameters d_3 and d_5 of the model, see Tab. 4.2, have then been selected as follows:

$$d_3 = 1 - \frac{1}{8} \sum_{i=1}^{8} R_i = 0.5174 \quad d_5 = \frac{1}{8} \sum_{i=1}^{8} R_i = 0.4826 \tag{4.6}$$

where $R_i = F_i / L_i$.
Notice that, at this point, all the marker measurements are comparable, since they are referred to the same frame and correspond to an arm with the same (unitary) length.

The next step after data normalization is the reconstruction of joint variables, i.e. of the variables of the kinematic model of the human arm introduced in Section 4.2, that best correspond to the output of the motion capture experiments. Following the approach proposed in [32], an Extended Kalman Smoother (EKS) is used to estimate joint variables. The model adopted in the smoother consists in a chain of four integrators for each joint variable. The state-update equation is, therefore, linear, while the output equations, three for each marker accounting for the marker kinematics, are nonlinear. Introducing the unbiased process white

noise $\boldsymbol{\xi}$ and the unbiased measurement white noise $\boldsymbol{\zeta}$, we obtain:

$$\begin{bmatrix} \boldsymbol{q}(k+1) \\ \dot{\boldsymbol{q}}(k+1) \\ \ddot{\boldsymbol{q}}(k+1) \\ \dddot{\boldsymbol{q}}(k+1) \end{bmatrix} = \begin{bmatrix} \boldsymbol{I} & \boldsymbol{I}\epsilon & \boldsymbol{I}\epsilon^2/2 & \boldsymbol{I}\epsilon^3/6 \\ \boldsymbol{0} & \boldsymbol{I} & \boldsymbol{I}\epsilon & \boldsymbol{I}\epsilon^2/2 \\ \boldsymbol{0} & \boldsymbol{0} & \boldsymbol{I} & \boldsymbol{I}\epsilon \\ \boldsymbol{0} & \boldsymbol{0} & \boldsymbol{0} & \boldsymbol{I} \end{bmatrix} \begin{bmatrix} \boldsymbol{q}(k) \\ \dot{\boldsymbol{q}}(k) \\ \ddot{\boldsymbol{q}}(k) \\ \dddot{\boldsymbol{q}}(k) \end{bmatrix} + \boldsymbol{\xi}(k) \tag{4.7}$$
$$\boldsymbol{y}(k) = \boldsymbol{m}(\boldsymbol{q}(k)) + \boldsymbol{\zeta}(k)$$

where $\epsilon = 1/200\ s$ is the discrete time-step.
The extended version of the Kalman filter, in the form of the Rauch-Tung-Striebel smoother [92], has been adopted in order to simultaneously estimate the joint variables and their time-derivatives:

$$\begin{aligned} \text{Prediction: } \hat{\boldsymbol{x}}_{\boldsymbol{k|k-1}} &= \boldsymbol{F_k}\hat{\boldsymbol{x}}_{\boldsymbol{k-1|k-1}} \\ \boldsymbol{P_{k|k-1}} &= \boldsymbol{F_k}\boldsymbol{P_{k-1|k-1}}\boldsymbol{F_k}^T + \boldsymbol{Q_{k-1}} \end{aligned} \tag{4.8a}$$

$$\begin{aligned} \text{Update: } \boldsymbol{K_k} &= \boldsymbol{P_{k|k-1}}\boldsymbol{M_k}^T\left(\boldsymbol{M_k}\boldsymbol{P_{k|k-1}}\boldsymbol{M_k}^T + \boldsymbol{R_k}\right)^{-1} \\ \boldsymbol{P_{k|k}} &= \left(\boldsymbol{I} - \boldsymbol{K_k}\boldsymbol{M_k}\right)\boldsymbol{P_{k|k-1}} \\ \hat{\boldsymbol{x}}_{\boldsymbol{k|k}} &= \hat{\boldsymbol{x}}_{\boldsymbol{k|k-1}} + \boldsymbol{K_k}\left(\boldsymbol{y_k} - \boldsymbol{m}\left(\hat{\boldsymbol{x}}_{\boldsymbol{k|k-1}}\right)\right) \end{aligned} \tag{4.8b}$$

$$\begin{aligned} \text{Smoothing: } \tilde{\boldsymbol{x}}_{\boldsymbol{k-1}} &= \hat{\boldsymbol{x}}_{\boldsymbol{k-1|k-1}} \\ &+ \boldsymbol{P_{k-1|k-1}}\boldsymbol{F_{k-1}}^T\left(\boldsymbol{P_{k-1|k-1}}\right)^{-1}\left(\tilde{\boldsymbol{x}}_{\boldsymbol{k}} - \hat{\boldsymbol{x}}_{\boldsymbol{k|k-1}}\right) \end{aligned} \tag{4.8c}$$

where $\boldsymbol{x} = \begin{bmatrix} \boldsymbol{q}^T & \dot{\boldsymbol{q}}^T & \ddot{\boldsymbol{q}}^T & \dddot{\boldsymbol{q}}^T \end{bmatrix}^T$, $\boldsymbol{M} = \partial\boldsymbol{m}/\partial\boldsymbol{x}$, $\boldsymbol{F_k}$ is the (constant) state-update matrix in (4.7), while $\boldsymbol{Q_k} = \boldsymbol{Q_k}^T > 0$ and $\boldsymbol{R_k} = \boldsymbol{R_k}^T > 0$ are state and output noise (constant) covariance matrices, respectively.

In Fig. 4.7 the output of the EKS in terms of joint angles is shown. The output of the EKS $\tilde{\boldsymbol{x}}(k)$, and in particular the time history of the estimated joint variables $\tilde{\boldsymbol{q}}(k)$, has been used to develop an animated reconstruction of the acquired motion. Figure 4.8 shows two snapshots corresponding to a couple of different experiments performed by two different volunteers.

4.4 Summary

In this Chapter, a suitable kinematic model of the human arm has been identified and its self-motion manifold has been characterized. Motion capture experiments have been performed in order to study the motion of human arm in some predefined operations. The rough experimental data have been post-processed using Kalman filtering techniques aimed at computing a more synthetic representation

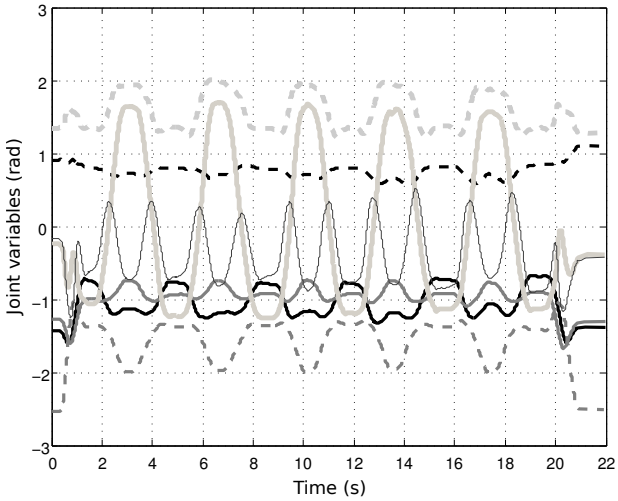

Figure 4.7: *Joint variables during experiment VB(1), volunteer 2 (q_1: solid black, q_2: solid gray, q_3: dashed black, q_4: dashed gray q_5: solid light gray, q_6: dashed light gray and q_7: thin black)*

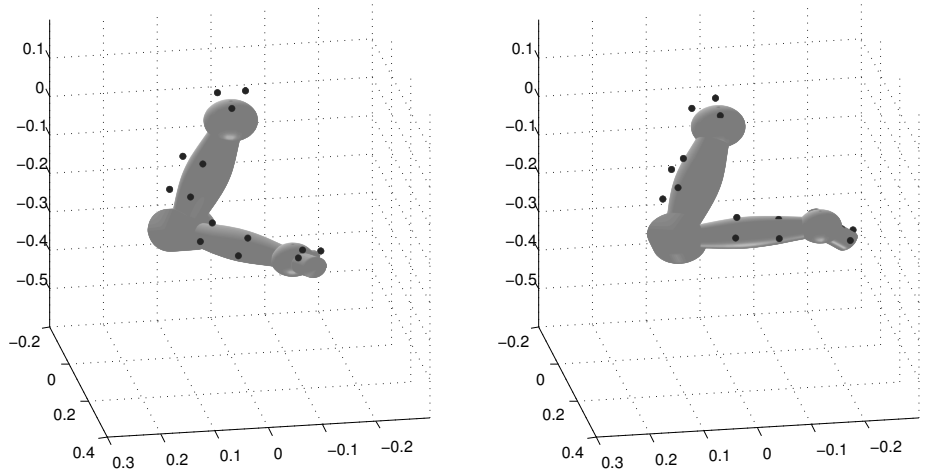

(a) experiment A(1), volunteer 1

(b) experiment A(5), volunteer 3

Figure 4.8: *EKS-based reconstruction of the human arm posture from marker measurements (acromion, upper-, lower-arm, and hand clusters are shown only)*

(i.e. trajectory in the joint space in place of time histories of each marker in the Cartesian space) of the data. A detailed analysis of the collected data and the identification of a redundancy resolution criterion will be addressed in next Chapter.

CHAPTER 5

Identification of natural postures

The problem addressed in this Chapter is to check whether during the experiments a relation between the hand position/orientation and the swivel angle can be identified. Data clustering is applied in order to have a manageable set of data on which statistical analysis will be performed. Then, an expression of such relation is derived and validated. Finally, by exploiting the symmetry of the human upper body, such relationship is adapted to suit the case of the left arm.

5.1 Correlation analysis of task variables

First, a minimal description of the hand frame should be introduced. For this, let

$$\boldsymbol{\mu} = \begin{bmatrix} x & y & z & \rho & \theta & \phi \end{bmatrix}^T \tag{5.1}$$

be the vector of hand position (x, y, z are the Cartesian coordinates of the wrist center) and orientation (ZYZ Euler angles have been used for ρ, θ and ϕ). In Figs. 5.1, 5.2 and 5.3 the time history of the hand Cartesian position and orientation and of the joint angles (the output of the EKS introduced in the previous Chapter) are shown, respectively. Notice that the given trajectory of the hand $\boldsymbol{\mu}(t)$ as well as the corresponding behavior of all the joint variables are *cyclic* (namely periodic). Theorem 2.1 of Chapter 2 ensures that whenever a kinematic control strategy is

cyclic, then a constraint of the form $\nu + p(\boldsymbol{\mu}) = 0$ is enforced during the motion. We want to investigate whether a relationship between the hand pose $\boldsymbol{\mu}$ and the swivel angle ν, such that $\nu = -p(\boldsymbol{\mu})$, is likely to exist. In other words, the hypothesis we would like to prove is that during a partly constrained motion of the hand (due to some task one is supposed to perform), the elbow, and then the entire arm, assumes a position that is fully correlated with the pose of the hand.

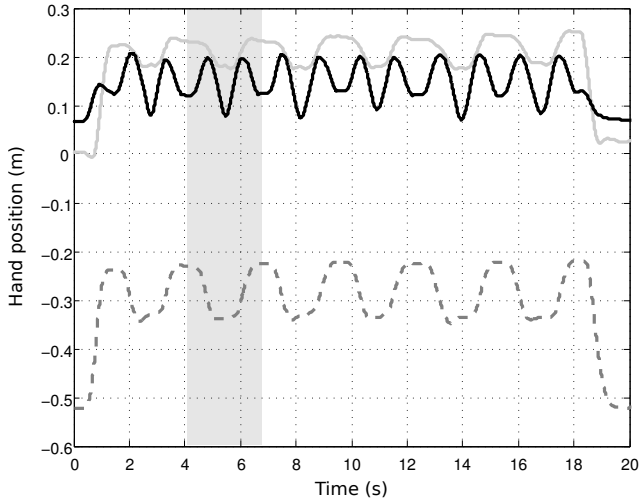

Figure 5.1: *Hand Cartesian position during experiment C(2), volunteer 1 (x: solid black, y: solid gray and z: dashed gray)*

In [58] and [65], such a relationship is conjectured, assuming, however, that it exists only between the elbow swivel angle and a partial description of the hand pose (the Cartesian position, expressed in spherical coordinates, together with the palm roll angle in the former paper and the Cartesian position in the latter). In [124] instead, it has been pointed out that this relationship, if it exists, should take into account the full description of the orientation of the hand together with its Cartesian position. However, there is no particular evidence about the existence of such a correlation and the particular behavior observed in Fig. 5.3 is certainly not sufficient to be generalized.
A statistical verification of the existence of this relationship, at least during the operations considered in the experimental campaign, is thus required.

An equivalent way to set our problem is to prove the existence of a configuration manifold $\nu + p(\boldsymbol{\mu}) = 0 \Leftrightarrow \sigma(\boldsymbol{q}) = 0$. This problem can be tackled with the tools of information theory, e.g. using the concept of information entropy, see e.g. [120], which measures the "amount of information" in a data set. In fact, assuming that a constraint of the kind $\sigma(\boldsymbol{q}) = 0$ holds, the motion is limited to

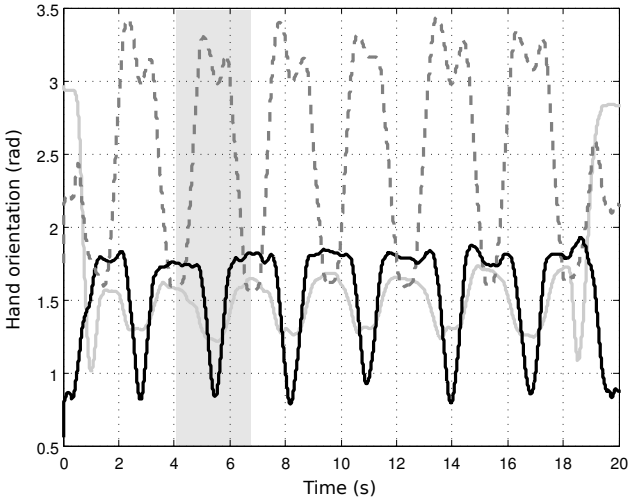

Figure 5.2: *Hand orientation during experiment C(2), volunteer 1 (ρ: solid black, θ: solid gray and ϕ: dashed gray)*

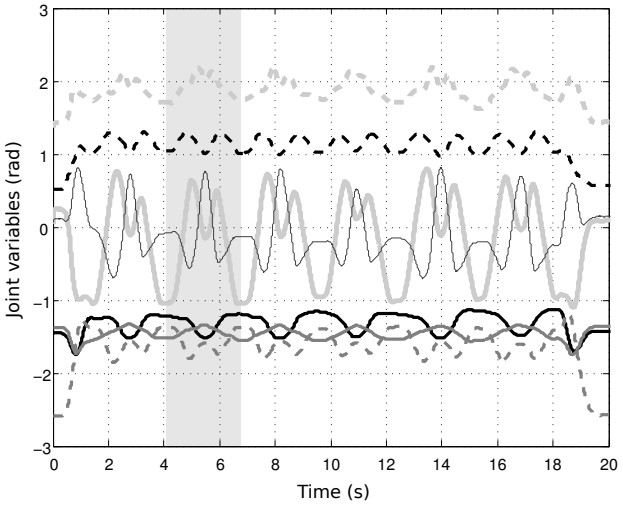

Figure 5.3: *Joint variables during experiment C(2), volunteer 1 (q_1: solid black, q_2: solid gray, q_3: dashed black, q_4: dashed gray q_5: solid light gray, q_6: dashed light gray and q_7: thin black)*

lie in a lower-dimensional manifold. In this case, the pose of the arm could be described using a reduced set of variables. The information entropy measures the amount of information (in terms of bits) to describe each arm configuration.
On the other hand, as stated in Chapter 2, the existence of such a manifold is totally equivalent to the existence of a correlation between variables $\boldsymbol{\mu}$ and ν

which is definitely easier to be proven. Since this correlation might be multivariate and/or nonlinear, the standard tools of correlation analysis, e.g. the Principal Component Analysis (PCA) or the Pearson's correlation cannot be used. In the following an approach to test the existence of such a correlation is described.

The first step of this analysis is to cluster the task space. Each cluster $\boldsymbol{\mu_{(i)}}$ is a 6-dimensional, $5\,cm \times 5\,cm \times 5\,cm \times 10\deg \times 10\deg \times 10\deg$, hypercube[1]. A possible scenario in which a correlation might exists is shown in Fig. 5.4. When the correlation between $\boldsymbol{\mu}$ and ν is believable, at least in one cluster, the corresponding values of the swivel angle ν are, roughly speaking, "not so different", namely similar. Here the standard deviation s_i has been considered as an

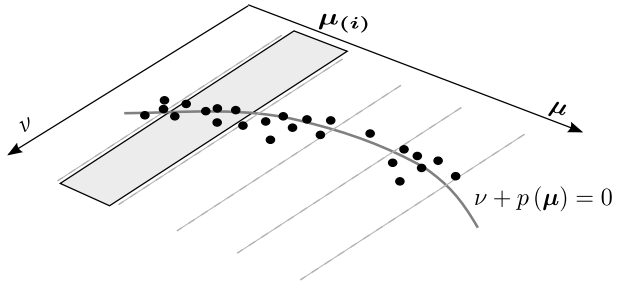

Figure 5.4: *An example of nonlinear correlation between variables $\boldsymbol{\mu}$ and ν, cluster $\boldsymbol{\mu_{(i)}}$ is highlighted*

intra-cluster similarity measure:

$$s_i = \mathbb{S}td\left[\nu_{(i)}\right] \quad \tilde{s}_i = \sqrt{\frac{1}{n_{(i)}-1}\sum\nolimits_{\boldsymbol{\mu_{(i)}}} \left(\nu - \tilde{e}_i\right)^2} \tag{5.2a}$$

$$e_i = \mathbb{E}\left[\nu_{(i)}\right] \quad \tilde{e}_i = \frac{1}{n_{(i)}}\sum\nolimits_{\boldsymbol{\mu_{(i)}}} \nu \tag{5.2b}$$

where $n_{(i)}$ is the number of elements in cluster $\boldsymbol{\mu_{(i)}}$. Its meaning in this context is straightforward: if in a given cluster $\boldsymbol{\mu_{(i)}}$ this value is small enough, a correlation between the hand pose $\boldsymbol{\mu}$ and the swivel angle ν exists, at least locally (i.e. in the considered cluster).
However, in this work we are interested in proving (or disproving) that a *global* (instead of a local) correlation between such variables exists. While for each cluster we were interested in measuring how data were sparsely distributed around their mean value, in order to prove the existence of a global relationship, we need to measure how much the values $\tilde{s}_i \geq 0$ are different from zero. To this end, the

[1] Clusters with less than 10 samples were discarded, see Tab. 5.1.

mean value m_1 (first moment), the square root of the second moment $\sqrt{m_2}$ and the $95th$ percentile p_{95} have been taken into account. The corresponding values computed on the available data are listed in Tab. 5.2. As one can see, all the

Count statistics	Value
Acquired samples	615022
Clusters	20482
Non-empty clusters	10200 (47%)
Samples in non-empty clusters	568317 (92%)

Table 5.1: *Count statistics*

	Value	
Statistic definition	actual	normalized
$m_1 = \mathbb{E}[\tilde{s}_i]$	2.20 deg	1.68%
$\sqrt{m_2} = \sqrt{\mathbb{E}\left[(\tilde{s}_i)^2\right]}$	2.94 deg	2.25%
p_{95}	5.96 deg	4.56%

Table 5.2: *Summary statistics: actual and normalized with respect to the range of variability* $\nu_{max} - \nu_{min}$

computed values are very small. In particular, in the 95% of the clusters, a correlation between the hand pose $\boldsymbol{\mu}$ and the swivel angle ν is very believable. We thus have a clear experimental evidence that a relationship $\nu = -p(\boldsymbol{\mu})$ exists during the motion, where function $p(\cdot)$ might be identified.
Such a relationship can be interpreted as a synergy, see e.g. [15], which actually restricts the space of natural configurations of the human arm to a lower dimensional configuration manifold, i.e. $\sigma(\boldsymbol{q}) = 0 \Leftrightarrow \nu(\boldsymbol{q}) + p(\boldsymbol{\mu}(\boldsymbol{q})) = 0$.

Figure 5.5 shows the intra-cluster variability of the swivel angle. It should be noticed that the values of ν are more likely distributed around the average value, justifying the results in Tab. 5.2. In comparison with other works that make use of a GMR to explain the data distribution, see e.g. [23], [24], [115], and as a further verification of the previous result, Fig. 5.6 shows the estimated variability of the swivel angle in each cluster modelled as a single-Gaussian with an expected value of $\tilde{e}_i$ and variance $\tilde{s}_i^2$, namely

$$\mathcal{P}\left(\nu \mid \boldsymbol{f}(\boldsymbol{q}) \in \boldsymbol{\mu}_{(i)}\right) \sim \mathcal{N}\left(\tilde{e}_i, \tilde{s}_i^2\right) \tag{5.3}$$

Notice that, as a consequence of Proposition 2.1, which guarantees the existence of an equivalent extended Jacobian method for a given function $p(\cdot)$, the

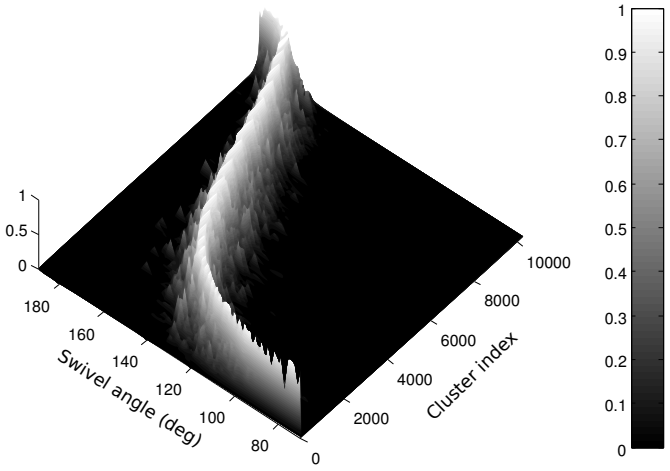

Figure 5.5: *Intra-cluster variability of the swivel angle*

identified relationship confirms the possible explanation of the human arm natural posture by means of a physiologically-based potential energy $u(\boldsymbol{q})$, as discussed in [63], [62] and [61], and briefly described in Chapter 1. Provided that a musculo-skeletal model of the human arm is available, one may extract optimal joint postures from the configuration manifold

$$\sigma(\boldsymbol{q}) = \boldsymbol{N}^T \left(\frac{\partial u}{\partial \boldsymbol{q}}\right)^T = 0 \tag{5.4}$$

where

$$u = \boldsymbol{g}(\boldsymbol{q})^T \left(\boldsymbol{M}(\boldsymbol{q})^T \boldsymbol{W} \boldsymbol{M}(\boldsymbol{q})\right)^{-1} \boldsymbol{g}(\boldsymbol{q}) \tag{5.5}$$

is the cost function introduced in Chapter 1, $\boldsymbol{M}(\boldsymbol{q})$ is the Jacobian of muscle activation, $\boldsymbol{W} = \boldsymbol{W}^T > 0$ is the weight matrix introduced in [61] and $\boldsymbol{g}(\boldsymbol{q})$ is the joint torque due to the gravity. An alternative function $p(\cdot)$ can be subsequently identified, following the approach discussed in detail in the previous Part of this thesis.

Finally, notice that the measured null-space variability, which is confirmed to be small if compared to the variability allowed by joint redundancy (as reported in [44]), might be due to unmodelled dynamics or learning effects during the repetitions.

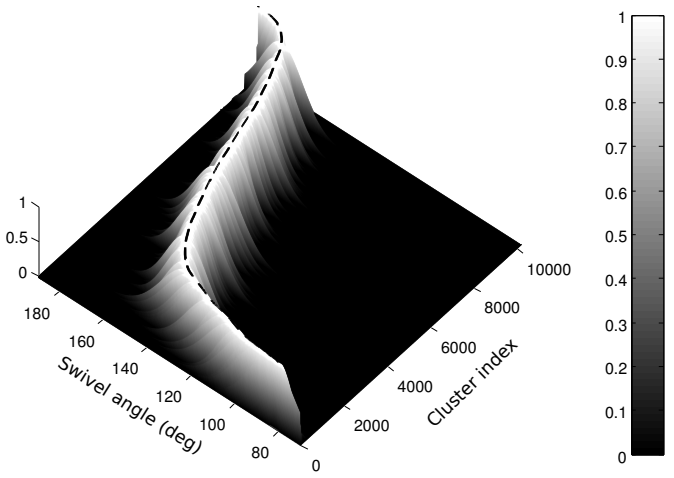

Figure 5.6: *Single-Gaussian model of the intra-cluster variability of the swivel angle*

5.2 Identification of a cyclic redundancy resolution criterion

Based on the statistical evidence of a time-independent correlation between the swivel angle ν and the hand pose $\boldsymbol{\mu}$ during assembly-like movements, in the following an expression for the function $p(\cdot)$ that describes such a relationship will be derived. Since in the 95% of the clusters the mean value of the swivel angle is very representative, clustered values are used to identify the relationship between the task variables $\boldsymbol{\mu}$ and the swivel angle ν, instead of using the entire data set. Moreover, using clustered quantities, acquired data are more uniformly distributed in the task space.
A nonlinear relationship is expected, therefore a pool of nonlinear regressors consisting in a mixture of sine/cosine waves (multivariate truncated Fourier series) and inverse tangent functions has been selected. The identification of the nonlinear relationship between ν and $\boldsymbol{\mu}$ has been then turned into the minimization of a linear-in-parameter cost-function. The greedy algorithm introduced in Chapter 2 has been used to solve the identification problem and to simultaneously reduce the number of regressors needed to obtain an acceptable approximation.
The computed solution of the optimization problem, corresponding to an acceptance threshold (RMS error) of $F_{TH}^{0} = 6\,\mathrm{deg}$, is as follows:

$$\begin{aligned} p(\boldsymbol{\mu}) = & -0.88\cos(\theta + 2.30) - 0.49\cos(\theta + \phi + 2.98) + 0.21\mathrm{atan2}(z, y) \\ & + 0.64\sin(\rho) + 0.50\mathrm{atan2}(y, x) + 0.22\cos(\rho + \theta + \phi) \\ & - 0.47\cos(\phi + 0.60) + 0.15\mathrm{atan2}(z, x) - 0.34\cos(\rho + \phi + 1.07) \\ & + 0.40\cos(\rho + \theta) + 1.39 \end{aligned} \tag{5.6}$$

Function $p(\cdot)$ in (5.6) can be used to predict the value of the swivel angle ν, once the task variables $\boldsymbol{\mu}$ are known.
As a matter of comparison, time histories of acquired and of predicted values of the swivel angle are shown together in Figs. 5.7, 5.8 and 5.9. As one can see, the identified function $p(\cdot)$ correctly predicts the value of the swivel angle for a given (even time-varying) hand pose for every volunteer.

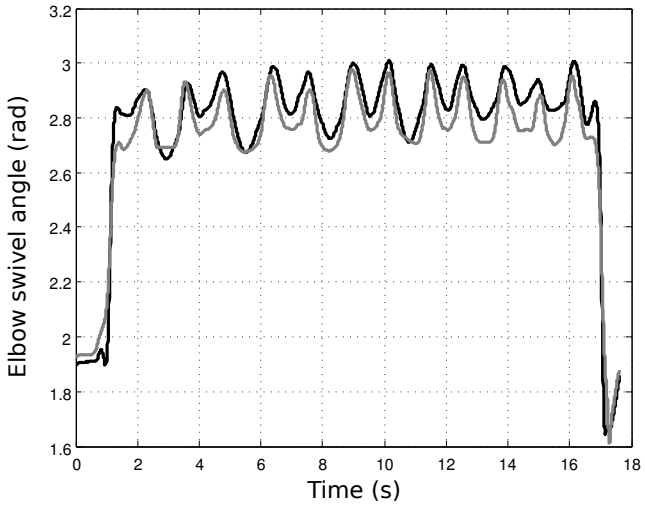

Figure 5.7: *Swivel angle during experiment A(3), volunteer 4: actual (black) and predicted (gray)*

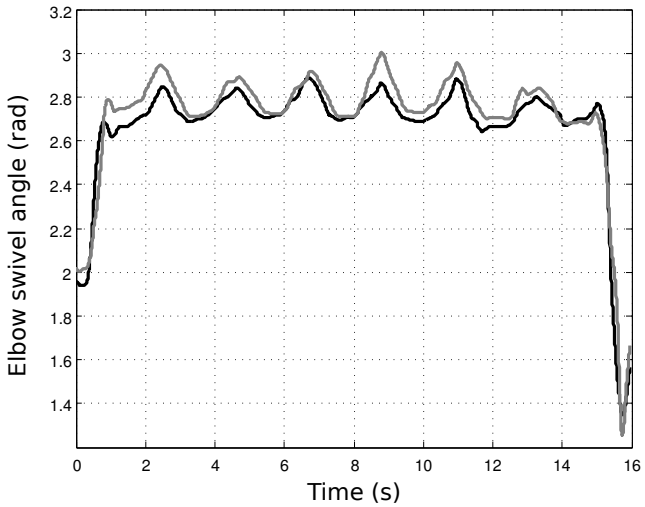

Figure 5.8: *Swivel angle during experiment B(2), volunteer 5: actual (black) and predicted (gray)*

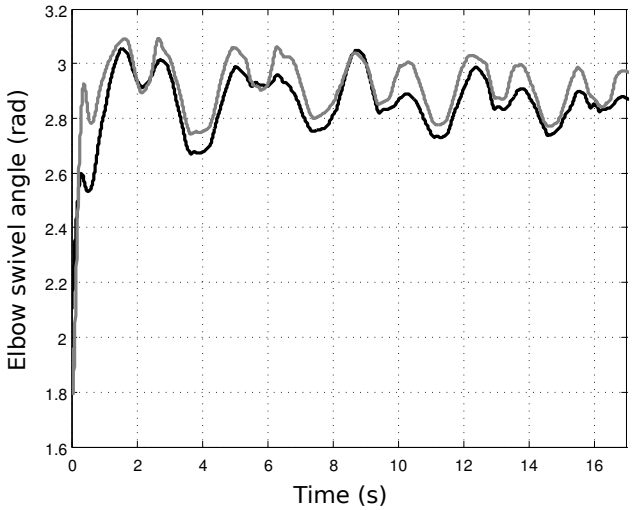

Figure 5.9: *Swivel angle during experiment VA(2), volunteer 8: actual (black) and predicted (gray)*

5.3 Model adaptation to the left arm

The motion capture experiments on the human arm were tackled considering the right arm only. Therefore, the following question arises: how does the correlation identified so far look like for the *left* arm?
The problem concerning how to modify the identified relationship to suit also the left arm was tackled by exploiting the symmetry of the human upper body. However, the mathematical development is a little more involved and deserves a more detailed explanation.
From now on we need to discriminate the position and orientation vector of the right hand

$$\boldsymbol{\mu^R} = \begin{bmatrix} x^R & y^R & z^R & \rho^R & \theta^R & \phi^R \end{bmatrix}^T \tag{5.7}$$

from the corresponding one related to the left hand

$$\boldsymbol{\mu^L} = \begin{bmatrix} x^L & y^L & z^L & \rho^L & \theta^L & \phi^L \end{bmatrix}^T \tag{5.8}$$

as well as the value of the right elbow swivel angle ν^R and similarly ν^L for the left arm. For both the arms the reference frame, centered in the shoulder, is oriented in such a way that the y-axis is pointing forward and the z-axis is vertical and pointing upward. It follows that in order to put the left hand in a position symmetrically equivalent to the right hand, one just needs to enforce the following constraints:

$$x^L = -x^R \quad y^L = y^R \quad z^L = z^R \tag{5.9}$$

As for the Euler angles, some geometrical yet tedious considerations lead to:

$$\rho^L = \pi - \rho^R \quad \theta^L = \theta^R \quad \psi^L = \pi - \psi^R \tag{5.10}$$

Therefore, from (5.9) and (5.10) it follows that one can define a non-singular matrix $\boldsymbol{A}$ and a vector $\boldsymbol{b}$ such that

$$\boldsymbol{\mu^L} = \boldsymbol{A}\boldsymbol{\mu^R} + \boldsymbol{b} \tag{5.11}$$

where

$$\boldsymbol{A} = \begin{bmatrix} -1 & 0 & 0 & 0 & 0 & 0 \\ 0 & 1 & 0 & 0 & 0 & 0 \\ 0 & 0 & 1 & 0 & 0 & 0 \\ 0 & 0 & 0 & -1 & 0 & 0 \\ 0 & 0 & 0 & 0 & 1 & 0 \\ 0 & 0 & 0 & 0 & 0 & -1 \end{bmatrix} \quad \boldsymbol{b} = \begin{bmatrix} 0 \\ 0 \\ 0 \\ \pi \\ 0 \\ \pi \end{bmatrix} \tag{5.12}$$

Given the desired position and orientation for the left hand $\boldsymbol{\mu^L}$, by inverting equation (5.11) one can compute the position and the orientation of the right hand $\boldsymbol{\mu^R}$ and compute the corresponding right swivel angle using (5.6). Then, since the elbow swivel angle for both the arms is defined as the counter-clockwise angular deflection of the plane containing the arm with respect to the vertical plane, it follows that:

$$p^L\left(\boldsymbol{\mu^L}\right) = -p^R\left(\boldsymbol{A^{-1}}\boldsymbol{\mu^L} - \boldsymbol{A}^{-1}\boldsymbol{b}\right) \tag{5.13}$$

where $p^R(\cdot)$ is the function reported in (5.6).

5.4 Summary

In this Chapter a simple relationship between the hand pose (position and orientation) and the elbow swivel angle enforced during the motion of the human arm has been derived. This relation effectively explains the motion of the arm and lends itself to easy application in the kinematic controller of a robotic arm. The existence of such relationship was first proven with statistical methods using a clustering approach and multivariate correlation statistics, and then identified using a least-squares algorithm.

The kinematic constraint between hand position/orientation and swivel angle can now be used as a holonomic redundancy resolution criterion for anthropomorphic industrial manipulators. In particular, the framework for redundancy resolution described in the first Part of this thesis will be exploited for this purpose. Details about the implementation on a real robot prototype as well as the investigation on volunteers about the effect of robot trajectories designed according to the human-centric criterion will be presented in the next Part of this thesis.

Part III

Application to a dual-arm robot prototype

CHAPTER 6

Physiological assessment of the acceptability of robot trajectories

The final objective of this work is to allow the robot to perform a natural execution of a given task by a proper exploitation of the kinematic redundancy. In the previous Chapter, a model describing the natural way humans adopt to resolve arm redundancy has been identified. This Chapter describes the final step needed to achieve a human-like redundancy resolution for robotic manipulators and the experiments performed to assess the corresponding acceptability by human fellow co-workers.

6.1 Implementation of the human-like redundancy resolution criterion

In this Chapter, we will make reference to a dual-arm redundant manipulator prototype called Flexible Robot Industrial Dual Arm (FRIDA), [45], developed by ABB. FRIDA, see Fig. 6.1, is an anthropomorphic robot that aims at closing the gap between a manual assembly and a fully automatic assembly process. This concept robot suits environments involving handling and assembly of small parts in a line where both humans and robots work.

The robot consists of a torso with an integrated controller, two arms (with 7 axes each), and grippers capable of handling a wide range of parts. Each arm has a reach similar to that of a small adult. The weight of the robot is low enough to make it truly portable without mechanical support. All surfaces are designed to be smooth and safe, being covered with soft padding.

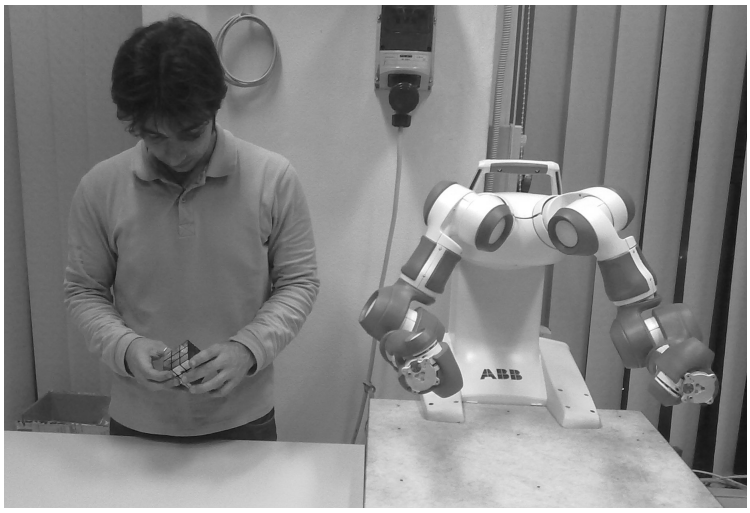

Figure 6.1: ABB *concept robot FRIDA complements human labor*

The motion capture experiments on the human arm described in the previous Chapter were performed without taking care of the robot kinematics and proportions. The following question naturally arises: how can these results be transferred to an arm possibly having different proportions? The answer is however quite straightforward: the only source of difference are the Cartesian variables x, y and z that depend on the human arm length, which might differ from the lengths of the robot arm. However, thanks to a suitable choice of all the regressors in the identified relationship (5.6), the value assigned to ν depends on the ratio between the Cartesian variables only and not on their absolute values. This way, there is no particular issue in applying the identified model to a robot whose dimensions substantially differ from those of the human arm.

For each arm, the controller of FRIDA has an additional input to modify the arm position without affecting the motion of the end-effector. The redundant degree of freedom is directly specified by the programmer through the elbow swivel angle (actually *arm angle* following ABB's terminology), already introduced in this work. The syntax of each motion instruction is as follows:

```
MoveL target, speed, zone, tool;
```

where `target` specifies both position and orientation of the tool and the swivel angle, while `speed` and `zone` are parameters for the path planner, and `tool` specifies the parameters of the tool, if any.
The algorithm for redundancy resolution has been implemented on top of the ABB robot controller without adding any additional hardware. The human-like redundancy resolution criterion has been coded directly in RAPID and the two functions $p^R(\cdot)$ and $p^L(\cdot)$ in (5.6) and (5.13) have been implemented as function calls. Therefore, the redundancy resolution strategy has been implemented by overriding the value of the elbow angle using (5.6) for the right arm

```
MoveL pRight(target), speed, zone, tool;
```

where `pRight( )` is a function that returns the input target modified for the elbow angle as in (5.6). A similar function `pLeft( )` has been defined for the left arm in (5.13).

Figure 6.2 shows a sequence of snapshots of the robot FRIDA while executing pick-and-place and assembly-like motions, adopting a human-like redundancy resolution criterion. It should be noticed that the reported postures look smooth and natural. Figure 6.3 shows the time history of the right and left elbow angles during the task.

A second experiment has been performed involving the coordination of the two arms. In particular, the absolute motion of the right hand has been specified, while the motion of the left hand has been specified with respect to the other hand, in order to maintain a rigid transformation between the two arms and thus to carry an object.
The implementation of the redundancy resolution for the right arm is unchanged and implemented by means of the function `pRight( )`. As for the left arm, a new function `pLeftwrtRight( )` has been introduced. This function takes two arguments: `tLeftwrtRight` which is the desired position and orientation of the left hand with respect to the actual position of the right hand and `tRight` which contains the desired position for the right hand used as an argument for `pRight( )`.
The implementation of `pLeftwrtRight( )` is exactly the same as the one

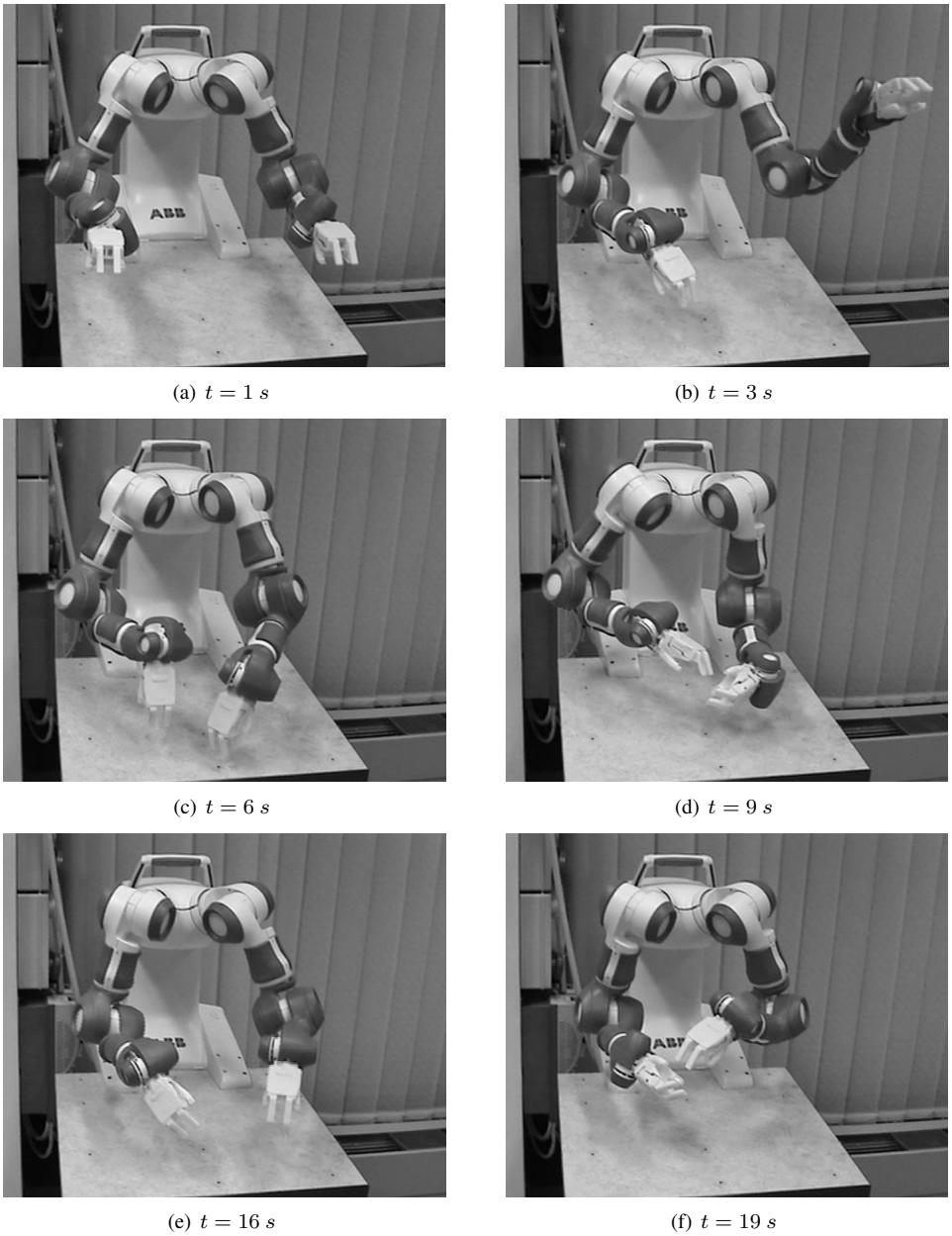

(a) $t = 1\ s$ (b) $t = 3\ s$

(c) $t = 6\ s$ (d) $t = 9\ s$

(e) $t = 16\ s$ (f) $t = 19\ s$

Figure 6.2: *Human-like motion for the prototype robot FRIDA during assembly-like movements*

of `pLeft( )`, apart from an initial instruction to obtain the desired absolute position for the left hand

```
tLeft := PoseMult(tRight,tLeftwrtRight);
```

which simply concatenates the two translations and rotations to compute the absolute target `tLeft` which is used as an input for the function `pLeft( )`.

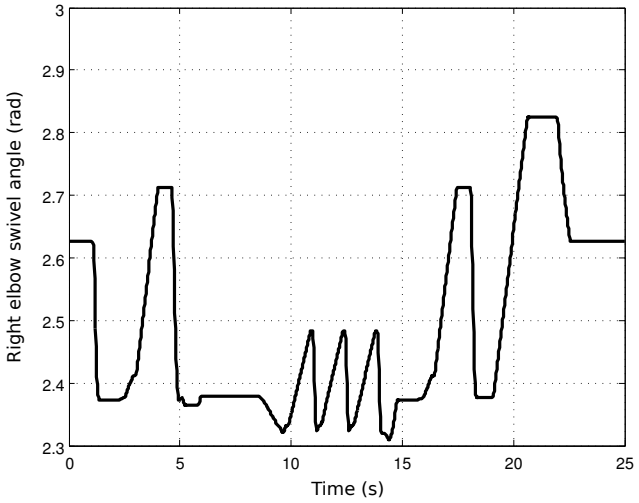

(a) Right elbow swivel angle

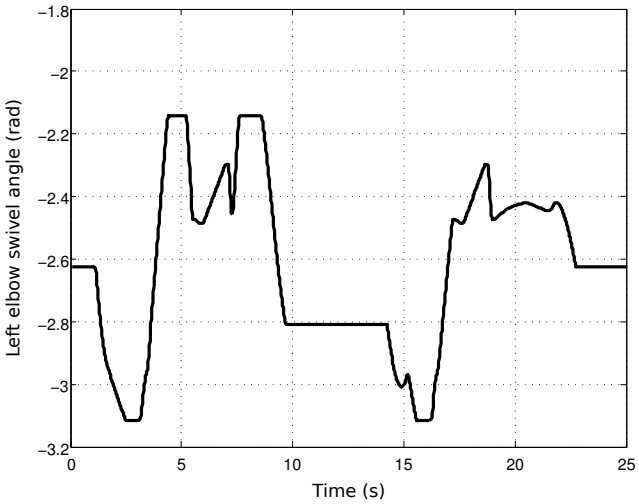

(b) Left elbow swivel angle

Figure 6.3: *Right and left elbow swivel angle during the human-like motion*

Figure 6.4 shows a sequence of snapshots of the prototype robot while executing coordinated movements to carry an object while adopting the human-like

redundancy resolution criterion.

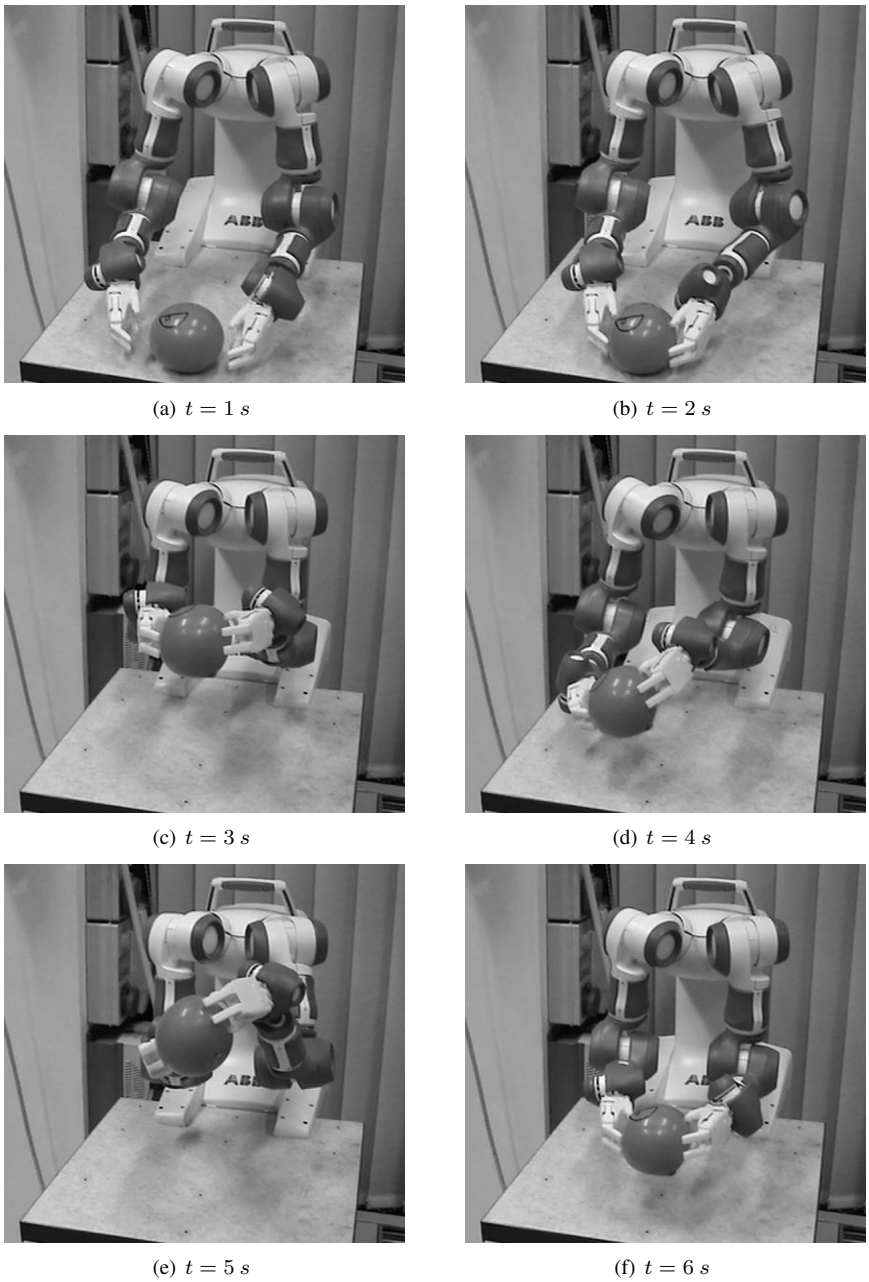

(a) $t = 1\ s$ (b) $t = 2\ s$

(c) $t = 3\ s$ (d) $t = 4\ s$

(e) $t = 5\ s$ (f) $t = 6\ s$

Figure 6.4: *Human-like motion for the prototype robot FRIDA while carrying an object*

6.2 Description of the physiological experiments

Measuring the quality of human-machine interaction is a novel field in robotics research and will be extremely useful for future assessments of all efforts spent in the direction of a more effective HRI. Existing approaches range from the statistical analysis of questionnaires, see e.g. [13], to a more involved affective state estimation from physiological measurements using HMM, as explained in [70], or fuzzy logics, [69], to relate the acquired measurements to the internal affective state.
In order to analyze the physiological reactions of humans to different robot trajectories, an experimental campaign on volunteers has been organized. Following the approach in [68], heart activity, skin conductance and activation of the corrugator muscle have been identified as suitable physiological data for this analysis.

6.2.1 Experimental apparatus

The PROCOMP INFINITI system from THOUGHT TECHNOLOGY was used to acquire the physiological data. The heart muscle activity was measured via Electrocardiography (ECG) measurement using EKG Flex/Pro sensor. The Skin Conductance Response (SCR) was measured using the SCFlex-Pro sensor. The activity of the corrugator muscle was measured with the MyoScan Pro surface Electromyography (EMG) sensor. The sampling frequency was $2048\ Hz$ for the ECG signal and $256\ Hz$ for both the SCR and EMG signals.
Eighteen healthy subjects of age 26.7 ± 4.6 have been selected within master students and the research personnel of Politecnico di Milano. The EMG electrodes were arranged in the abdominal placement and fixed with steucoplastic tape to limit the effects of artifacts. The EMG tripolar electrode has been placed on the frontalis muscle, with the reference electrode on the sagittal plane and the two measurement electrodes to measure the activity on the muscle fibers closest to the robot, just above the eyebrow. The SCR probes have been placed on the first phalanges of the digitus secundus (pointer finger) and of the digitus annularis (ring finger), respectively, of the hand closest to the robot. The overall setup is shown in Fig. 6.5.

6.2.2 Protocol of the experiments

The experiments described in the following aimed at capturing the physiological state of humans working side-by-side with the robot. No physical interaction or cooperation with the robot was expected.
In order to test the physiological response to different robot trajectories, three redundancy resolution criteria have been designed and implemented. The first one

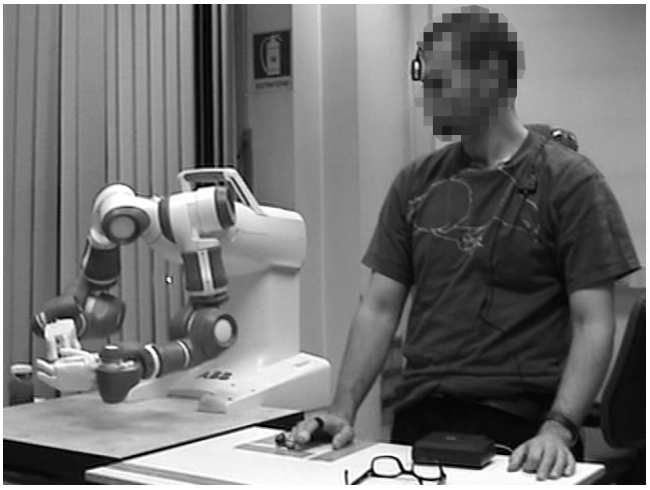

Figure 6.5: *Setup for the physiological experiments*

corresponds to the cyclic human-like (HL) kinematic control strategy described in the previous Sections and identified using the motion capture data as explained in the previous Chapter. The second one (cyclic non human-like, nHL) has been selected in order to enforce a different correlation between the hand pose and the elbow angle. In other words, two functions $p(\cdot)$ differing from (5.6) and (5.13) have been selected. The last one corresponds to a generic non-cyclic (GnC) redundancy resolution criterion which has been designed by assigning (without any specific criterion) the value of the elbow angle to each robot target. Some snapshots of the three motions are compared in Fig. 6.6.

A workspace resembling the one in Fig. 2 has been assembled. The prototype robot FRIDA has been placed in the middle of the table and a working station has been set up next to the robot. The protocol of the experiments is summarized in Tab. 6.1. Notice that each subject experienced the three redundancy resolution methods in different sequence in order to remove the possible effects of prior experiences of the robot motion, which may influence and bias the measurements as pointed out in [12].

Approximately $30\ s$ of physiological data have been acquired before triggering the robot motion, and will be regarded as baseline for subsequent analyses. Then, the assembly-like task and the corresponding redundancy resolution were activated. The robot performed the same task twice for each redundancy resolution criterion with a total duration of approximately $160\ s$.

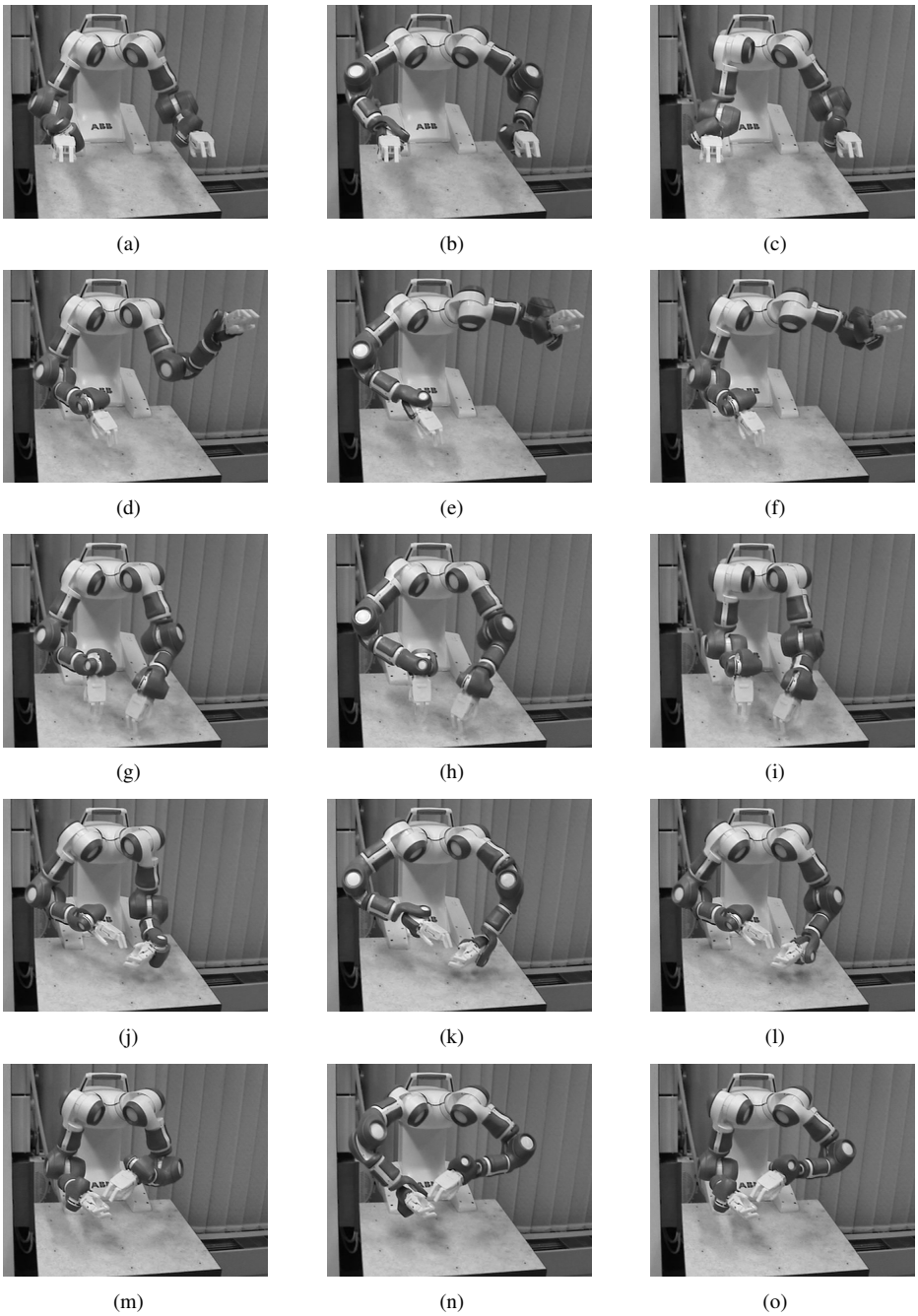

Figure 6.6: *Three redundancy resolutions for the prototype robot (left: HL, center: nHL, right: GnC)*

		Order of the experiments		
Subject	Protocol	First run	Second run	Third run
1	C1	HL	nHL	GnC
2	C2	HL	GnC	nHL
3	C3	nHL	GnC	HL
4	C4	nHL	HL	GnC
5	C5	GnC	HL	nHL
6	C6	GnC	nHL	HL
7	C1	HL	nHL	GnC
⋮	⋮	⋮	⋮	⋮
18	C6	GnC	nHL	HL

Table 6.1: *Order of the physiological experiments*

6.3 Post-processing of the physiological measurements

This Section describes the procedure adopted to extract relevant features from the raw acquired signals. Particular attention was paid to minimize the effect of artifacts, which might invalidate subsequent analyses.

6.3.1 Processing of the ECG signal

In previous studies aimed at measuring the robot-induced stress on humans during coexistence, see e.g. [70], the heart rate and its time derivative, or Heart Rate Variability (HRV) have been analyzed. However, it is widely agreed that their absolute values, especially for the heart rate, are strongly influenced by other factors such as, for instance, physical fitness and posture. In the psychiatric literature, an alternative and well-established tool, based on spectral decomposition, is usually introduced to analyze the ECG information, see [79], [30].
A typical ECG signal, which is shown in Fig. 6.7, consists of a P wave, a QRS complex and a T wave. From raw ECG data, a filter is applied in order to recognize QRS complex and estimate the time instant corresponding to the R peak. Therefore, the output signal is simply a train of pulses, corresponding to the depolarization of the left ventricular, which is responsible of the R peak in the ECG waveform. Then, the time interval between the subsequent R peaks (called RR interval) was measured. The resulting signal is a discrete time one, updated at the end of each RR interval, and is usually called *tachogram*. Spline interpolation has been finally applied to increase the time resolution of the tachogram.
The HRV was then computed using a frequency domain analysis, by means of the estimation of its Power Spectral Density (PSD). Compared with the time domain analysis, the frequency domain analysis of the HRV can reveal a more detailed in-

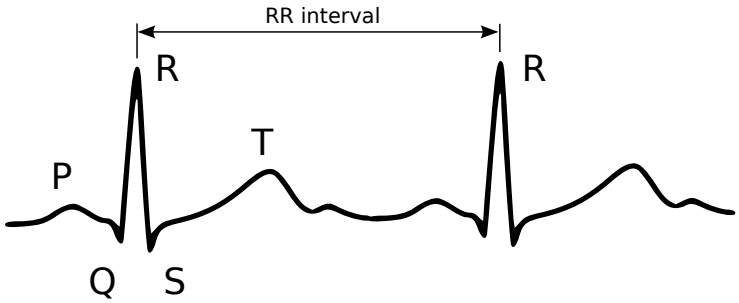

Figure 6.7: *A typical ECG signal*

formation about the ongoing neural activities. In fact, the heart rate is modulated in response to a variety of stimuli by both the parasympathetic and the sympathetic nervous systems. While the former is responsible for a physiological response to normal situations, the latter is more related to reactions to external stimuli producing anxiety, stress and warnings. Several scientists agree on the well-defined frequency separation between the sympathetic- and the parasympathetic-related activities on the HRV PSD, see e.g. [82], [37], [101]. In particular, Low Frequency (LF) of the HRV PSD, approximately in the range $0.04 - 0.15\ Hz$, are related to the sympathetic activities, while the High Frequency (HF) bandwidth, between 0.15 and $0.5\ Hz$, are dominated by the parasympathetic nervous system.

Since the portion of each experiment related to a particular redundancy resolution scheme is very short in time, the tachogram was first re-sampled at $4\ Hz$, and the overall linear trend (corresponding to the Very Low Frequency (VLF) bandwidth $< 0.04\ Hz$) was removed. Then, following modern approaches in the analysis of the HRV signal, see e.g. [27], an Auto Regressive (AR) of order 18 was identified using the well-known Yule-Walker equations, [77]. The PSD of HRV signal has been therefore estimated directly from the AR model coefficients, [4], rather than applying the Fast Fourier Transform (FFT) to the HRV signal. This way a smoother PSD with a higher frequency resolution was obtained. Figure 6.8 shows the frequency domain analysis of the HRV related to one of the experiments.

6.3.2 Processing of the EMG signal

Surface facial electromyography is a non-invasive technique to assess the affective state of individuals subject to external stimuli of different nature, ranging from visual [73] to acoustic [18] ones. More recently, it has been also adopted to analyze the emotional state while playing at computer games, as in [93], or to

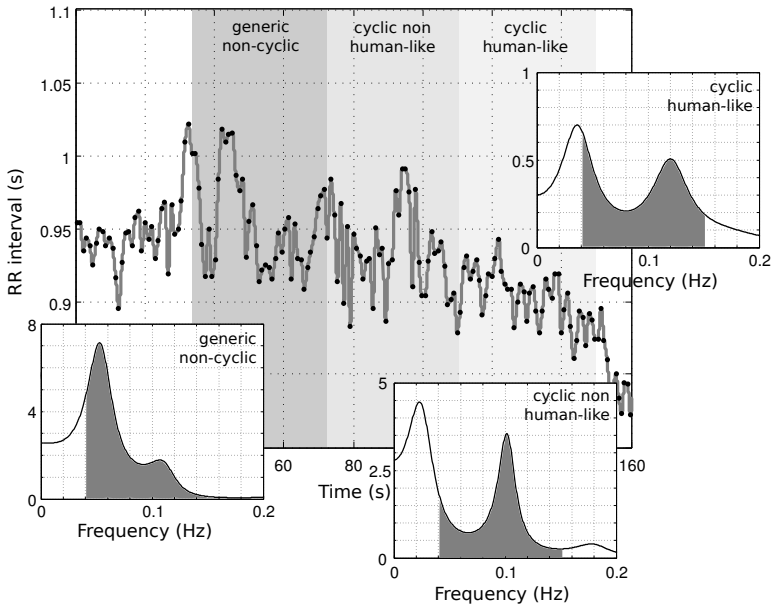

Figure 6.8: *Low frequency component of the HRV PSD (the LF bandwidth is highlighted)*

address the quality of the human-robot interaction, [68].
The analysis of the EMG signal is definitely less involved with respect to the one adopted for the ECG signal, however a variety of different methods exist, ranging from the integrated EMG signal, as explained in [55], to spectral analysis, see e.g. [76].
While most of the methods are related to muscular force estimation, this work is rather focused on stress assessment. For this reason, an accurate estimation of the intensity and of the total duration of each contraction is not considered here.
The analysis of the muscle activity developed in this work is based on the detection of the so-called *onsets* and *offsets*, [46]. An onset is defined as the time interval during which the muscle is contracted, whereas an offset corresponds to a negligible muscle activity. In order to estimate whether the corrugator muscle was contracted (onset) or not (offset) a windowing approach was introduced. It was first noticed that the level of noise measured during the baseline acquisition was significantly lower with respect to the one measured during the actual experiment. Therefore, in order to remove the noise, the median of the entire acquisition was first measured and then removed from the acquired signal. Then, the Inter Quartile Range (IQR) was computed and used as an estimate of the noise amplitude. Finally, a candidate onset was recognized when EMG activity was greater of equal to $2.0\ IQR$ for at least $\Delta t = 40\ ms$. The onset recognition was then confirmed if the maximum level of the EMG signal was greater or equal to 3.0

IQR. The resulting onsets/offsets signal is shown in Fig. 6.9.

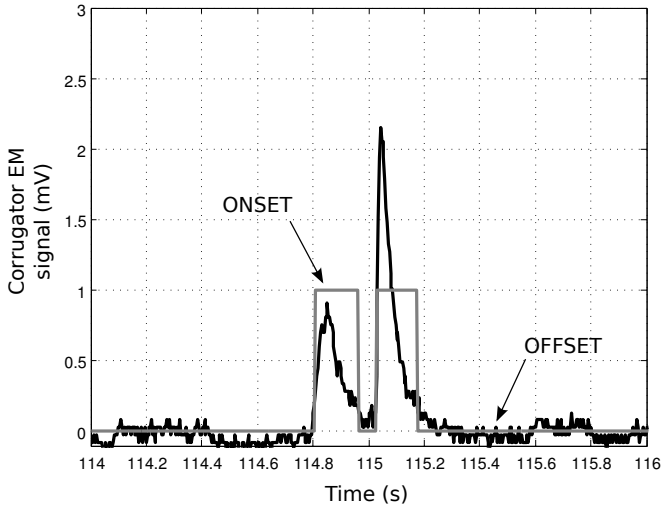

Figure 6.9: *Onsets extraction from RMS-EMG signal*

6.3.3 Processing of the SCR signal

Skin Conductance (SC) is used to infer the sympathetic arousal. The SC signal includes two types of electro-dermal activity: the DC level component and the SCR. The DC level in the SC signal indicates the general activity of the perspiratory glands influenced by body temperature or external temperature, [64], while fluctuations around the average level are due to sweat secretion initiated by distinct bursts of sudomotor nerve activity, which result from the liberation of acetylcholin by the sympathetic nervous system, [17]. For this reason, the measured skin conductance has been first re-sampled at $16\ Hz$ and then filtered with a Butterworth high-pass filer of order 6 with a cut-off frequency[1] of $0.04\ Hz$.

6.4 Physiological assessment of the HRI

In the following, the final analysis of the post-processed experimental data is reported. In particular, the definition of statistics aimed at quantifying the robot-induced stress is explained.
For the ECG signal, a common way to assess the dominance of the sympathetic nervous system with respect to the parasympathetic one, is to measure the ratio between the power associated to the two corresponding bands of frequency.

[1] Notice that the value $0.04\ Hz$ is the same used for the VLF/LF separation in the HRV analysis.

As reported in [82], such a value is significantly higher when the subject is experiencing emotions with a negative valence (anger), while being substantially unchanged, with respect to the baseline, when the subject experiences emotions with a positive valence (appreciation). Therefore, the following statistics can be taken into account as an indicator of the overall physiological acceptability of robot trajectories:

$$s_{ECG}^{i,RR} = \frac{LF^{i,RR}}{HF^{i,RR}} \tag{6.1}$$

where

$$\begin{aligned} LF^{i,RR} &= \int_{0.04Hz}^{0.15Hz} PSD^{i,RR}(f)\, df \\ HF^{i,RR} &= \int_{0.15Hz}^{\infty} PSD^{i,RR}(f)\, df \end{aligned} \tag{6.2}$$

meaning that the lower the value of the statistics, the higher the comfort of volunteer $i = 1, \ldots, 18$ was, while working next to the robot which implemented the redundancy resolution $RR \in \{HL, nHL, GnC\}$.
EMG activity of the corrugator muscle, and more generally of facial muscles, has been extensively exploited in the literature, as being highly correlated with emotions with a negative valence, see e.g. [19]. Therefore, the number of contractions per minute, regardless their duration and intensity, was counted:

$$s_{EMG}^{i,RR} = \frac{60}{t_f^{i,RR} - t_0^{i,RR}} \int_{t_0^{i,RR}}^{t_f^{i,RR}} edge\left(onsets^{i,RR}(t)\right) dt \tag{6.3}$$

where $edge(\cdot)$ is a function returning a unit Dirac pulse corresponding to rising edges of the input.
As for the skin conductance, which is positively correlated with the arousal [72], [19] or [53], the following statistics has been considered:

$$s_{SCR}^{i,RR} = \frac{1}{t_f^{i,RR} - t_0^{i,RR}} \int_{t_0^{i,RR}}^{t_f^{i,RR}} \left(SCR_{HighPass}^{i,RR}(t)\right)^2 dt \tag{6.4}$$

which, apart from some scaling factor, corresponds from Parseval's theorem to the integrated PSD of the SCR over the frequency range $[0.04Hz, \infty)$. The meaning of this statistics is straightforward: the lower value corresponds to a lower arousal.

As already mentioned, the values of these statistics might depend on the order in which the three different robot trajectories are experienced by the volunteer.

As shown in Tab. 6.1, the availability of eighteen volunteers could help in circumvent this problem. In fact every possible sequence of motions has been tested by three volunteers and this mitigates the effect of possible biases and trends during the sequence each volunteer experienced.
Since the final objective of this investigation is to measure differences in the physiological state of subjects, rather than measuring the absolute value of their affective state, the given statistics have been normalized. Figures 6.10 and 6.11

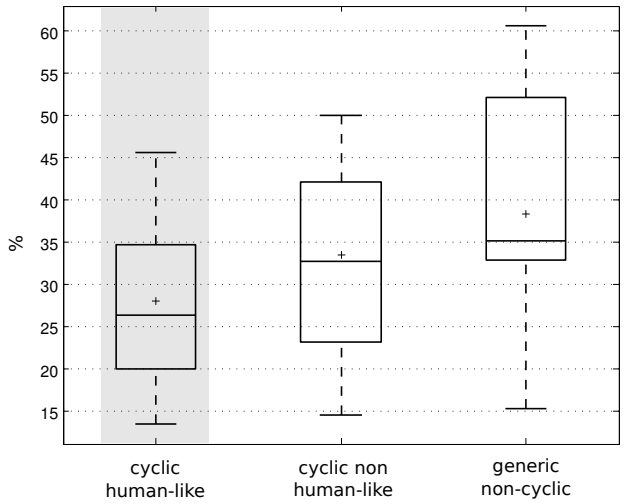

Figure 6.10: *Boxplot of the normalized ECG statistics*

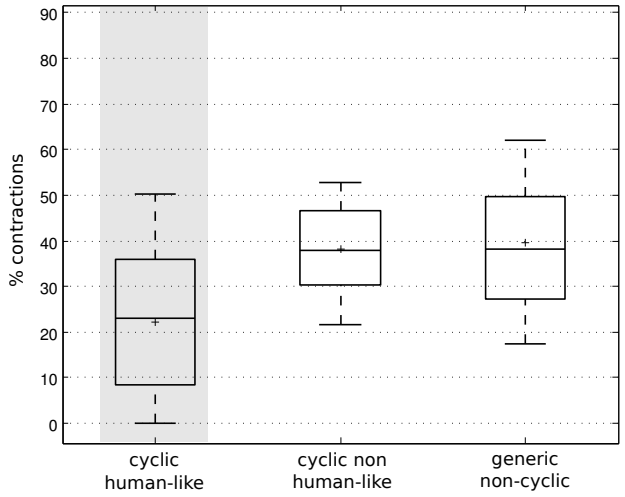

Figure 6.11: *Boxplot of the normalized EMG statistics*

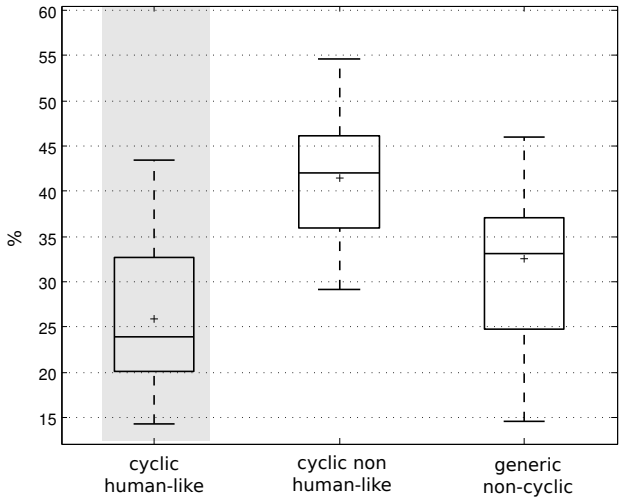

Figure 6.12: *Boxplot of the normalized SCR statistics*

report the boxplots[2] of the normalized ECG and EMG statistics, respectively, while Fig. 6.12 shows the boxplot for the normalized SCR statistics. As already stated, ECG and EMG statistics are negatively correlated with the valence, while the SCR statistics is positively correlated with the arousal.
At first glance, the ECG and the EMG statistics agree in predicting a clear trend in the valence, meaning that the more negative valence corresponds with the lower degree of human-likeness. Therefore, the human-like motion generally induces a lower level of stress, with respect to both the cyclic non human-like and the generic non-cyclic motions. Moreover, the non-cyclic motion seems to even increase the stress perceived by the volunteers.
In order to obtain a more rigorous verification of this conjecture, the Page's L-test[3] was computed for both the ECG and the EMG statistics. The visible trend on the acquired data has been found to be statistically significant[4] for both the ECG ($p < 0.05$) and the EMG signals ($p \approx 0.05$).
The SCR statistics, which is positively correlated with the arousal, deserves a more detailed discussion. As one can see from Fig. 6.12, the arousal state does not exhibit the same trend which was statistically consistent for both the ECG and the EMG statistics. The only reasonable hypothesis to test is that the arousal

[2]Boxplots are a graphical way to represent grouped data. They report the three quartiles as solid lines, the so called whiskers which quantify the dispersion of the data and the mean value, see [14].

[3]The Page's L-test is a non parametric ranking-based statistical trend test aimed at verifying the hypothesis of trends between grouped variables (for more details see [91]). More precisely, the test considers the null hypothesis that, for k groups, the corresponding statistics are such that $s_1 = s_2 = s_3 = \cdots = s_k$ against the alternative hypothesis that $s_1 < s_2 < s_3 < \cdots < s_k$.

[4]In statistics, the p-value is the minimum value of the significance level $1 - \alpha$ that leads to reject the null-hypothesis. Practically speaking, the lower the p-value is, the more confident the acceptance of the alternative hypothesis is.

is greater corresponding to the nHL motion with respect to the HL motion. For this the Wilcoxon signed-rank test (suitable to test the trend hypothesis between data organized in two groups) has been performed, confirming the hypothesis ($p < 0.001$).
For a different analysis, we introduce a different ordering of the three robot trajectories by defining the average elbow elevation statistics:

$$s_{elbow}^{i,RR} = \frac{1}{t_f^{i,RR} - t_0^{i,RR}} \int_{t_0^{i,RR}}^{t_f^{i,RR}} z_{elbow}^{i,RR}(t)\, dt \tag{6.5}$$

where $z_{elbow}^{i,RR}$ represents the instantaneous elevation of the elbow during the experiment. The resulting boxplot corresponding to the alternative order of the three motions is shown in Fig. 6.13. At first glance, a positive trend of the arousal state

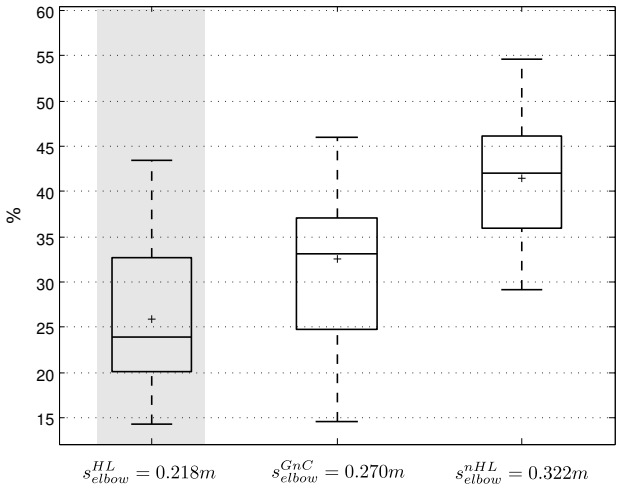

Figure 6.13: *Boxplot of the normalized SCR statistics corresponding to the alternative ordering of robot trajectories based on the average elbow elevation*

with respect to the average elbow elevation can be reported. The corresponding Page's L-test confirmed the hypothesis ($p = 0.05$).

6.5 Summary

This Chapter described the implementation of the human-like redundancy resolution, described in the previous Part of this thesis, on a 14-DOF prototype robot. In order to assess the physiological comfort/discomfort perceived by humans working side-by-side with the robot, an experimental campaign has been organized. For comparison, two alternative redundancy resolution strategies have

been implemented: a non-human like, yet cyclic, one and one corresponding to a generic non-cyclic kinematic control strategy. During the experiments valence and arousal of subjects have been indirectly estimated using electrocardiographic/electromyographic signals and skin conductance, respectively.
The non-human like motion induced a more negative valence with respect to the human-like one. Moreover, a non-cyclic motion was responsible of a more negative valence with respect to both the two cyclic kinematic control strategies (human- and non human-like).
A different classification of the three robot trajectories, based on the average elevation of the elbow, has been adopted to analyze the arousal of the subjects. It was shown that increased elbow elevations induced higher levels of arousal.
The human-like redundancy resolution strategy developed in this thesis, characterized by lower elbow elevations, induced a quantified reduction of the emotional arousal and was responsible for less negative valences. For these reasons, it could be adopted to effectively reduce the robot-induced stress in human fellow co-workers.

Conclusions

This thesis tries to take a step forward in the use of different emerging robotic technologies: kinematic redundancy and safe human-robot interaction. While robot manufacturers are commercializing redundant manipulators, HRI is becoming an important issue also in the industrial context. New production paradigms require that humans and robots coexist in the same workspace and also cooperate to some extent.

In Part I of this thesis a newly conceived method to enforce arbitrary cyclic kinematic control strategies on top of industrial controllers has been presented. The most important features of this methodology are:

- proof of completeness of the approach, namely the direct one-to-one matching with the extended Jacobian method, and in particular the possibility to enforce any holonomic constraint;
- the user-oriented fashion which allows the robotic programmer to tune the redundancy resolution criterion depending on the specific application;
- the convenience for the robotic manufacturer who is free to implement a specific inverse kinematic algorithm in advance, allowing the customization of redundancy resolution criterion;
- the possibility to enforce different criteria ranging from kineto-static to dynamic optimization requirements;
- the effectiveness in solving the kinematic redundancy in some practical applications.

In Part II motion capture experiments performed on volunteers to investigate how humans resolve arm redundancy are described. A methodology based on Kalman Filtering techniques has been adopted to estimate joint positions from marker measurements. It has been then shown that an identifiable holonomic constraint explains how redundancy is exploited in human arms. This relationship has been derived in closed form using a nonlinear regression technique and validated against experimental data.

Finally, in Part III the human-like redundancy resolution has been implemented in the robotic controller for a 14-DOF anthropomorphic industrial manipulator using the framework developed in Part I. Experiments have shown that the resulting motion appeared more natural compared with other redundancy resolution criterion. The outcome of physiological experiments showed that the human-like redundancy resolution strategy developed in this thesis can be adopted to effectively reduce the robot-induced stress in humans working side-by-side with robots.

Future research directions

The framework for redundancy resolution developed in this thesis has been largely tested in industrial situations to solve the inverse kinematic problem, even in the case of multiple degrees of redundancy. It has been finally applied to a 14-DOF anthropomorphic prototype robot mounted on a fixed stand to achieve a human-like execution of a generic manipulation task.

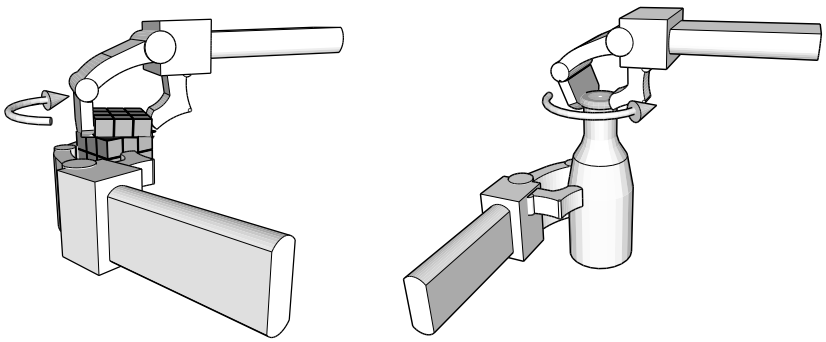

(a) Solving the Rubik cube (b) Opening a bottle

Figure 7.1: *Examples of bimanual manipulation, adapted from [3]*

A natural development of this work could be to apply the proposed techniques to full humanoid robots, possibly equipped with additional DOF, e.g. a mov-

able torso, legs or wheels. In particular, it would be interesting to investigate on the way humans exploit the redundancy during bimanual manipulation tasks, as sketched in Fig. 7.1.
Differently from the case analyzed in this work, the swivel angle is not sufficient to describe the available degrees of redundancy in tasks like solving the Rubik cube, see Fig. 7.1(a), or unscrewing a bottle top, as in Fig. 7.1(b). In fact, when performed with a dual-arm robot (having 14 DOF or more) the former requires 6 DOF only (to describe the relative displacements of the two hands), while for the latter only 8 DOF (6 as in the previous case and 2 additional ones to maintain the bottle aligned with vertical direction) are necessary.

Glossary

A

AR Auto Regressive. 101

C

C7 7th cervical vertebra. 68, 75

CLIK Closed-Loop Inverse Kinematics. 20, 24, 25, 29, 36

D

DOF Degree(s) of Freedom. III, VII, IX, X, 5, 6, 12, 38, 41, 42, 45, 55, 74, 107, 112, 113

E

ECG Electrocardiography. 97, 100, 102, 103, 106

EKS Extended Kalman Smoother. 75, 76, 79

EMG Electromyography. 97, 102, 104, 106

F

FFT Fast Fourier Transform. 101

FRIDA Flexible Robot Industrial Dual Arm. 91–93, 98

G

GHJ Gleno-Humeral Joint. 71, 75

GMR Gaussian Mixture Regression. 14, 83

H

HF High Frequency. 101
HMM Hidden Markov Models. 14, 97
HRI Human-Robot Interaction. 11, 15, 16, 97
HRV Heart Rate Variability. 100, 101, 103

I

IJ incisura jugularis. 68, 75
IQR Inter Quartile Range. 102

L

LF Low Frequency. 101, 103

M

MCMC Markov Chain Monte Carlo. 126

P

PCA Principal Component Analysis. 82
PSD Power Spectral Density. 100, 101, 104

R

RMS Root Mean Square. 58, 85
RULA Rapid Upper Limb Assessment. 14

S

SC Skin Conductance. 103
SCR Skin Conductance Response. 97, 103, 104, 106
SVD Singular Value Decomposition. 4

T

TCP Tool Center Point. 35, 38, 39, 42, 47, 56, 57

V

VLF Very Low Frequency. 101, 103

Bibliography

[1] ISO-14738:2002: Safety of machinery - anthropometric requirements for the design of workstations at machinery, 2002.

[2] DIN-33402-2: Ergonomics - human body dimensions - part 2: Values, 2005.

[3] B. V. Adorno. *Two-arm Manipulation: From Manipulators to Enhanced Human-Robot Collaboration*. PhD thesis, Université Montpellier II, 2011.

[4] H. Akaike. Power spectrum estimation through autoregressive model fitting. *Annals of the Institute of Statistical Mathematics*, 21:407–419, 1969.

[5] C. Alford and S. Belyeu. Coordinated control of two robot arms. In *IEEE Conference on Robotics and Automation, ICRA*, pages 468–473, 1984.

[6] G. Alici and R. W. Daniel. Robotic drilling under force control: Execution of a task. In *IEEE/RSJ International Conference on Intelligent Robots and Systems, IROS*, pages 1618–1625, 1994.

[7] J. K. Antonio, R. Ramabhadran, and T. L. Ling. A framework for optimal trajectory planning for automated spray coating. *International Journal on Robotics and Automation*, 12:124–134, 1997.

[8] C. G. Atkeson, C. H. An, and J. M. Hollerbach. Estimation of inertial parameters of manipulators loads and links. *International Journal of Robotics Research*, 5(3):101–119, 1986.

[9] K. Ayusawa, G. Venture, and Y. Nakamura. Real-time implementation of physically consistent identification of human body segments. In *IEEE Conference on Robotics and Automation, ICRA*, 2011.

[10] J. Baillieul. Kinematic programming alternatives for redundant manipulators. In *IEEE International Conference on Robotics and Automation, ICRA*, pages 722–728, 1985.

[11] J. Baillieul, J. Hollerbach, and R. Brockett. Programming and control of kinematically redundant manipulators. In *IEEE Conference on Decision and Control, CDC*, 1984.

[12] C. Bartneck, D. Kulic, and E. Croft. Measuring the anthropomorphism, animacy, likeability, perceived intelligence, and perceived safety of robots. In *Metrics for Human-Robot Interaction Workshop in conjunction with the International Conference on Human Robot Interaction, HRI*, pages 37–44, 2008.

[13] C. Bartneck, D. Kulic, E. Croft, and S. Zoghbi. Measurement instruments for the anthropomorphism, animacy, likeability, perceived intelligence, and perceived safety of robots. *International Journal of Social Robot*, pages 71–81, 2009.

[14] Y. Benjamini. Opening the box of a boxplot. *The American Statistician*, 42:257–262, 1988.

[15] N. Bernstein. *The coordination and regulation of movement*. Pergamon, New York, 1967.

[16] A. Blomdell, G. Bolmsjö, T. Brogårdh, P. Cederberg, M. Isaksson, R. Johansson, M. Haage, K. Nilsson, M. Olsson, T. Olsson, A. Robertsson, and J. Wang. Extending an industrial robot controller - implementation and applications of a fast open sensor interface. *IEEE Robotics and Automation Magazine*, 12:85–94, 2005.

[17] W. Boucsein. *Electrodermal Activity*. Springer, Berlin, 1992.

[18] M. M. Bradley and P. J. Lang. Affective reactions to acoustic stimuli. *Psychophysiology*, 37(2):204–215, 2000.

[19] M. M. Bradley and P. J. Lang. Measuring emotion: behavior, feeling, and physiology. In Richard D. Lane, Lynn Nadel, and Geoffrey Ahern, editors, *Cognitive neuroscience of emotion*, pages 242–276. Oxford University Press, 2000.

[20] F. Caccavale, P. Chiacchio, and S. Chiaverini. Task-space regulation of cooperative manipulators. *Automatica*, pages 879–887, 2000.

[21] F. Caccavale, S. Chiaverini, C. Natale, B. Siciliano, and L. Villani. Geometrically consistent impedance control for dual-robot manipulation. In *IEEE Conference on Robotics and Automation, ICRA*, volume 4, pages 3873–3878, 2000.

[22] F. Caccavale and M. Uchiyama. Cooperative manipulators. In *Handbook of robotics*, pages 701–718. Springer, 2008.

[23] S. Calinon, F. D'halluin, Sauser E. L., D. G. Caldwell, and A. G. Billard. Learning and reproduction of gestures by imitation. *IEEE Robotics Automation Magazine*, 17(2):44 –54, 2010.

[24] S. Calinon, I. Sardellitti, and D. G. Caldwell. Learning-based control strategy for safe human-robot interaction exploiting task and robot redundancies. In *IEEE/RSJ International Conference on Intelligent Robots and Systems, IROS*, pages 249–254, 2010.

[25] A. C. Campbell, D. G. Lloyd, J. A. Alderson, and B. C. Elliot. MRI development and validation of two new predictive method of glenohumeral joint centre location identification and comparison with estabilished techniques. *Journal of Biomechanics*, 42:1527–1532, 2009.

[26] C. Cantelmo and L. Piroddi. Adaptive model selection for polynomial narx models. *Control Theory Applications, IET*, 4(12):2693–2706, 2010.

[27] J. L. A. Carvalho, A. F. Rocha, I. Dos Santos, Junqueira L. F. Itiki, C., and F. A. O. Nascimento. Study on the optimal order for the auto-regressive time-frequency analysis of heart rate variability. In *Annual International Conference of the IEEE Engineering in Medicine and Biology*, volume 3, pages 2621–2624, 2003.

[28] M. Chen and B. Schmeiser. General hit-and-run Monte Carlo sampling for evaluating multidimensional integrals. *Operative Research Letters*, pages 161–169, 1996.

[29] P. Chiacchio, S. Chiaverini, and B. Siciliano. Direct and inverse kinematics for coordinated motion tasks of a two-manipulator system. *ASME Journal of Dynamics, Systems, Measurements, and Control*, 118:691–697, 1996.

[30] H. Cohen, M. A. Matar, Z. Kaplan, and M. Kotler. Power spectral analysis of heart rate variability in psychiatry. *Psychotherapy and Psychosomatics*, 68(2):59–66, 1999.

[31] J. J. Craig. *Introduction to Robotics: Mechanics and Control*. Prentice Hall, 2005.

[32] F. De Groote, T. De Laet, I. Jonkers, and J. De Schutter. Kalman smoothing improves the estimation of joint kinematics and kinetics in marker-based human gait analysis. *Journal of Biomechanics*, 41:3390–3398, 2008.

[33] A. De Luca. Dynamic control of robots with joint elasticity. In *IEEE International Conference on Robotics and Automation, ICRA*, 1988.

[34] A. De Luca, L. Lanari, and G. Oriolo. Control of redundant robots on cyclic trajectories. In *IEEE International Conference on Robotics and Automation, ICRA*, 1992.

[35] A. De Luca and G. Oriolo. Nonholonomic behavior in redundant robots under kinematic control. *IEEE Transactions on Robotics and Automation*, 13(5):776–782, 1997.

[36] A. De Santis, B. Siciliano, A. De Luca, and A. Bicchi. An atlas of physical human-robot interaction. *Mechanism and Machine Theory*, 43(3):253–270, 2008.

[37] J. P. A. Delaney and D. A. Brodie. Effects of short-term psychological stress on the time and frequency domains of heart-rate variability. *Perceptual and Motor Skills*, 91(2):515–524, 2000.

[38] D. Domkin, J. Laczko, M. Djupsjobacka, S. Jaric, and M. L. Latash. Joint angle variability in 3D bimanual pointing: uncontrolled manifold analysis. *Experimental Brain Research*, 163:44–57, 2005.

[39] O. Egeland. Task-space tracking with redundant manipulators. *IEEE Journal on Robotics and Automation*, 1:471–475, 1987.

[40] G. Ferretti, C. Maffezzoni, G. Magnani, and P. Rocco. Joint stiffness estimation based on force sensor measurements in industrial manipulators. *ASME Journal of Dynamic Systems, Measurements and Control*, 116(1):163–167, 1994.

[41] G. Ferretti, G. Magnani, and P. Rocco. Assigning virtual tool dynamics to an industrial robot through an admittance controller. In *International Conference on Advance Robotics, ICAR*, pages 1–6, 2009.

[42] T. Flash, N. Hogan, and E. Bizzi. The coordination of arm movements: an experimentally confirmed mathematical model. *The Journal of Neuroscience*, 5:1688–1703, 1985.

[43] A. A. Goldenberg and D. L. Lawrence. A generalized solution to the inverse kinematic of robot manipulators. *ASME Journal of Dynamic Systems, Measurements, and Control*, 107:103–106, 1985.

[44] H. Grea, M. Desmurget, and C. Prablanc. Postural invariance in three-dimenstional reaching and grasping movements. *Experimental Brain Research*, 134:155–162, 2000.

[45] E. Guizzo. ABB's FRIDA offers glimpse of future factory robots. IEEE Spectrum, `http://spectrum.ieee.org/`, 2011.

[46] P. W. Hodges and B. H. Bui. A comparison of computer-based methods for the determination of onset of muscle contraction using electromyography. *Electroencephalography and Clinical Neurophysiology - Electromyography and Motor Control*, 101(6):511–519, 1996.

[47] N. Hogan. An organizing principle for a class of voluntary movements. *Journal of Neuroscience*, 11:2745–2754, 1984.

[48] N. Hogan. Impedance control - an approach to manipulation, part I-III. *ASME Journal of Dynamic Systems and Measurements and Control*, 107:1–24, 1985.

[49] P. Hsu. Coordinated control of multiple manipulator systems. *IEEE Transactions on Robotics and Automation*, 9(4):400–410, August 1993.

[50] P. Hsu, J. Hauser, and S. Sastry. Dynamic control of redundant manipulators. In *IEEE International Conference on Robotics and Automation, ICRA*, pages 183–187, 1988.

[51] D. Huybrechs and S. Olver. Rapid function approximation by modified Fourier series. *Highly Oscillatory Problems*, pages 51–71, 2009.

[52] A. Isidori. *Nonlinear Control Systems*. Springer, 1995.

[53] S. C. Jacobs, R. Friedman, J. D. Parker, G. H. Tofler, A. H. Jimenez, J. E. Muller, H. Benson, and P. H. Stone. Use of skin conductance changes during mental stress testing as an index of autonomic arousal in cardiovascular research. *American Heart Journal*, 128(6):1170–1176, 1994.

[54] R. Johansson, P. Fransson, and M. Magnusson. Optimal coordination and control of posture and movements. *Journal of Physiology - Paris*, 103(3):159–177, 2009.

[55] M. Jorge and M. L. Hull. Analysis of EMG measurements during bicycle pedalling. *Journal of Biomechanics*, 19(9):683–694, 1986.

[56] S. Jung, T. C. Hsia, and R. G. Bonitz. Force tracking impedance control of robot manipulators under unknown environments. *IEEE Transactions on Control System Technology*, 12:474–483, 2004.

[57] T. Kang, J. He, and S. I. Helms-Tillery. Determining natural arm configuration along a reaching trajectory. *Experimental Brain Research*, 167:352–361, 2005.

[58] T. Kang, Y. Shimansky, and J. He. Angle of elbow elevation depends on the reach target coordinates. In *IEEE Engineering in Medicine and Biology and Annual Conference and the Annual Fall Meeting of the Biomedical Engineering Society joint Conference, EMBS/BMES*, 2002.

[59] S. Kawaji, M. Arao, and Y. Chen. Thrust force control of drilling system using neural network. In *IEEE/ASME International Conference on Advance Intelligence Mechatronics, AIM*, pages 476–481, 2001.

[60] O. Khatib. Unified approach for motion and force control of robot manipulators: The operational space formulation. *IEEE Journal of Robotics and Automation*, 3:43–53, 1987.

[61] O. Khatib, E. Demicran, V. De Sapio, L. Sentis, T. Besier, and S. Delp. Robotics-based synthesis of the human motion. *Journal of Physiology - Paris*, 103:211–219, 2009.

[62] O. Khatib, L. Sentis, and J. Park. *A Unified Framework for Whole-Body Humanoid Robot Control With Multiple Constraints and Contacts*, pages 303–312. Springer Tracts in Advanced Robotics - STAR Series, European Robotics Symposium (EURON), 2008.

[63] O. Khatib, J. Warren, V. De Sapio, and L. Sentis. Human-like motion from physiologically-based potential energies. In J. Lenarčič and C. Galletti, editors, *On Advances in Robot Kinematics*, pages 149–163. Kluwer Academic Publishers, 2004.

[64] J. Kim and E. Ande. Emotion recognition based on physiological changes in music listening. *IEEE Transactions on Pattern Analysis and Machine Intelligence*, 30(12):2067–2083, 2008.

[65] S. Kim, C. Kim, and J. H. Park. Human-like arm motion generation for humanoid robots using motion capture database. In *IEEE/RSJ International Conference on Intelligent Robots and Systems, IROS*, pages 3486–3491, 2006.

[66] C. A. Klein and C. H. Huang. Review of pseudoinverse control for use with kinematically redundant manipulators. *IEEE Transactions on Systems, Man, and Cybernetics*, 13(3):245–250, 1983.

[67] K. Kreutz-Delgado, M. Long, and H. Seraji. Kinematic analysis of 7 DOF anthropomorphic arms. In *IEEE International Conference on Robotics and Automation, ICRA*, 1990.

[68] D. Kulic. *Safety for Human-Robot Interaction*. PhD thesis, University of British Columbia, 2005.

[69] D. Kulic and E. Croft. Physiological and subjective responses to articulated robot motion. *Robotica*, 25:13–27, 2007.

[70] D. Kulic and E. A. Croft. Affective state estimation for human-robot interaction. *IEEE Transactions on Robotics*, 23(5):991–1000, 2007.

[71] J. Kwon and F. C. Park. Natural movement generation using Hidden Markov Models and principal components. *IEEE Transactions on Systems, Man, and Cybernetics*, 38(5):1184–1194, 2008.

[72] P. J. Lang. The emotion probe: Studies of motivation and attention. *American Psychologist*, 50:372–372, 1995.

[73] P. J. Lang, M. K. Greenwald, M. M. Bradley, and A. O. Hamm. Looking at pictures: Affective, facial, visceral, and behavioral reactions. *Psychophysiology*, 30(3):261–273, 1993.

[74] S. Lee and J. M. Lee. Task-oriented dual-arm manipulability and its application to configuration optimization. In *IEEE Conference on Decision and Control, CDC*, pages 2253–2260, 1988.

[75] A. Liegeois. Automatic supervisory control of the configuration and behavior of multibody mechanisms. *IEEE Transactions on Systems, Man and Cybernetics*, 7:868–871, 1977.

[76] L. Lindstrom, R. Magnusson, and I. Petersen. Muscular fatigue and action potential conduction velocity changes studied with frequency analysis of EMG signals. *Electromyography*, 10(4):341–356, 1970.

[77] L. Ljung. *System Identification - Theory For the User*. Prentice Hall, 1999.

[78] Z. Lv, Y. Li, and H. He. An optimization-based arm posture prediction in presence of obstacles. In *International Conference on Computer-Aided Industrial Design and Conceptual Design, CAID/CD*, 2008.

[79] M. Malik. Heart rate variability: Standards of measurement, physiological interpretation, and clinical use. *Circulation*, 93(5):1043–1065, 1996.

[80] B. Masih-Tehrani and F. Janabi-Sharifi. Kinematic and dynamic dextery measures for posture prediction. In *IEEE/RSJ International Conference on Intelligent Robots and Systems, IROS*, 2008.

[81] L. McAtamney and E. N. Corlett. RULA: a survey method for the investigation of work-related upper limb disorders. *Applied ergonomics*, 24:91–99, 1993.

[82] R. McCraty, M. Atkinson, W. A. Tiller, G. Rein, and A. D. Watkins. The effects of emotions on short-term power spectrum analysis of heart rate variability. *American Journal of Cardiology*, 76(14):1089–1092, 1995.

[83] Y. Michellod, P. Mullhaupt, and D. Gillet. On achieving periodic joint motion for redundant robots. In *IFAC World Congress*, pages 4355–4360, 2008.

[84] M. Mori. The uncanny valley. *Energy*, 7(4):33, 1970.

[85] R. M. Murray, Z. Li, and S. S. Sastry. *A Mathematical Introduction to Robotic Manipulation*. CRC Press, 1994.

[86] F. A. Mussa-Ivaldi and N. Hogan. Integrable solutions of kinematic redundancy via impedance control. *International Journal of Robotics Research*, 10(5):481–491, 1991.

[87] F. A. Mussa-Ivaldi, N. Hogan, and E. Bizzi. Neural, mechanical and geometric factors subserving arm posture in humans. *The Journal of Neuroscience*, 5:2732–2743, 1985.

[88] Y. Nakamura and H. Hanafusa. Inverse kinematic solutions with singularity robustness for manipulator control. *ASME Journal of Dynamic Systems, Measurment, and Control*, 108:163–171, 1986.

[89] T. Olsson, M. Haage, H. Kihlman, R. Johansson, K. Nilsson, A. Robertsson, M. Björkman, R. Isaksson, G. Ossbahr, and T. Brogårdh. Cost-efficient drilling using industrial robots with high-bandwidth force feedback. *Robotics and Computer-Integrated Manufacturing*, 26:24–38, 2010.

[90] T. Olsson, A. Robertsson, and R. Johansson. Flexible force control for accurate low-cost robot drilling. In *IEEE International Conference on Robotics and Automation, ICRA*, pages 4770–4775, 2007.

[91] E. B. Page. Ordered hypotheses for multiple treatments: A significance test for linear ranks. *Journal of the American Statistical Association*, 58(301):216–230, 1963.

[92] H. E. Rauch, F. Tung, and C. T. Striebel. Maximum likelihood estimates of linear dynamic systems. *AIAA Journal*, 3:1445–1450, 1965.

[93] N. Ravaja, M. Turpeinen, T. Saari, S. Puttonen, and L. Keltikangas-Järvinen. The psychophysiology of james bond: Phasic emotional responses to violent video game events. *Emotion*, 8(1):114–120, 2008.

[94] R. G. Roberts and A. A. Maciejewski. Nearest optimal repeatable control strategies for kinematically redundant manipulators. *IEEE Transactions on Robotics and Automation*, 8(3):327–337, 1992.

[95] A. M. Sabatini. Identification of neuromuscular synergies in natural upper-arm movements. *Biological Cybernetics*, 86:253–262, 2002.

[96] M. A. Sahir-Arikan and T. Balkann. Process modeling, simulation and paint thickness measurement for robotic spray painting. *Journal of Robotic Systems*, 17:479–494, 2000.

[97] M. Santello, M. Flanders, and J. F. Soechting. Postural hand synergies for tool use. *Journal of Neuroscience*, 18(23):10105–10115, 1998.

[98] R. Schaufler, C. H. Fedrowitz, and R. Kammüller. A simplified criterion for repeatability and its application in constraint path planning problems. In *IEEE/RSJ International Conference on Intelligent Robots and Systems, IROS*, pages 2345–2350, 2000.

[99] R. Schmidt, C. Disselhorst-Klug, J. Silny, and G. Rau. A marker-based measurement procedure for unconstrained wrist and elbow motions. *Journal of Biomechanics*, 32:615–621, 1999.

[100] J. P. Scholz and G. Schöner. The uncontrolled manifold concept: identifying control variables for a functional task. *Experimental Brain Research*, 126(3):289–306, 1999.

[101] C. Schubert, M. Lambertz, R. A. Nelesen, W. Bardwell, J. B. Choi, and J. E. Dimsdale. Effects of stress on heart rate complexity - A comparison between short-term and chronic stress. *Biological Psychology*, 80(3):325–332, 2009.

[102] L. Sciavicco and B. Siciliano. A solution algorithm to the inverse kinematic problem for redundant manipulators. *IEEE Journal of Robotics and Automation*, 4(4):403–410, aug 1988.

[103] L. Sciavicco and B. Siciliano. *Modelling and Control of Robot Manipulators*. Springer, 2000.

[104] H. Seraji. Configuration control of redundant manipulators: Theory and implementation. *IEEE Transactions on Robotics and Automation*, 5(4):472–490, 1989.

[105] T. Shamir and Y. Yomdin. Repeatability of redundant manipulators: Mathematical solution of the problem. *IEEE Transactions on Automatic Control*, 33(11):1004–1009, 1988.

[106] B. Siciliano. A closed-loop inverse kinematic scheme for on-line joint-based robot control. *Robotica*, 8:231–243, 1990.

[107] L. J. Soslowsky, E. L. Flatow, L. U. Bigliani, and V. C. Mow. Articular geometry of the glenohumeral joint. *Clinical Orthopaedics and Related Research*, 285:181–190, 1992.

[108] I. H. Suh and K. G. Shin. Coordination of dual robot arms using kinematic redundancy. *IEEE Transactions on Robotics and Automation*, 5(2):236–242, apr 1989.

[109] T. J. Tarn, A. Bejczy, and X. Yun. Coordinated control of two robot arms. In *IEEE Conference on Robotics and Automation, ICRA*, volume 3, pages 1193–1202, 1986.

[110] K. P. Tee, D. W. Franklin, M. Kawato, T. E. Milner, and E. Burdet. Concurrent adaptation of force and impedance in the redundant muscle system. *Biological Cybernetics*, 2010.

[111] R. Tempo, G. Calafiore, and F. Dabbene. *Randomized algorithms for analysis and control of uncertain systems*. Springer, 2005.

[112] G. Terres-Oviedo and L. H. Ting. Muscle synergies characterizing human postural responses. *Journal of Neurophysiology*, 98:2144–2156, 2007.

[113] A. Terrier, M. Aeberhard, Y. Michellod, P. Mullhaupt, D. Gillet, A. Farron, and D. Pioletti. A musculoskeletal shoulder model based on pseudo-inverse and null-space optimization. *Medical Engineering and Physics*, in press.

[114] E. Todorov. Optimality principles in sensorimotor control. *Nature Neuroscience*, 7:907–915, 2004.

[115] C. Towell, M. Howard, and S. Vijayakumar. Learning nullspace policies. In *IEEE/RSJ International Conference on Intelligent Robots and Systems, IROS*, pages 241–248, 2010.

[116] P. van der Smagt, M. Grebenstein, H. Urbanek, N. Fligge, M. Strohmayr, G. Stillfried, J. Parrish, and A. Gustus. Robotics of human movements. *Journal of Physiology - Paris*, 103(3-5):119–132, 2009.

[117] Z. Wang and K. Kazerounian. Analytical determination of the null space of anthromorphic manipulators. *IEEE Transactions on Systems, Man, and Cybernetics*, 22(6):1488–1492, 1992.

[118] C. Wei and Z. Dean. Tool trajectory optimization of robotic spray painting. In *Second International Conference on Intelligent Computation Technology and Automation, ICICTA*, pages 419–422, 2009.

[119] H. J. Woltring. A Fortran package for generalized, cross-validatory spline smoothing and differentiation. *Advances in Engineering Software*, 8:104–110, 1986.

[120] R. W. Yeung. *A first course in information theory*. Springer, 2002.

[121] T. Yoshikawa. Dynamic manipulability of robot manipulators. In *IEEE International Conference on Robotics and Automation, ICRA*, pages 1033–1038, 1985.

[122] T. Yoshikawa. Manipulability of robotic mechanisms. *International Journal of Robotics Research*, 4(2):3–9, 1985.

[123] F. Zacharias, C. Schlette, F. Schmidt, C. Borst, J. Rossmann, and G. Hirzinger. Making planned paths look more human-like in humanoid robot manipulation planning. In *IEEE International Conference on Robotics and Automation, ICRA*, pages 1192–1198, 2011.

[124] A. M. Zanchettin, P. Rocco, L. Bascetta, I. Symeonidis, and S. Peldschus. Kinematic motion analysis of the human arm during a manipulation task. In *Joint 41th International Symposium on Robotics and 6th German Conference on Robotics, ISR/Robotik*, 2010.

[125] A. M. Zanchettin, P. Rocco, and G. Ferretti. Numerical issues in integrating holonomic kinematic inversion algorithms for redundant manipulators. In *IFAC Symposium on Nonlinear Control Systems, NOLCOS*, pages 999–1004, 2010.

[126] V. M. Zatsiorsky. *Kinematics of human motion*. Human Kinetics, 1998.

APPENDIX $\mathcal{A}$

Pseudo-code of the random walk algorithm

In this work an adapted version of a random walk algorithm has been considered, see [28]. Under very simple assumptions, this method generates randomly selected samples from a quasi-uniform distribution in the manifold

$$\mathcal{D} = \{\boldsymbol{q} : \|\boldsymbol{\sigma}(\boldsymbol{q})\| \leq \epsilon\}$$

A pseudo-code of the algorithm is given in the following.

Suppose that $k-1 < M$ samples have already been generated in $\mathcal{D}$. Then, in order to generate the k-th sample:

1: set $\Delta > 0$, small enough
2: select the number of steps, $T \gg 1$
3: pick a random sample $\boldsymbol{q}^{(j)}$, $j \in [1, k-1]$

proc $randStep\left(\boldsymbol{q}^{(j)}, T, \Delta\right)$
output: $\boldsymbol{q}^{(k)} \in \mathcal{D}$

1: $s \leftarrow 0$
2: $\boldsymbol{q}^{(k),0} \leftarrow \boldsymbol{q}^{(j)}$
3: generate a random direction $\boldsymbol{v}$, $\|\boldsymbol{v}\| = 1$ in the null-space of $\boldsymbol{\sigma}(\boldsymbol{q}) = \boldsymbol{0}$, i.e. such that $[\partial\boldsymbol{\sigma}/\partial\boldsymbol{q}]\,\boldsymbol{v} = \boldsymbol{0}$
4: $\boldsymbol{q}^{(k),s+1} \leftarrow \boldsymbol{q}^{(k),s} + \Delta\boldsymbol{v}$
5: $s \leftarrow s + 1$
6: **if** $s = T$ **then**

7: $\boldsymbol{q}^{(k)} \leftarrow \boldsymbol{q}^{(k),T}$
8: **return** $\boldsymbol{q}^{(k)}$
9: **else**
10: goto step 5.
11: **end if**

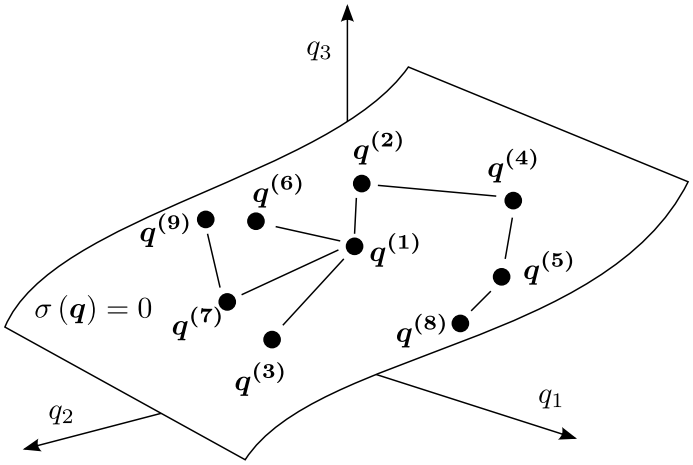

Figure A.1: *Random walk algorithm*

Notice that if $T \gg 1$ is selected large enough, then, since the point $\boldsymbol{q}^{(k),s+1}$ is very close to $\boldsymbol{q}^{(k),s}$, this algorithm spreads rapidly within a simply-connected region $\mathcal{D}$, where the constraint $\boldsymbol{\sigma}(\boldsymbol{q}) = \mathbf{0}$ is enforced.
In the literature, these algorithms are also referred to as Markov Chain Monte Carlo (MCMC) methods. The graph consists in configurations $\boldsymbol{q}$ such that $\|\boldsymbol{\sigma}(\boldsymbol{q})\| \leq \epsilon$. The sequence of randomly explored nodes of the graph constitutes the Markov Chain. A detailed review on the use of these methods to generate uniform distributions can be found in [111].
In Fig. A.1, one instance of the algorithm is running in order to generate random configurations within a simply-connected manifold $\sigma(\boldsymbol{q}) = 0$.

APPENDIX $\mathcal{B}$

Greedy algorithm for quadratic optimization

Given the (possibly sparse) square matrix $\boldsymbol{A} = \boldsymbol{A}^T \geq 0$ and the vector $\boldsymbol{b}$, the problem we would like to solve here is the following one:

$$\min_{\boldsymbol{x} \in \mathbb{R}^n} \|\boldsymbol{A}\boldsymbol{x} + \boldsymbol{b}\|$$

Clearly, when matrix $\boldsymbol{A}$ is non-singular, the unique solution is given by

$$\boldsymbol{x} = -\boldsymbol{A}^{-1}\boldsymbol{b}$$

However, when matrix $\boldsymbol{A}$ has a large number of entries, this problem is difficult to deal with. Moreover, using the given solution might result in a vector $\boldsymbol{x}$ with many non-zero entries. Therefore, in order to reduce the number of non-zero entries of vector $\boldsymbol{x}$, a greedy algorithm with pruning can be adopted, see e.g. [26]. The greedy algorithm iteratively increments the number of admissible non-zero entries of vector $\boldsymbol{x}$, until a satisfactory solution is found. For this a threshold F_{TH}^0 is used as a parameter of the algorithm.

A pseudo-code of the greedy algorithm is given in the following.

proc $greedy\left(\boldsymbol{A}, \boldsymbol{b}, \mathcal{P}, F_{TH}^0\right)$
output: $\boldsymbol{x}$
1: $r \leftarrow findBestRegressor\left(\boldsymbol{A}, \boldsymbol{b}, \mathcal{P}\right)$
2: $\mathcal{U} \leftarrow \{r\}$
3: $\boldsymbol{x} \leftarrow solve\left(\boldsymbol{A}, \boldsymbol{b}, \mathcal{U}\right)$

4: $n \leftarrow \|\boldsymbol{A}\boldsymbol{x} + \boldsymbol{b}\|$
5: **while** $n \geq F_{TH}^{0} \wedge \neg isempty\,(\mathcal{P} \setminus \mathcal{U})$ **do**
6: $r \leftarrow findBestRegressor\,(\boldsymbol{A}, \boldsymbol{b}, \mathcal{P} \setminus \mathcal{U})$
7: $\mathcal{U} \leftarrow \mathcal{U} \cup \{r\}$
8: $s \leftarrow findWorstRegressor\,(\boldsymbol{A}, \boldsymbol{b}, \mathcal{P} \setminus \mathcal{U})$
9: **if** $s \neq r$ **then**
10: $\mathcal{U} \leftarrow \mathcal{U} \setminus \{s\}$
11: **end if**
12: $\boldsymbol{x} \leftarrow solve\,(\boldsymbol{A}, \boldsymbol{b}, \mathcal{U})$
13: $n \leftarrow \|\boldsymbol{A}\boldsymbol{x} + \boldsymbol{b}\|$
14: **end while**
15: $\boldsymbol{x} \leftarrow solve\,(\boldsymbol{A}, \boldsymbol{b}, \mathcal{U})$

APPENDIX C

Dual-arm Jacobian matrix

Consider the leader-follower robotic system of Fig. 3.9 and define:

$$\boldsymbol{v_l} = \begin{bmatrix} \dot{\boldsymbol{p}}_{\boldsymbol{l}}{}^T & \boldsymbol{\omega_l}{}^T \end{bmatrix}^T = \begin{bmatrix} \boldsymbol{J_l} & \boldsymbol{0} \end{bmatrix} \dot{\boldsymbol{q}} \quad \boldsymbol{v_f} = \begin{bmatrix} \dot{\boldsymbol{p}}_{\boldsymbol{f}}{}^T & \boldsymbol{\omega_f}{}^T \end{bmatrix}^T = \begin{bmatrix} \boldsymbol{0} & \boldsymbol{J_f} \end{bmatrix} \dot{\boldsymbol{q}} \tag{C.1}$$

the differential kinematic relations of each robot with respect to the world frame where $\boldsymbol{v_l}$ and $\boldsymbol{v_f}$ are the twist of the leader and of the follower, respectively. In the following the relative differential kinematics of the two robots, namely the relation between the relative twist $\boldsymbol{v_r} = \begin{bmatrix} \dot{\boldsymbol{p}}_{\boldsymbol{r}}{}^T & \boldsymbol{\omega_r}{}^T \end{bmatrix}^T$ and the joint velocities $\dot{\boldsymbol{q}}$ will be derived.

For convenience, first define

$$\boldsymbol{W} = \begin{bmatrix} \boldsymbol{R_l} & \boldsymbol{p_l} \\ \boldsymbol{0} & 1 \end{bmatrix} \quad \boldsymbol{T} = \begin{bmatrix} \boldsymbol{R_f} & \boldsymbol{p_f} \\ \boldsymbol{0} & 1 \end{bmatrix} \quad \boldsymbol{R} = \begin{bmatrix} \boldsymbol{R_r} & \boldsymbol{p_r} \\ \boldsymbol{0} & 1 \end{bmatrix} \tag{C.2}$$

then, using the well known relations to compose velocities (see e.g. [31])

$$\begin{aligned} \dot{\boldsymbol{p}}_{\boldsymbol{f}} &= \dot{\boldsymbol{p}}_{\boldsymbol{l}} + \boldsymbol{\omega_l} \times \boldsymbol{R_l} \boldsymbol{p_r} + \boldsymbol{R_l} \dot{\boldsymbol{p}}_{\boldsymbol{r}} \\ \boldsymbol{\omega_f} &= \boldsymbol{R_l} \boldsymbol{\omega_r} + \boldsymbol{\omega_l} \end{aligned} \tag{C.3}$$

one obtains

$$\begin{aligned} \dot{\boldsymbol{p}}_{\boldsymbol{r}} &= \boldsymbol{R_l}{}^T \dot{\boldsymbol{p}}_{\boldsymbol{f}} - \boldsymbol{R_l}{}^T \dot{\boldsymbol{p}}_{\boldsymbol{l}} + \boldsymbol{p_r} \times \boldsymbol{R_l}{}^T \boldsymbol{\omega_l} = \boldsymbol{R_l}{}^T \dot{\boldsymbol{p}}_{\boldsymbol{f}} - \boldsymbol{R_l}{}^T \dot{\boldsymbol{p}}_{\boldsymbol{l}} + \boldsymbol{S}\left(\boldsymbol{p_r}\right) \boldsymbol{R_l}{}^T \boldsymbol{\omega_l} \\ \boldsymbol{\omega_r} &= \boldsymbol{R_l}{}^T \boldsymbol{\omega_f} - \boldsymbol{R_l}{}^T \boldsymbol{\omega_l} \end{aligned} \tag{C.4}$$

which can be written as follows

$$\begin{aligned} \boldsymbol{v_r} &= \begin{bmatrix} \boldsymbol{R_l}^T & \boldsymbol{0} \\ \boldsymbol{0} & \boldsymbol{R_l}^T \end{bmatrix} \boldsymbol{v_f} - \begin{bmatrix} \boldsymbol{R_l}^T & \boldsymbol{0} \\ \boldsymbol{0} & \boldsymbol{R_l}^T \end{bmatrix} \boldsymbol{v_l} + \begin{bmatrix} \boldsymbol{0} & \boldsymbol{S}\left(\boldsymbol{p_r}\right) \boldsymbol{R_l}^T \\ \boldsymbol{0} & \boldsymbol{0} \end{bmatrix} \boldsymbol{v_l} \\ &= \begin{bmatrix} \boldsymbol{R_l}^T & \boldsymbol{0} \\ \boldsymbol{0} & \boldsymbol{R_l}^T \end{bmatrix} \begin{bmatrix} -\boldsymbol{J_l} & \boldsymbol{J_f} \end{bmatrix} \dot{\boldsymbol{q}} + \begin{bmatrix} \boldsymbol{0} & \boldsymbol{S}\left(\boldsymbol{p_r}\right) \boldsymbol{R_l}^T \\ \boldsymbol{0} & \boldsymbol{0} \end{bmatrix} \begin{bmatrix} \boldsymbol{J_l} & \boldsymbol{0} \end{bmatrix} \dot{\boldsymbol{q}} \\ &= \left\{ \begin{bmatrix} \boldsymbol{R_l}^T & \boldsymbol{0} \\ \boldsymbol{0} & \boldsymbol{R_l}^T \end{bmatrix} \begin{bmatrix} -\boldsymbol{J_l} & \boldsymbol{J_f} \end{bmatrix} + \begin{bmatrix} \boldsymbol{0} & \boldsymbol{S}\left(\boldsymbol{p_r}\right) \boldsymbol{R_l}^T \\ \boldsymbol{0} & \boldsymbol{0} \end{bmatrix} \begin{bmatrix} \boldsymbol{J_l} & \boldsymbol{0} \end{bmatrix} \right\} \dot{\boldsymbol{q}} \end{aligned} \tag{C.5}$$

POLITECNICO DI MILANO
Dipartimento di Elettronica e Informazione
Piazza Leonardo da Vinci, 32 I-20133 - Milano